Contract No:

This document was prepared in conjunction with work accomplished under Contract No. DE-AC09-08SR22470 with the U.S. Department of Energy (DOE) Office of Environmental Management (EM).

We put science to work.™

Savannah River
National Laboratory™

OPERATED BY SAVANNAH RIVER NUCLEAR SOLUTIONS

A U.S. DEPARTMENT OF ENERGY NATIONAL LABORATORY • SAVANNAH RIVER SITE • AIKEN, SC

DWPF Melter Off-Gas Chemistry Model for the Nitric-Glycolic Acid Flowsheet

A. S. Choi

June 2018

SRNL-STI-2014-00355, Rev. 1

DISCLAIMER

Printed in the United States of America

Prepared for
U.S. Department of Energy

SRNL-STI-2014-00355
Revision 1

Keywords: DWPF, Nitric-Glycolic Acid Flowsheet, Melter Off-Gas Flammability, CEF Phase 2

Retention: *Permanent*

DWPF Melter Off-Gas Chemistry Model for the Nitric-Glycolic Acid Flowsheet

A. S. Choi

June 2018

Prepared for the U.S. Department of Energy under contract number DE-AC09-08SR22470.

Savannah River National Laboratory™
OPERATED BY SAVANNAH RIVER NUCLEAR SOLUTIONS

REVIEWS AND APPROVALS

AUTHOR:

A. S. Choi, Process Technology Programs Date

TECHNICAL REVIEW:

J. R. Zamecnik, Process Technology Programs Date

APPROVAL:

F. M Pennebaker, SRR Customer Relations Manager Date
Chemical Processing Technologies/Environmental Stewardship/SRNL

D. E. Dooley, Director Date
Chemical Processing Technologies/Environmental Stewardship/SRNL

E. J. Freed, Manager Date
Defense Waste Processing Facility & Saltstone Facility Engineering, SRR

ACKNOWLEDGEMENTS

Expert reviews and timely programmatic guidance provided by T. L. Fellinger, E. W. Holtzscheiter, M, E. Smith of Savannah River Remediation throughout the course of this study are greatly appreciated. The author also would like to recognize the immense contributions made by F. C. Johnson (Lead), and the rest of the CEF Team members to the successful planning and execution of the CEF Phase 2 test. The author would like to particularly single out F. C. Johnson for her dedication and efforts to coordinate post-run analysis of a countless number of feed, glass, and condensate samples taken throughout the test. The author also would like to point out that the dedication by J. R. Zamecnik in setting up the comprehensive off-gas sampling system, collecting and post-run processing of a very large amount of off-gas data as well as providing a thorough and critical technical review of Revision 1 calculations was central to the successful completion of this study. A timely and thorough technical review of the calculations made in Revision 0 and the report content provided by F. G. Smith and W. E. Daniel are also appreciated.

EXECUTIVE SUMMARY

The Defense Waste Processing Facility (DWPF) melter off-gas flammability model for the current nitric-formic acid (NFA) flowsheet was revised in Revision 0 to reflect the upcoming reductant change from formic to glycolic acid. The necessary data for the model revision was obtained during Phase 2 of the Cold-cap Evaluation Furnace (CEF) test, which was completed on March 21, 2014 after 24 days of round-the-clock feeding and pouring, including a total downtime of ~20 hours due to equipment failures. Specifically, the CEF was run to generate steady state melter off-gas data during the first 10 days using two nitric-glycolic acid (NGA) flowsheet feeds prepared at 100% and 125% acid stoichiometry from the same Sludge Batch 6 (SB6) simulant used during the Phase 1 CEF test in 2013. Each feed was fed under both bubbled and non-bubbled conditions, while maintaining the CEF vapor space temperature constant for at least two hours approximately at 700, 600, 500, 400, 350, and <300 °C for a total of 26 steady state runs. During the next 8 days, the CEF was run at the nominal vapor space temperature of 700 °C to generate the off-gas surge data using the 100% acid-stoichiometry feed under bubbled and non-bubbled conditions. The remaining days were spent on producing additional data using the 100% acid-stoichiometry feed spiked with excess antifoam as well as re-running some of the earlier steady state runs.

Recently, an additional set of off-gas data from the Phase 2 test was made available mainly in the form of nitrogen oxide gases (NO, NO_2, N_2O and NO_x) measured by Fourier Transform Infrared Spectroscopy (FTIR). This new data has enabled a more rigorous description of nitrogen chemistry in the cold cap and this revision documents how the new nitrogen chemistry scheme was developed and implemented into the NGA flowsheet model developed in Revision 0. Some of the key results from the Phase 2 test include:

- At the vapor space gas temperature (T_{gas}) < ~500 °C under non-bubbled conditions, each carbon in the NGA flowsheet feed produced about ¼ of the H_2 produced by each carbon in the NFA flowsheet feed used in Phase 1. As T_{gas} increased above 500 °C, the difference between the measured H_2 data for the two feeds narrowed but the data for the NGA flowsheet remained no higher than ½ of that of the NFA flowsheet. As the potential for melter off-gas flammability remains low until T_{gas} decreases below 400 °C, it can be concluded that on a per carbon basis the NGA flowsheet feed has only ¼ of the off-gas flammability potential of the NFA flowsheet feed, which may be attributed to the fact that the former has 3.6X higher nitrate (oxidant) than the latter.

- The measured concentration of H_2 was higher under bubbled conditions than non-bubbled at all T_{gas}, which appears to be primarily due to increased feed rate facilitated by the bubbling action at fixed air purge rates. Although no direct comparison of H_2 data between the two flowsheets could be made for bubbled operation due to lack of such data for the NFA flowsheet feed, the trend of the NGA flowsheet feed having a much lower flammability potential under non-bubbled conditions than the NFA flowsheet feed should continue for bubbled operation.

- Glass samples were taken from the pour stream throughout the test and, except for those taken during the initial melter turnover, they were all determined to be fully oxidized, i.e., $Fe^{2+}/\Sigma Fe = 0$. A potential for the air-glass contact existed especially when the pour stream became sluggish and intermittent during low-temperature runs. However, glass samples remained fully oxidized during the surge test, where the feed/pour rates were kept high for ~4 straight days round-the-clock (thus minimizing the air-glass contact) with constant bubbling of the melt pool with argon at 2-3X the DWPF bubbling flux (which should have made glass reducing) and with feeds spiked with up to 3X the normal antifoam (reductant). This suggests that the nitrate level in the Phase 2 feeds might have been too high to produce non-zero REDOX glass.

- With the NGA flowsheet feed, off-gas surged more frequently with greater intensity than with the NFA flowsheet feed. The increased propensity for surging is attributed to the higher nitrate level in the NGA flowsheet feed as the nitrate releases not only the greatest volume of gases among all gas generators in the feed but it continues to do so past 900 °C, where the cold cap is most prone to foaming, thus causing increased turbulence and instabilities.

- The largest pressure spike of significance to the off-gas flammability occurred during bubbled Phase 2 test; it was in excess of +13 "H_2O with its overall profile matching closely that of the DWPF design basis off-gas surge, including the total duration of 7 minutes. A further analysis showed that the magnitudes of the condensable and non-condensable flow surges associated with the +13 "H_2O pressure spike were close to 13X and 3X their respective normal flows. Compared to the 9X/5X NFA flowsheet surge basis for bubbled operation, the NGA flowsheet surge basis of 13X/3X is higher in the condensable flow but lower in the non-condensable flow. Although a higher condensable surge would lower the combustion kinetics more, the fuel flows are set directly by the non-condensable surge. Based on this reasoning, off-gas surges are expected to be somewhat less impactful on the flammability potential of the NGA flowsheet melter off-gas.

All the key components of the NFA flowsheet model construct were retained in the revised models. The impact of the new flowsheet chemistry was instead modeled by adding a new reaction zone on top of the cold cap where the volatile feed components and those with low decomposition temperatures participate in the pre- and post-cold cap reactions before entering the vapor space reactor. Glycolic-acid denitration is one such pre-cold cap reaction; a portion of nitrate in the feed is destroyed by free glycolic acid (i.e., un-dissociated glycolic acid of neutral charge) and thus excluded from the cold cap model input. The extent of the glycolic-acid denitration reaction was set based on the bench-scale calciner data found in the literature: 90% at the stoichiometric glycolic acid-to-nitrate ratio of 1:2. The remaining free glycolic acid after the denitration reaction was thermally decomposed to CO and H_2 also in the new reaction zone, which acts as a buffer between the cold cap and the vapor space reactor. A correlation was derived that predicts the extent of glycolic-acid decomposition as a function of T_{gas} for the baseline case run with 100% acid-stoichiometry feed under non-bubbled conditions (100%_NB).

The new data showed that $\geq$ 60% of nitrate fed was detected as NO in the off-gas, while NO_2, N_2O and N_2 constituted approximately 10-15% each. (Note N_2 was calculated as the balance of total N fed as nitrate after subtracting $NO/NO_2/N_2O$.) Under the thermodynamic equilibrium premise, however, the cold cap model predicted that nearly 100% of nitrate would decompose to N_2 and O_2, which is not in agreement with the data. To overcome this difficulty, N_2 was removed from the list of potential equilibrium species and the model then predicted that nearly 100% of nitrate would decompose to NO, which is closer to the data but made the resulting calcine gases too reducing in the process, i.e., the predicted concentrations of H_2 and CO were too high. This necessitated the following post-cold cap reactions; reduction of NO to N_2 and O_2 followed by the oxidation of H_2 and CO. The extent of reaction for the NO-to-N_2 reduction was set to match the "measured" N_2 concentration in the off-gas.

It turns out that the O_2 produced from the reduction of NO was not nearly enough to oxidize H_2 and CO to a sufficient degree. This necessitated an additional source of O_2, which came in the form of air infiltration. As the vapor space is filled with excess air from air purges and air inleakage, it is conceivable that some fraction of air would infiltrate the new reaction zone and react with H_2 and CO coming out of the cold cap. It is interesting to note that the total O_2 made available from both the reduction of NO and air infiltration was found to be proportional to the feed rate regardless of the feed chemistry (i.e., 100% or 125% acid stoichiometry) and the operating mode (i.e., bubbled or non-bubbled).

It was also found in Revision 0 that the NFA flowsheet model under-predicted the combustion rates of H_2 in the vapor space at $T_{gas} < 350$ °C but over-predicted at $T_{gas} > 350$ °C. This means that the existing global first-order kinetic parameters of H_2/CO oxidation are conservative at $T_{gas} < 350$ °C but not so at $T_{gas} > 350$ °C. To ensure conservative prediction of combustion rates at all T_{gas}, the new global kinetic parameters of H_2/CO oxidation were derived for the baseline case by matching 125% of the measured H_2/CO data at $T_{gas} > 350$ °C during Phase 2. The resulting baseline model was shown to predict the measured CO data for the remaining cases with a sufficient margin of safety at all T_{gas} except for some degree of under-prediction for the 100%_B case at $T_{gas} \leq 275$ °C. However, under-prediction of CO by the observed magnitude should have no impact on the overall flammability potential as the lower flammability limit (LFL) of CO is 3X higher than that of H_2.

The baseline NGA flowsheet model was tested further against the steady state H_2/CO data taken just prior to the +13 "H_2O pressure spike as well as the bounding data taken during the pressure spike. The predicted concentrations of H_2 and CO for the pre-surge steady state were found to be slightly higher than their respective measured data, while the predicted bounding H_2/CO concentrations were 35-40% higher than their respective measured data. Although encouraging, these results should not be interpreted as a sufficient validation of the revised model because the data used was obtained during the same melter run using the same feed that produced the data used for the model revision.

It is noted that the DWPF has since implemented a new melter off-gas flammability control and no longer requires the melter off-gas flammability model to set the Technical Safety Requirements (TSR) and feed interlocks for the melter operation. Therefore, the new model presented in this report may be viewed as a tool for assessing the impact of changing process and input conditions on the underlying chemistry of the cold cap/REDOX reactions and the combustion of flammable gases produced during the calcination/fusion process. As such, the model is called the DWPF melter off-gas chemistry model from here on.

Based on the results of Phase 2 data analysis and model development highlighted thus far, the following conclusions can be drawn:

1. At $T_{gas} < 400$ °C, where the potential for off-gas flammability could increase appreciably, the NGA flowsheet feed produced ¼ of the H_2 produced by the NFA flowsheet feed on a per carbon basis.

2. A new bounding off-gas surge basis has been defined for the NGA flowsheet; it consists of 13X the normal condensable and 3X the normal non-condensable flows for bubbled operation. For non-bubbled operation, the existing 3X/3X surge basis for the NFA flowsheet is still bounding.

3. The DWPF melter off-gas chemistry model has been revised for the NGA flowsheet - its new parameters were set to match, as a conservative measure, 125% of the measured H_2 and CO data during Phase 2 for the baseline case with 100% acid-stoichiometry feed under non-bubbled conditions. The baseline model was shown to predict both the steady state and bounding H_2/CO data taken during the +13 "H_2O pressure spike well.

4. All glass samples taken during Phase 2 were fully oxidized (i.e., $Fe^{2+}/\Sigma Fe = 0$) even under the test conditions designed to induce reducing conditions in the feed (spiked with 2-3X normal antifoam) and in the melt pool (bubbled with argon at 2X the DWPF bubbling flux) along with the efforts to minimize the air-glass contact by continuously feeding/pouring at very high rates round-the-clock for 4 straight days.

5. The existing correlation used to estimate the true gas temperature in the DWPF melter vapor space from the measured data (TI4085D) for the combustion kinetics calculations is conservative, which confirms the earlier findings of the Phase 1 test.

6. The results of carbon balance on the analytical data for the Phase 2 feed samples and the off-gas data suggest that the current analytical method used to detect the glycolate is under reporting it. Specifically, based on the analysis of feed sample data, the reported glycolate may be low by up to 18-20%.

It is recommended that:

1. The current analytical method for glycolate be optimized to reduce the detected bias in glycolate data. The new analytical results should be compared against the difference between the measured TOC_{DWPF} and the sum of non-glycolate carbons from IC analysis and antifoam carbon from the recipe.

2. As the nitrogen balance suggests that excess nitrate may be influencing measured REDOX data, the current REDOX method should be re-evaluated and further optimized to better reflect the role of varying TOC-to-nitrate ratio.

3. The new parameters added to the revised DWPF melter off-gas chemistry model be validated prior to using the model for process optimization purposes.

TABLE OF CONTENTS

LIST OF TABLES

LIST OF FIGURES

LIST OF ABBREVIATIONS

AD	Analytical Development
CC	closed crucible
CEF	Cold cap Evaluation Furnace
DCS	Distributed Control System
DWPF	Defense Waste Processing Facility
FC	Film Cooler
FTIR	Fourier Transform Infrared Spectroscopy
GC	Gas Chromatography
IC	Ion Chromatography
ICP	Invariant Condensed Phase
ICP-MS	Inductively Coupled Plasma Mass Spectrometry
LAW	Low Activity Waste
LFL	lower flammability limit
MCU	Modular Caustic-side solvent extraction Unit
MFT	Melter Feed Tank
MS	Mass Spectrometry
MOG	melter off-gas
NFA	nitric-formic acid
NGA	nitric-glycolic acid
OGCT	Off-Gas Condensate Tank
PNNL	Pacific Northwest National Laboratory
PEG	polyethylene glycol
PSAL	Process Science Analytical Laboratory
REDOX	Reduction-Oxidation
SB	Sludge Batch
SGM	Scale Glass Melter
SME	Sludge Mix Evaporator
SRAT	Sludge Receipt and Adjustment Tank
SRNL	Savannah River National Laboratory
SRR	Savannah River Remediation
TOC	total organic carbon
TSR	Technical Safety Requirements
TTR	Technical Task Request
VS	vapor space

1.0 Introduction

The Defense Waste Processing Facility (DWPF) at the Department of Energy's (DOE) Savannah River Site (SRS) is planning a flowsheet change to replace formic acid with glycolic acid as the baseline reductant for the high-level waste (HLW) melter feed.[1] Nitric acid is used in conjunction with either formic or glycolic acid to neutralize the alkaline sludge from the Tank Farms. Thus, the existing flowsheet will be referred to as the nitric-formic acid (NFA) flowsheet, while the new flowsheet will be referred to as the nitric-glycolic acid (NGA) flowsheet in this report. Prior to implementation, the processability of the NGA flowsheet feed through a melter was demonstrated during the Phase 2 Cold-cap Evaluation Furnace (CEF) test in 2014, which lasted for 24 days with round-the-clock feeding/pouring. Concurrently with the melter demonstration, three sets of data necessary for the development of the DWPF melter off-gas flammability technical bases for the NGA flowsheet were also collected; (1) steady state melter and off-gas data with the vapor space temperature held constant for two hours at near 700, 600, 500, 400, 350, and <300 °C, (2) off-gas surge data for both condensable and non-condensable flows, and (3) additional steady state data using the feeds spiked with excess antifoam.[2] Two NGA flowsheet feeds at 100% and 125% acid stoichiometry were used to produce Set 1, whereas only the 100% acid stoichiometry feed was used to produce Sets 2 and 3. Moreover, Sets 1 and 2 were collected under bubbled and non-bubbled conditions, while Set 3 was collected only under non-bubbled conditions.

A detailed description of the Phase 2 CEF run is given elsewhere.[3] The purpose of this study was to; (1) reconcile/analyze the collected data, (2) develop a new off-gas surge basis, and (3) develop a new DWPF melter off-gas flammability model for the NGA flowsheet. The results of these activities were documented in Revision 0 of this report.[4] As the NGA flowsheet feed has a nearly 4X higher concentration of nitrate than the NFA flowsheet feed, it was important for the model to adequately describe the chemistry of nitrate decomposition and further reactions with other feed constituents in the cold cap. The success of the resulting model would then be determined by how well it predicts the measured concentrations of not only H_2/CO but NO/NO_2/N_2O in the off-gas. Unfortunately, it was not feasible to fully develop the nitrate decomposition chemistry since the measured concentrations of NO and NO_2 by Mass Spectrometer (MS) would result in a negative concentration of N_2, which was calculated as the balance of the nitrate fed after subtracting NO, NO_2 and N_2O. Since then, the NO/NO_2 data by Fourier Transform Infrared Spectroscopy (FTIR) has become available, and a preliminary analysis has shown that the nitrogen balance seems to work better with the FTIR data. Therefore, the purpose of this revision was to complete the development of the nitrate decomposition chemistry and implement it into the NGA flowsheet model.

The CEF is a 1/11th scale DWPF melter based on the effective melt surface area, excluding those areas occupied by various penetrations.[5] It was used in 2010 to study the impact of glass bubblers on melter off-gas surging (Phase 1),[6] and the frequency and intensity of off-gas surges during bubbled and non-bubbled CEF runs were found to be prototypic of the DWPF melter pressure spike data collected during the 6 months before and 6 months after the bubblers went into operation.[7] The CEF was also shown to be prototypic in terms of predicting the flammability potential of the DWPF melter off-gas;[8] the predicted concentrations of H_2 and CO by the existing DWPF melter off-gas flammability model correctly trended and further bounded the respective measured data in the off-gas produced with the NFA flowsheet feed during the Phase 1 CEF run. The seemingly-excessive over-prediction of the Phase 1 H_2 data at the melter vapor space gas temperature (T_{gas}) below ~350 °C was attributed to the conservative antifoam decomposition scheme used by the model and, therefore, was considered a modeling issue and not a design issue.

Furthermore, the thermal characteristics of the CEF vapor space were also shown to be prototypic thanks to its prototypic design.[8] Thus, it is ensured that the data taken during the Phase 2 run will be also prototypic and thus suitable to be used as the basis for developing the new DWPF melter flammability technical bases for the NGA flowsheet. This report details the results of the Phase 2 data analysis, highlights some of the characteristic features of melter operation with the NGA flowsheet feeds, and documents the key bases and assumptions of the new DWPF melter off-gas flammability model. The scope of this work is described in the Technical Task Request (TTR), HLW-DWPF-TTR-2013-0002, Rev. 1 and issue of this report satisfies Deliverable #4 of the TTR.[9]

It is noted that the DWPF has since implemented a new melter off-gas flammability control strategy and no longer requires the melter off-gas flammability model to set the process and operating limits for each sludge batch.[10] Therefore, the new model presented in this report may be viewed as a tool for assessing the impact of changing process and input conditions on the underlying chemistry of the cold cap/REDOX reactions and the combustion of flammable gases produced during the calcination/fusion process. As such, the model is called the DWPF melter off-gas chemistry model from here on.

2.0 Phase 2 CEF Run

2.1 Overview

A total of 26 steady state data points were collected using two NGA flowsheet feeds prepared at 100% and 125% acid stoichiometry with each fed at 6-8 different vapor space temperatures under bubbled and non-bubbled conditions. Efforts were made to maintain steady state operation at each vapor space temperature for at least 2 hours; however, doing so proved to be more difficult than with the NFA flowsheet feed during Phase 1, as the system parameters fluctuated more and often started to drift suddenly. As a result, transition from one steady state to the next took considerably longer, particularly under bubbled conditions. It appears that these difficulties arose as the NGA flowsheet feed has a significantly higher concentration of nitrate than the NFA flowsheet feed. That is, with the nitrate being the main gas generator beyond 850 °C, turbulence in the cold cap and thus departure from steady state operation is more likely with increasing nitrate content. To see how large the difference in nitrate content of the two flowsheet feeds, it was estimated that each glycolate carbon in the NGA flowsheet feeds used in Phase 2 was counterbalanced by ~4X higher nitrate than each formate carbon in the NFA flowsheet feed used in Phase 1 at the same REDOX target.

2.2 Development of CEF Feed Compositions

The sludge simulant used was the same Sludge Batch 6 simulant recipe I (SB6I) used in Phase 1. Mercury and noble metals were not included in SB6I since they are not known to affect the melter off-gas flammability directly, and thus inclusion of these species was not considered a prerequisite for the melter feed simulants used in both CEF tests.[11] However, their presence is known to strongly affect the oxidant (nitrate) and reductant (carbon) balances of the melter feed, which in turn affects not only the rheological properties but the cold cap chemistry in terms of REDOX and off-gas flammability. For this reason, a series of 4L Sludge Receipt and Adjustment Tank (SRAT) runs were performed to provide the operating instructions for the nitric and glycolic acid additions and subsequent boil-up at an off-site vendor's facility (Harrell Industries) so that the SRAT products would meet all the target properties set for the Phase 2 feed in the absence of mercury and noble metals.[12,13] The reductant is made up of several different carbon species, including formate, glycolate and antifoam, and typically represented by the total organic carbon (TOC) data, although each carbon species has a varying reducing power.[14]

2.2.1 *SRAT Products*

The SRAT products received from Harrell Industries were analyzed at SRNL, and the results are shown in Table 2-1 and Table 2-2 for the 100% and 125% acid stoichiometry, respectively. It was noted that although the elemental results matched the expected targets for both products, the anion results were different than expected.[15,16] Specifically, the nitrate concentration of the 100% acid stoichiometry SRAT product met its target but the glycolate concentration was determined to be 22% higher, which seemed to be in line with the fact that the measured REDOX of glass made in a closed crucible-ramp (CC-ramp) was significantly higher than the target; 0.47 vs. 0.15.[15]

The CC-ramp is a setup where the crucible is inserted into the furnace at ambient temperature and heated to 1,150 °C at a given heating rate, as opposed to being inserted into the furnace already at 1,150 °C in the CC-hot. The lid should seal more quickly in the CC-hot, thus trapping the calcine gases longer than in the CC-ramp. However, even after the lid is sealed, gases can still escape once a threshold pressure is reached inside the crucible (although it is not known what that threshold pressure is).

On the other hand, the measured REDOX of glass made from the 125% acid stoichiometry SRAT product was <0.02 vs. the target of 0.2-0.3.[16] It was noted that the measured concentrations of anions such as nitrate, glycolate and formate were all within ±10% of their respective targets but the measured TOC was 49% higher than that calculated by summing up the anion data by Ion Chromatography (IC),[16] which seems to suggest that more antifoam may have been added than what the recipe called for. However, the higher than expected TOC data could not explain the fact that the measured redox was significantly lower than the target, as it should have led to a higher REDOX value than the target. Subsequently, these large discrepancies between the measured and target REDOX prompted a series of crucible studies to develop a remediation strategy to restore the REDOX to their respective targets.

Table 2-1. Analytical Data for the 100% Acid Stoichiometry SRAT Product.

	Elements	wt% calcined solids	Anions	mg/Kg slurry
Slurry	Al	13.486	F	<500
	Ba	0.133	Cl	<500
	Ca	1.117	NO_2	<500
	Cr	0.175	NO_3	66,950
	Cu	0.125	$C_2H_3O_3$	44,525
	Fe	21.305	SO_4	1,863
	K	0.313	C_2O_4	2,005
	Mg	0.852	COOH	3,135
	Mn	6.825	PO_4	<500
	Na	13.761	Bulk Properties	
	Ni	2.951	Total solids	32.27%
	P	<0.100	Insoluble solids	15.81%
	S	0.354	Soluble solids	16.46%
	Si	1.418	Calcined solids	17.97%
	Sn	0.060	Density (g/mL)	
	Ti	0.051	- slurry	1.2514
	Zn	0.111	- supernate	1.1340
	Zr	<0.100	pH	5.03
Supernate	Cations	mg/L	Anions	mg/L
	Al	349.2	F	<500
	Ba	1.716	Cl	565
	Ca	2,653	NO_2	<500
	Cr	1.544	NO_3	92,000
	Cu	56.125	$C_2H_3O_3$	60,050
	Fe	304.75	SO_4	2,628
	K	755.591	C_2O_4	2,563
	Mg	2,021.75	COOH	2903
	Mn	14,550	PO_4	<500
	Na	31,850		
	Ni	2,720	Misc. Data	
	P	<10.0	REDOX	$Fe^{2+}/\Sigma Fe$
	S	817.75	- Measured	0.47
	Si	706.5	- Target	0.15
	Sn	9.515	TOC (mg/kg)	
	Ti	0.323	- AD	12,546
	Zn	55.663	- DWPF Lab	20,790
	Zr	<0.100		

Table 2-2. Analytical Data for the 125% Acid Stoichiometry SRAT Product.

Slurry	Elements	wt% calcined solids	Anions	mg/Kg slurry
	Al	14.36	F	<500
	Ba	0.126	Cl	<500
	Ca	1.229	NO_2	<500
	Cr	0.175	NO_3	84,850
	Cu	0.117	$C_2H_3O_3$	43,500
	Fe	21.560	SO_4	2,695
	K	0.293	C_2O_4	2,155
	Mg	0.837	COOH	<500
	Mn	6.795	PO_4	<500
	Na	13.120	Bulk Properties	
	Ni	2.897	Total solids	32.77%
	P	<0.100	Insoluble solids	15.66%
	S	0.309	Soluble solids	17.12%
	Si	1.523	Calcined solids	17.72%
	Sn	<0.100	Density (g/mL)	
	Ti	0.050	- slurry	1.2553
	Zn	0.110	- supernate	1.1526
	Zr	0.142	pH	3.21
Supernate	Cations	mg/L	Anions	mg/L
	Al	1,100	F	<500
	Ba	3.461	Cl	567
	Ca	3,135	NO_2	<500
	Cr	4.350	NO_3	118,000
	Cu	182.5	$C_2H_3O_3$	59,650
	Fe	2,700	SO_4	3,120
	K	1,075	C_2O_4	3,200
	Mg	2,355	COOH	<500
	Mn	13,600	PO_4	<500
	Na	33,900		
	Ni	5,345	Misc. Data	
	P	18.57	Redox	$Fe^{2+}/\Sigma Fe$
	S	766.2	- Measured	<0.02
	Si	297.9	- Target	0.2-0.3
	Sn	6.233	TOC (mg/kg)	
	Ti	3.530	- AD	23,300
	Zn	144.0	- DWPF Lab	21,062
	Zr	0.100		

2.2.2 *Carbon Balance of Feeds*

The REDOX of a given feed is determined by the balance between the oxidant (nitrate) and reductant (glycolate, oxalate, formate, and antifoam) concentrations. Since both SRAT products missed their respective REDOX targets widely despite having followed the recipes provided by SRNL, it was decided to re-examine available anion data to determine the potential cause(s) for such large discrepancies. Accurately knowing the concentrations of oxidants and reductants in the feed is important to the success of this study whose scope is to interpret the Phase 2 data, extract the kinetic parameters of key reactions involving the carbon species, and develop a new DWPF melter off-gas chemistry model using those kinetic parameters.

The elemental and anion data reported in Table 2-1 and Table 2-2 was measured at the Process Science Analytical Laboratory (PSAL) of SRNL. The slurry samples were re-analyzed only for the anions by the Analytical Development (AD) of SRNL, and the results are compared in Table 2-3. For the 100% acid stoichiometry SRAT product, the agreement between the two lab results is quite good for the two main anions, nitrate and glycolate. Discrepancies in oxalate, formate and sulfate are not as important due to their much lower concentrations and thus have a relatively low impact on both REDOX and off-gas flammability. For the 125% acid stoichiometry SRAT product, the measured nitrate and glycolate concentrations by AD are larger than those by PSAL but the differences are still within 10%.

Table 2-3. Comparison of Anion Measurements by AD and PSAL.

	NO_3	$C_2H_3O_3$	SO_4	C_2O_4	COOH
	mg/Kg	mg/Kg	mg/Kg	mg/Kg	mg/Kg
100% Acid, SRAT Product					
AD Average	70,538	44,166	1,529	1,796	2,545
PSAL average	66,950	44,525	1,863	2,005	3,135
Δ (AD-PSAL)	5.4%	-0.8%	-17.9%	-10.4%	-18.8%
125% Acid, SRAT Product					
AD Average	91,303	47,153	1,651	1,723	1,073
PSAL average	84,850	43,500	2,695	2,155	<500
Δ (AD-PSAL)	7.6%	8.4%	-38.7%	-20.0%	-
125% Acid, 45%, 1X Antifoam					
AD Average	67,341	43,250	1,282	1,218	764
PSAL average	66,550	35,650	1,458	1,288	1,965
Δ (AD-PSAL)	1.2%	21.3%	-12.0%	-5.4%	-61.1%
100% Acid, 45%, 1X Antifoam					
AD Average	58,804	34,665	1,292	1,130	1,721
PSAL average	61,450	26,600	1,405	928	2,413
Δ (AD-PSAL)	-4.3%	30.3%	-8.0%	21.7%	-28.7%
100% Acid, 45%, 2X Antifoam					
AD Average	61,760	36,239	1,313	1,152	1,787
PSAL average	55,233	31,033	854	944	1,838
Δ (AD-PSAL)	11.8%	16.8%	53.8%	22.0%	-2.8%

The next 3 samples represent the actual feeds used in Phase 2, after each SRAT product was remediated and blended with Frit 418. It is clearly seen that the measured nitrate concentrations by PSAL and AD remain well within ±10% of each other; for the feed spiked with 2X antifoam, the difference is larger at 11%. However, the measured glycolate concentrations by AD are up to 30% higher than the PSAL data.

The TOC values of 7 different melter feeds were calculated from the measured anion data by AD and the results are compared in Table 2-4 against the measured values by the DWPF Analytical Laboratory (TOC_{DWPF}). The given anion data may be somewhat different from the reported analytical results because the former represents the charge-reconciled feeds. The antifoam values shown were calculated by assuming that 100% of antifoam added during the Sludge Receipt and Adjustment Tank (SRAT) and/or the Slurry Mix Evaporator (SME) processing remained in the feed. Another TOC values (TOC_{cruc}) were calculated based on the measured total carbon emission during batch melting of a slurry feed in an argon-purged crucible. Specifically, they were estimated by dividing the total mass of carbon emitted in the off-gas in mg by the initial batch weight of 0.01 kg.[17]

CEF1_Baseline is the NFA flowsheet feed used in Phase 1 and its calculated TOC (TOC_{calc}) is shown to be only 3% lower than the TOC_{DWPF} data while the TOC_{cruc} data was lower by 11%. The SB8-D3 series were also based on the NFA flowsheet. SB8-D3_Baseline was produced at 120% acid stoichiometry and contained less than 30% of the antifoam added to the baseline CEF Phase 1 (CEF1) or Phase 2 (CEF2) feed.[18] Its calculated TOC value from the anion data was practically identical to TOC_{DWPF} while TOC_{cruc} was 8% higher. Considering that all three TOC values (TOC_{calc}, TOC_{DWPF}, TOC_{cruc}) are in reasonable agreement for the two baseline NFA flowsheet feeds, it may be concluded that: (1) the TOC_{DWPF} data tracks the anion carbon data well, which is consistent with the trend seen earlier,[19] and (2) no significant degradation and subsequent loss of antifoam carbon (AC) occurred during the preparation of these simulated feeds, and (3) the TOC_{cruc} data based on the total carbon emission during batch melting in a crucible appears to be a viable option.

When SB8-D3_Baseline was spiked with 1,600 ppm of fresh AC, both TOC_{calc} and TOC_{cruc} were still close to TOC_{DWPF}, differing only by +5%. Despite the excellent agreement with an independent measurement, the carbon balance showed that the TOC_{cruc} data for this particular batch was 27% larger than TOC_{calc}.[17] In fact, the total carbon emissions measured during the eight batch melting tests using the argon-purged crucibles were consistently higher than those estimated from the analytical data by 15% - 40%.

When SB8-D3_Baseline was boiled before analysis (SB8-D3_1600ppm-AC Spike_Boiled), the resulting TOC_{calc} was 27% higher than TOC_{DWPF}. If all 27% is taken as the loss due to antifoam degradation during boil-up, it is equivalent to ~90% loss of antifoam, which is significantly higher than the 20% loss estimated earlier based on data from 15 SME batches.[19] The TOC_{cruc} data was even higher than TOC_{DWPF} by 35%, which suggests that TOC_{DWPF} could be at fault.

When SB8-D3_Baseline was spiked with 1,600 ppm of polyethylene glycol (PEG)-equivalent carbon and boiled, TOC_{calc} was 6% higher than TOC_{DWPF}. If all 6% is taken as the loss due to degradation, it is equivalent to a 29% loss of PEG carbon during boil-up, which is more in line with the earlier estimate.[19] On the other hand, TOC_{cruc} was 26% higher than TOC_{calc}, which is clearly outside the normal bounds of measurement errors so is in principle not feasible because TOC_{calc} assumes no loss of AC during boil-up and thus represents the theoretical maximum TOC. In addition, a quick scan of the listed TOC_{cruc} values for the SB8-D3 series feeds suggests that this particular data is likely at fault.

Table 2-4. Comparison of Measured vs. Calculated TOC in Various Feeds.

Sample	COOH[a] (mg/kg)	$C_2H_3O_3$[a] (mg/kg)	C_2O_4 (mg/kg)	Antifoam (mg/kg)	TOC_{calc}[b] (mg/kg)	TOC_{DWPF} (mg/kg)	Δ TOC (calc - DWPF)	TOC_{cruc}[c] (mg/Kg)	Δ TOC (crucible - DWPF)
CEF1_Baseline	46,098	0	12	3,125	13,873	14,352	-3%	12,789	-11%
SB8-D3_Baseline	54,393	0	2,624	875	15,668	15,883	-1%	17,209	8%
SB8-D3_1600ppm-AC Spike_Fresh[d]	54,393	0	2,624	4,062	17,268	16,427	5%	17,311	5%
SB8-D3_1600ppm-AC Spike_Boiled	54,393	0	2,624	4,062	17,268	13,599	27%	18,315	35%
SB8-D3_1600ppm-PEG C Spike_Boiled	54,393	0	2,624	4,062	17,268	16,352	6%	20,610	26%
CEF2_100% Acid-Baseline	1,751	34,494	1,236	2,936	13,322	16,199	-17%	16,178	0%
CEF2_100% Acid-1000ppm AC Spike	1,751	34,494	1,236	4,926	14,322	-	-	15,623	-

[a] Best possible match of AD results after charge reconciliation.
[b] Assumed 100% retention of antifoam carbon added.
[c] Calculated as the ratio of total carbon emitted during each run to initial slurry batch weight.
[d] AC stands for antifoam carbon, which makes up 50.27 wt% of antifoam.

Finally, TOC_{calc} for the baseline CEF Phase 2 feed is shown to be 18% lower than the TOC_{DWPF}, while the TOC_{cruc} was essentially identical to the TOC_{DWPF}. This result is significant because it means that the underestimation of TOC based on the anion carbon data for the NGA flowsheet feed is confirmed by two independent TOC measurements. In fact, as shown in the last column of Table 2-4, the agreement between the two TOC measurements is either excellent or reasonably good except for those spiked with excess carbons, which may be related to the large carbon imbalance in the crucible data. The potential cause for the underestimation of TOC is that the analytical method used did not detect all the glycolate ions due to their tendency to form complexes with normally insoluble metals and rendering them soluble, as shown by the results of charge reconciliation next. Another evidence of not detecting all the glycolate analytically comes from the fact that the total carbon emitted during the crucible run was ~40% more than the total carbon in the CEF2_100%_Acid-Baseline feed estimated from the anion data.[17]

2.2.3 *Charge Reconciliation*

The charge imbalances present in the 100% and 125% acid stoichiometry SRAT product data in Table 2-1 and Table 2-2, respectively, with the anion data replaced with the respective AD data shown in Table 2-3, were reconciled under the constraints of measured bulk properties, including pH, in the following steps:

1. Charge balance of supernate data: The given Na data was adjusted up by 14% and 6% for the 100% and 125% acid stoichiometry SRAT products, respectively. On a slurry basis, these adjustments were equivalent to a 9% and 13% increase above the elemental Na data by Inductively Coupled Plasma-Mass Spectrometry (ICP-MS) for the 100% and 125% acid stoichiometry, respectively. As explained later in the report, the reason for replacing the PSAL anion data with the AD anion data was to reduce the shortfall in TOC compared to the TOC_{DWPF}.

2. Calculation of soluble fractions of metals: The elemental data given in mg/L supernate was converted to per L slurry basis and compared to the elemental data of the slurry. The results are compared in Table 2-5 to those calculated for the NFA flowsheet feed used in Phase 1. It is clearly seen that the solubility of these normally insoluble metals increases from the NFA to NGA flowsheet and with increasing acid stoichiometry, which may be explained in terms of the metal-glycolate complex formation.

Table 2-5. Soluble Fractions in Charge Reconciled SRAT Products.

Elements	Phase 1*	100% acid	125% acid
Fe	0.0%	0.6%	5.2%
Al	0.1%	1.1%	3.2%
Mn	58.7%	88.1%	82.7%
Ca	98.8%	98.1%	100.0%
Mg	100.0%	98.0%	100.0%
Ni	24.4%	38.1%	76.2%
Cr	0.2%	0.4%	1.0%
Cu	21.4%	18.6%	64.4%
Ti	0.0%	0.3%	2.9%
Zn	9.4%	20.8%	54.1%
S	88.8%	95.5%	100.0%

* At 120% acid stoichiometry

3. Soluble metal-anion pairing: Most soluble metals in Table 2-5 were paired with NO_3, $C_2H_3O_3$ and COOH at their reported molar anion ratios.

4. Adjustment of glycolate IC data: The glycolate data for the SRAT product slurry in Table 2-1 and Table 2-2 was adjusted until the measured glycolate data for the post-remediation feed samples was matched.

5. Equilibrium dissociation of medium acids: The free acid (undissociated) fractions of the glycolate and formate IC data at a given pH were calculated for each acid-H_2O binary solution using their respective pK_a values of 3.83 and 3.75 at 25 °C.

6. Na partitioning: The total Na estimated in Step 1 was distributed among NO_3, C_2O_4, SO_4, PO_4, Cl, and the remaining $C_2H_3O_3$ and COOH after the acid dissociation calculations in Step 5. Per the SB6I simulant recipe, no insoluble Na was assumed to be present in either SRAT product.

7. Adjustment of equilibrium dissociation: The free acid fractions calculated in Step 5 were adjusted by iteration starting from Step 4 until no more surplus anions were left in Step 6.

The compositions of the charge-reconciled 100% and 125% acid stoichiometry SRAT Products are shown in Table 2-6 and Table 2-7, respectively, in a neutral species form. The calculated total insoluble and soluble solids are shown to be 1-7% larger than their respective measured data for both feeds. The concentrations of free glycolic and formic acids shown in Table 2-6 represent 2.2% and 1.2% of their respective IC data at the measured pH of 5.03. As shown in Figure 2-1, these free acid fractions are smaller than those calculated for the $C_2H_4O_3$-H_2O and HCOOH-H_2O binary solutions by 63% and 76%, respectively. The large reduction in free glycolic acid fraction was expected as it chelates polyvalent metal ions, which would shift the equilibrium toward more dissociation. Although formic acid forms little or no chelates, its dissociation equilibrium was still adjusted by the same factor as that of glycolate acid; however, this had little impact on the charge reconciliation as the concentration of formate was up to 43X smaller than that of glycolate.

When the pH was lowered to 3.21 for the 125% acid stoichiometry SRAT product, the calculated free acid fractions were increased to 25.0% and 13.3% of the measured glycolate and formate IC data, respectively, which correspond to 31% and 17% of those calculated for the $C_2H_4O_3$-H_2O and HCOOH-H_2O binary solutions. Both formic and glycolic acids (along with free H_2O in the feed) are listed as volatiles, as their reported boiling points are almost identical at 101 °C and 100 °C, respectively.[20] Unlike formic acid, however, glycolic acid is also known to decompose at >100 °C rather than volatilize due to its low vapor pressure.[21] Thus, the term “volatiles” is used here to be inclusive of those species with low-decomposition temperatures.

Since the presence of antifoam molecules cannot be detected directly by the analytical methods used, its concentration was set based on its addition recipe, 15.5 kg per 5,000 kg of SB6I simulant or 0.108 kg/kg Fe,[12,13] and assuming 100% retention during the SRAT processing at Harrell Industries, which included ~8 hours of boil-up. Furthermore, the oxalate was added as $Na_2C_2O_4$ at a rate of 0.023 kg/kg Fe. However, the measured C_2O_4 by IC was 2X the amount added per recipe and the increasing trend was consistent with the data.[36] The oxalate concentrations shown in Table 2-6 and Table 2-7 are based on the IC data. The phosphate was added as $Na_3PO_4 \cdot 12H_2O$ at a rate of 0.021 g/g Fe, and its IC data was below detection, i.e., <500 mg/kg in both SRAT products. Thus, its concentration was derived from the ICP-MS elemental data for P, assuming it to be 100% soluble, and the resulting phosphate concentrations were 573 and 554 mg/kg for the 100% and 125% acid stoichiometry SRAT products, respectively, both slightly above the detection limit.

Table 2-6. Composition of Charge Reconciled 100% Acid Stoichiometry SRAT Product.

Insoluble Solids:	g/L slurry	Soluble Solids:	g/L slurry	Soluble Solids:	g/L slurry
Fe(OH)3	93.846	Ca(COOH)2	0.249	Na2SO4	3.366
Al(OH)3	89.314	Ca(C2H3O3)2	4.271	Ni(COOH)2	0.199
MnO2	2.987	Ca(NO3)2	6.388	Ni(C2H3O3)2	3.284
Ca(OH)2	0.089	Fe(COOH)3	0.030	Ni(NO3)2	4.980
Mg(OH)2	0.096	Fe(C2H3O3)3	0.520	Zn(COOH)2	0.004
Ni(OH)2	6.684	Fe(NO3)3	0.776	Zn(C2H3O3)2	0.062
Cr(OH)3	0.802	Al(COOH)3	0.061	Zn(NO3)2	0.095
Cu(OH)2	0.360	Al(C2H3O3)3	1.107	H4SiO4	2.313
K2O	0.004	Al(NO3)3	1.621	Total Soluble	218.739
TiO2	0.196	Cu(COOH)2	0.004	Measured	206.028
SiO2	5.578	Cu(C2H3O3)2	0.064	Δ (%)	6.17%
Sn(OH)2	0.089	Cu(NO3)2	0.097		
Zn(OH)2	0.308	KCOOH	0.047	Volatiles:	
BaSO4	0.525	KC2H3O3	0.749	HCOOH	0.039
ZrO2	0.000	KNO3	1.149	C2H4O3	1.387
CaSO4	0.000	Mg(COOH)2	0.275	H2O	825.072
CaC2O4	0.000	Mg(C2H3O3)2	4.923		
antifoam	5.309	Mg(NO3)2	7.257	Total Solids	424.924
Total Insoluble	206.185	Mn(COOH)2	1.109	Measured	403.839
Measured	197.811	Mn(C2H3O3)2	18.428	Δ (%)	5.56%
Δ (%)	4.23%	Mn(NO3)2	27.877		
		NaCl	0.861		
		NaF	0.000		
		NaCOOH	2.791		
		NaC2H3O3	47.281		
		NaNO3	71.050		
		Na3PO4	1.788		
		Na2C2O4	3.422		
		Na2CO3	0.242		

Table 2-7. Composition of Charge Reconciled 125% Acid Stoichiometry SRAT Product.

Insoluble Solids:	g/L slurry	Soluble Solids:	g/L slurry	Soluble Solids:	g/L slurry
Fe(OH)3	87.723	Ca(COOH)2	0.092	Na2SO4	3.065
Al(OH)3	90.119	Ca(C2H3O3)2	3.333	Ni(COOH)2	0.129
MnO2	4.181	Ca(NO3)2	8.286	Ni(C2H3O3)2	4.490
Ca(OH)2	0.000	Fe(COOH)3	0.088	Ni(NO3)2	11.320
Mg(OH)2	0.000	Fe(C2H3O3)3	3.208	Zn(COOH)2	0.003
Ni(OH)2	2.442	Fe(NO3)3	7.955	Zn(C2H3O3)2	0.112
Cr(OH)3	0.768	Al(COOH)3	0.063	Zn(NO3)2	0.284
Cu(OH)2	0.143	Al(C2H3O3)3	2.427	H4SiO4	0.944
K2O	0.000	Al(NO3)3	5.908	Total Soluble	230.057
TiO2	0.181	Cu(COOH)2	0.004	Measured	214.851
SiO2	6.716	Cu(C2H3O3)2	0.145	Δ (%)	7.08%
Sn(OH)2	0.000	Cu(NO3)2	0.367		
Zn(OH)2	0.172	KCOOH	0.015	Volatiles:	
BaSO4	0.476	KC2H3O3	0.490	HCOOH	0.183
ZrO2	0.430	KNO3	1.249	C2H4O3	16.290
CaSO4	0.000	Mg(COOH)2	0.091	H2O	810.457
CaC2O4	0.000	Mg(C2H3O3)2	3.434		
antifoam	4.962	Mg(NO3)2	8.413	Total Solids	444.661
Total Insoluble	198.313	Mn(COOH)2	0.343	Measured	411.373
Measured	196.521	Mn(C2H3O3)2	11.986	Δ (%)	8.09%
Δ (%)	0.91	Mn(NO3)2	30.139		
		NaCl	0.000		
		NaF	0.000		
		NaCOOH	0.929		
		NaC2H3O3	33.078		
		NaNO3	82.623		
		Na3PO4	1.752		
		Na2C2O4	3.293		
		Na2CO3	0.000		

2.2.4 *Remediation and Frit Addition*

The charge-reconciled SRAT product compositions shown in Table 2-6 and Table 2-7 were next remediated to reduce the observed discrepancies between the REDOX of the as-received SRAT products and their respective targets. Specifically, the 100% acid stoichiometry SRAT product was made more oxidizing by adding 2.0 kg of 49.4 wt% nitric acid to each drum containing 170 lb of SRAT product following the strategy outlined in Table 2-8 and, as a result, its measured REDOX was decreased from 0.47 to 0.26 after remediation. For the 125% acid stoichiometry SRAT product, 1.5 kg of 70 wt% glycolic acid was added to each drum containing 200 lb of SRAT product, and its REDOX was increased from <0.02 to 0.26 after remediation. Frit 418 was added along with the acids at the target of 36 wt% waste loading (WL). The remediated products were fed at 45% total solids during the steady state tests, while the 100% acid stoichiometry feed at 42% total solids was fed during the surge testing.

Table 2-8. Remediation Strategy and Frit Addition.

Acid Stoichiometry	100%	100%	125%
Target Total Solids (wt%)	45	42	45
Target Waste Loading (wt%)	36	36	36
Drum Mass (lb)	184	184	214
Drum Tare (lb)	14	14	14
SRAT Product Mass (lb)	170	170	200
Frit 418 added (kg/drum)	24.7	24.7	28.6
Nitric Acid added (kg/drum)	2	2	0
- strength (wt%)	49.4	49.4	49.4
Glycolic Acid added (kg/drum)	0	0	1.5
- strength (wt%)	70	70	70
H_2O added (kg/drum)	8.4	19.7	10.5
Redox (closed crucible-ramp)			
- before remediation	0.47	0.47	<0.02
- after remediation	0.25	0.25	0.25
pH			
- before remediation	5.03	-	3.21
- after remediation & frit addition	3.82	-	3.34

2.2.5 *Final Adjustment of Phase 2 Feeds*

Although the as-received SRAT products were charge reconciled using the anion data by AD and remediated by adding either nitric or glycolic acid according to the recipe, the analytical results of the remediated feeds showed that the calculated glycolate concentrations were still lower than the post-remediation measured data by AD. Thus, an additional 14% and 8.5% glycolic acid was added to the 100% and 125% acid stoichiometry feeds, respectively, to match the AD data (Step 4 in charge reconciliation). As the pH shifted upon the acid addition, the free acid fractions were re-estimated using Eq. (1), which was derived by the regression of the calculated free acid fractions during the charge reconciliation, as shown by the blue dotted line in Figure 2-1:

$$C_2H_4O_3\ Fraction = \ 18.648\ e^{-1.343\ pH}, \ pH \geq 3 \tag{1}$$

It turns out that for the 100% acid stoichiometry feed there was not enough free glycolic acid to satisfy the equilibrium demand per Eq. (1) at pH = 3.82, which necessitated the conversion of glycolate salts into nitrate salts at the expense of nitric acid as follows:

$$NaC_2H_3O_3 + HNO_3 \rightarrow \ NaNO_3 + \ C_2H_4O_3 \tag{2}$$

In fact, there would have been no shortage of free glycolic acid had Eq. (2) been allowed to occur during remediation. Instead, it was deferred until the calculation of the cold cap model input vectors shown later in Table 4-1 and Table 4-2.

For the 125% acid stoichiometry feed, there was a surplus of glycolic acid beyond that predicted by Eq. (1) at pH = 3.34 as it was remediated with the addition of glycolic acid. The excess glycolic acid was input into the cold cap model and decomposed per Eq. (8), thereby reflecting the increased reducing potential of feed.

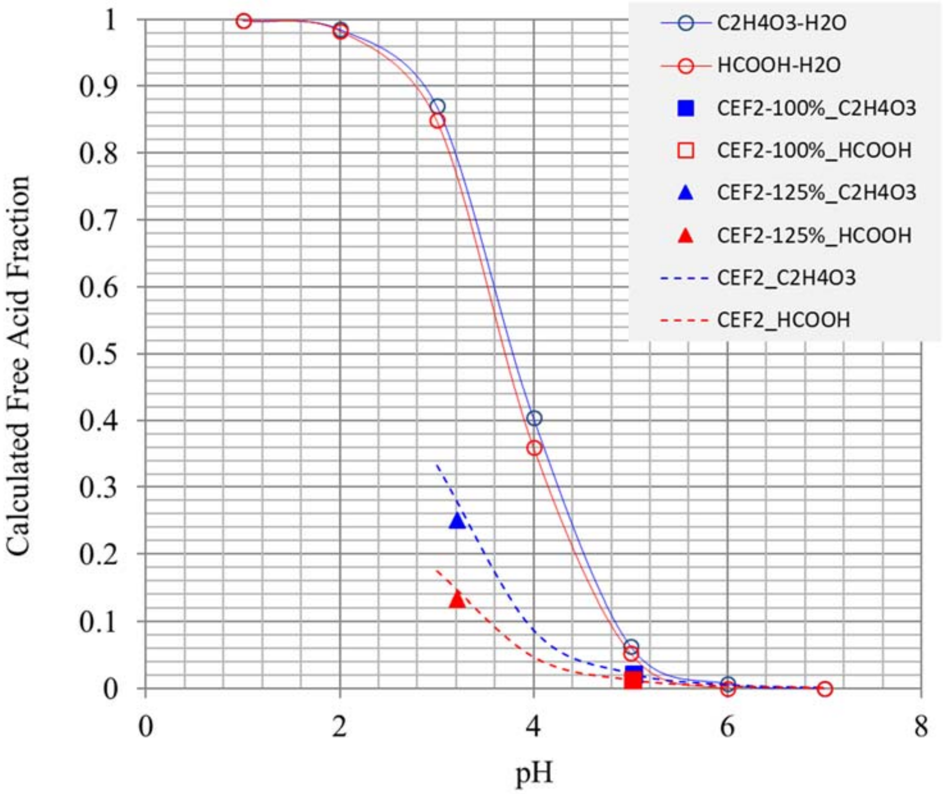

Figure 2-1. Calculated Free Acid Fraction vs. pH.

The concentrations of nitrate and glycolate in the final 100% and 125% acid stoichiometry feeds used during the Phase 2 CEF run are compared in Table 2-9 along with the TOC distributions. As expected, the calculated glycolate values are essentially identical to those measured. However, the calculated TOC is still shown to be 17.2% and 9.2% lower than the measured data for the 100% and 125% acid stoichiometry feeds, respectively. If the measured TOC data is considered accurate, the current analysis to derive the global kinetic parameters based on the underestimated TOC is conservative because the predicted concentrations of H_2 and CO in the calcines gases will be lower, while the target concentrations of H_2 and CO in the off-gas are set at the measured data regardless. Thus, the resulting rate constants for the H_2/CO combustion in the vapor space will be lower, which would make the predicted H_2/TOC and CO/TOC ratios conservatively high.

It was noted earlier that the TOC_{DWPF} data in Table 2-4 tracks the anion carbon data well, which is consistent with the trend seen in the DWPF SME samples.[19] Noting that these feeds were either simulated or actual DWPF feeds all based on the NFA flowsheet, the discrepancies seen between the calculated and measured TOC values in Table 2-9 seems to suggest that the current analytical method of quenching the sample with caustic to pH=14 followed by 5,000X dilution using water may still be under-estimating the total glycolate.

Table 2-9. Comparison of Final 100% and 125% Acid Stoichiometry Feeds to the Melter.

Analyte	100% Acid (mg/kg)	125% Acid (mg/kg)
NO_3		
- calculated	57,175	63,152
- measured by AD	58,804	67,341
$C_2H_3O_3$ total		
- calculated	34,645	43,255
- measured by AD	34,665	43,250
- $C_2H_3O_3$ (free)	763	16,950
TOC		
- calculated	13,362	15,744
- measured (TOC_{DWPF})	16,199	17,343
- Δ (calculated-data)	-17.5%	-9.2%
TOC Distributions:		
- formate	462	172
- glycolate	10,849	8,492
- oxalate	337	325
- free formic	6	26
- free glycolic	241	5,354
- antifoam	1,467	1,374

2.3 Phase 2 Data

The Phase 2 CEF run proceeded in 3 stages. In the first stage, a total of 26 steady state runs were made by feeding each acid stoichiometry feed (100% and 125%) at 6 to 8 different CEF vapor space temperatures (T_{vs}) under bubbled (B) and non-bubbled (NB) conditions. For example, the 100%_B case was run at 8 different T_{vs} under bubbled conditions with the 100% acid stoichiometry feed containing normal (1X) level of antifoam. In Stage 2, the CEF was run with the 100% acid stoichiometry feed containing normal (1X) level of antifoam for 4 days under bubbled and for 1 day under non-bubble conditions to collect off-gas surge data. In Stage 3, the CEF was run with the 100% acid stoichiometry feed containing 2X the normal level of antifoam under non-bubbled conditions at 6 different T_{vs} (100%_NB_2X). A detailed description of the Phase 2 run is given elsewhere along with the full set of data on the CEF and off-gas system parameters, off-gas analysis and analytical results on the feed, glass, and condensate samples.[3]

2.3.1 *Steady State Data*

The average readings of some of the key CEF operating variables during the steady state runs and the corresponding off-gas data are given in Table 2-10 and Table 2-11, respectively. A more complete list of steady state data is given in Appendix, including additional CO_2 data by FTIR and Gas Chromatography (GC) along with the standard deviation and the maximum/minimum of each average data point. Methane was also monitored but its concentration was less than 10 ppm throughout except during the 100%_NB_2X run at T_{vs} = 600 °C. No other flammable gases were detected besides H_2, CO and CH_4. The six steady state data points taken during the 100%_NB_2X run are not included in this report, as they were not used in the model development. At a given T_{vs}, both H_2 and CO readings were higher under bubbled than non-bubbled conditions. This was expected because the steady state feed rates were always higher under bubbled than non-bubbled conditions at comparable T_{vs}, as shown in Table 2-10.

Table 2-10. Average CEF Operating Conditions During Phase 2 Steady State Runs at 1X Antifoam.

SS Run	T_{vs}	Feed Rate	Ar Flow	FC Air	Canty Camera Air	SRNL Camera Air	VS Air Purge	FC Exit Temp	Melter Pressure	FC Exit Pressure	OGCT Pressure	Melt Temp
	(°C)	(g/min)	(scfm)	(scfm)	(scfm)	(scfm)	(scfm)	(°C)	("H_2O)	("H_2O)	("H_2O)	(°C)
125%_B	705	221.38	0.376	15.64	7.78	0.72	0.65	366	-5.22	-5.97	-1.1	1,033
	625	161.29	0.380	15.92	7.78	0.64	0.68	299	-5.35	-5.99	-0.5	1,032
	481	113.53	0.378	15.88	7.70	0.57	15.12	256	-4.90	-6.20	-4.8	1,025
	415	110.95	0.363	16.08	7.71	0.49	22.28	234	-4.74	-6.42	-7.2	1,029
	360	92.88	0.380	8.54	7.72	0.49	40.14	244	-3.48	-5.91	-10.8	1,011
	270	72.15	0.197	6.20	7.58	0.50	50.68	203	-1.16	-3.85	-11.5	1,035
125%_NB	709	99.60	0.004	15.73	7.61	0.69	0.45	325	-5.47	-6.02	-0.2	1,083
	604	105.85	0.006	16.04	7.97	0.58	0.25	279	-5.29	-6.00	-2.6	1,060
	486	87.60	0.005	15.89	7.92	0.51	0.28	217	-5.51	-6.16	-2.4	1,059
	393	51.07	0.004	15.73	7.58	0.55	14.98	212	-5.46	-6.56	-4.8	1,085
	351	44.27	0.005	15.93	7.67	0.52	20.89	200	-5.04	-6.43	-6.3	1,083
	302	35.08	0.005	15.91	7.68	0.46	29.62	183	-4.96	-6.81	-9.0	1,084
100%_B	750	194.31	0.379	15.28	7.74	0.66	0.53	376	-4.67	-5.39	-1.0	1,055
	705	170.49	0.379	15.25	7.72	0.67	0.52	358	-4.81	-5.50	-1.0	1,050
	607	166.89	0.379	15.20	7.70	0.54	0.44	292	-4.96	-5.54	-0.8	1,053
	592	146.21	0.372	15.32	7.78	0.57	0.51	285	-4.66	-5.25	0.0	1,042
	521	126.92	0.373	15.34	7.77	0.54	0.49	232	-4.70	-5.22	-0.2	1,035
	471	122.69	0.374	15.32	7.73	0.56	6.09	235	-4.42	-5.22	-1.6	1,041
	373	101.80	0.379	15.50	7.48	0.48	25.94	219	-5.06	-6.96	-11.0	1,025
	323	88.29	0.378	6.12	7.38	0.48	45.90	224	-1.13	-3.61	-12.0	1,031
100%_NB	697	125.22	0.003	16.14	7.36	0.71	0.32	323	-5.27	-5.77	-0.3	1,086
	600	98.54	0.005	16.55	7.45	0.64	0.32	268	-5.70	-6.15	-0.3	1,085
	496	84.48	0.005	16.80	7.50	0.59	0.33	214	-6.00	-6.42	-0.3	1,068
	410	55.75	0.006	16.83	7.54	0.52	13.22	209	-5.46	-6.49	-4.2	1,074
	344	47.59	0.003	16.10	7.49	0.49	27.93	201	-4.46	-6.28	-8.9	1,078
	326	42.33	0.003	9.67	7.50	0.51	34.77	217	-4.02	-5.99	-8.5	1,079

Table 2-11. Average Off-Gas Data During CEF Phase 2 Steady State Runs at 1X Antifoam.

SS Run	T_{vs}	H_2 (MS)	H_2 (GC)	CH_4 (FTIR)	CO (FTIR)	CO_2 (MS)	NO (MS)	NO (FTIR)	NO_2 (MS)	NO_2 (FTIR)	N_2O (FTIR)	NO_x (MS)	NO_x (FTIR)
	(°C)	(ppm)	(ppm)	(ppm)	(ppm)	(vol %)	(ppm)	(ppm)	(ppm)	(ppm)	(ppm)	(ppm)	(ppm)
125%_B	705	43	44	3	224	0.919	2,156	3,484	1,430	768	391	3,586	4,252
	625	70	73	8	180	0.676	1,892	2,556	981	490	266	2,873	3,046
	481	42	48	6	32	0.312	917	1,208	388	178	106	1,305	1,387
	415	28	32	4	23	0.245	793	978	364	158	90	1,156	1,135
	360	18	21	2	22	0.183	498	618	228	102	68	727	720
	270	19	18	2	19	0.162	441	545	184	77	59	624	622
125%_NB	709	13	15	1	119	0.431	1,360	1,721	607	267	219	1,966	1,988
	604	46	43	3	119	0.440	1,377	1,666	824	336	222	2,201	2,003
	486	83	75	7	55	0.431	1,275	1,530	704	279	189	1,979	1,809
	393	25	22	2	14	0.190	515	635	271	142	75	786	777
	351	16	16	2	11	0.157	374	459	279	172	56	653	631
	302	12	8	2	6	0.119	332	404	213	121	32	545	525
100%_B	750	7	10	0	105	0.686	1,990	2,856	1,042	532	187	3,032	3,389
	705	19	23	1	161	0.659	1,932	2,924	1,091	575	220	3,023	3,498
	607	43	45	6	75	0.504	1,515	2,091	707	348	144	2,222	2,439
	592	37	39	4	109	0.512	1,670	2,334	866	445	165	2,536	2,780
	521	32	34	5	63	0.489	1,500	2,039	806	423	139	2,305	2,461
	471	31	33	4	55	0.399	1,295	1,716	673	347	115	1,968	2,063
	373	18	17	3	20	0.218	685	864	340	156	56	1,024	1,020
	323	13	12	2	18	0.174	545	674	268	121	45	812	795
100%_NB	697	17	15	0	117	0.476	1,445	2,126	671	385	152	2,116	2,511
	600	23	24	2	85	0.355	1,137	1,585	518	270	125	1,655	1,855
	496	19	20	4	26	0.297	994	1,314	456	218	96	1,449	1,531
	410	8	10	2	8	0.163	502	633	244	107	46	746	740
	344	6	1	1	4	0.118	307	364	196	105	29	503	469
	326	6	1	1	4	0.117	284	348	252	160	30	536	508

Both H_2 and CO readings are shown to decrease with decreasing T_{vs} below ~600 °C, and this is reflection of the net effect of several competing changes occurring simultaneously. First, as T_{vs} decreased, the steady state feed rate decreased, which would lower the H_2 and CO readings, as noted above. Second, as T_{vs} decreased, the global combustion kinetics of H_2 and CO would slow down, resulting in higher H_2 and CO readings. Third, as the air purge into the vapor space was increased steadily to lower T_{vs} below ~500 °C, it would lower the H_2 and CO readings by dilution but the shortened gas residence time for the vapor space combustion would increase them at the same time. Thus, analysis of H_2 and CO data is not straightforward as it requires a comprehensive mass/heat balance model of both the CEF operating and off-gas data, as shown later in the report.

Although not shown, the rate of H_2 evolution during the 100%_NB run with 2X spiked antifoam was practically indistinguishable from that with no antifoam spike, except at T_{vs} around 600 °C, and in general lower than that during the 125%_NB run with no antifoam spike. This was a somewhat surprising result as doubling the antifoam addition did not have any appreciable effect on H_2; however, it appears to be consistent with the results from the batch-melting study in an argon-purged crucible shown in Figure 2-2.[17]

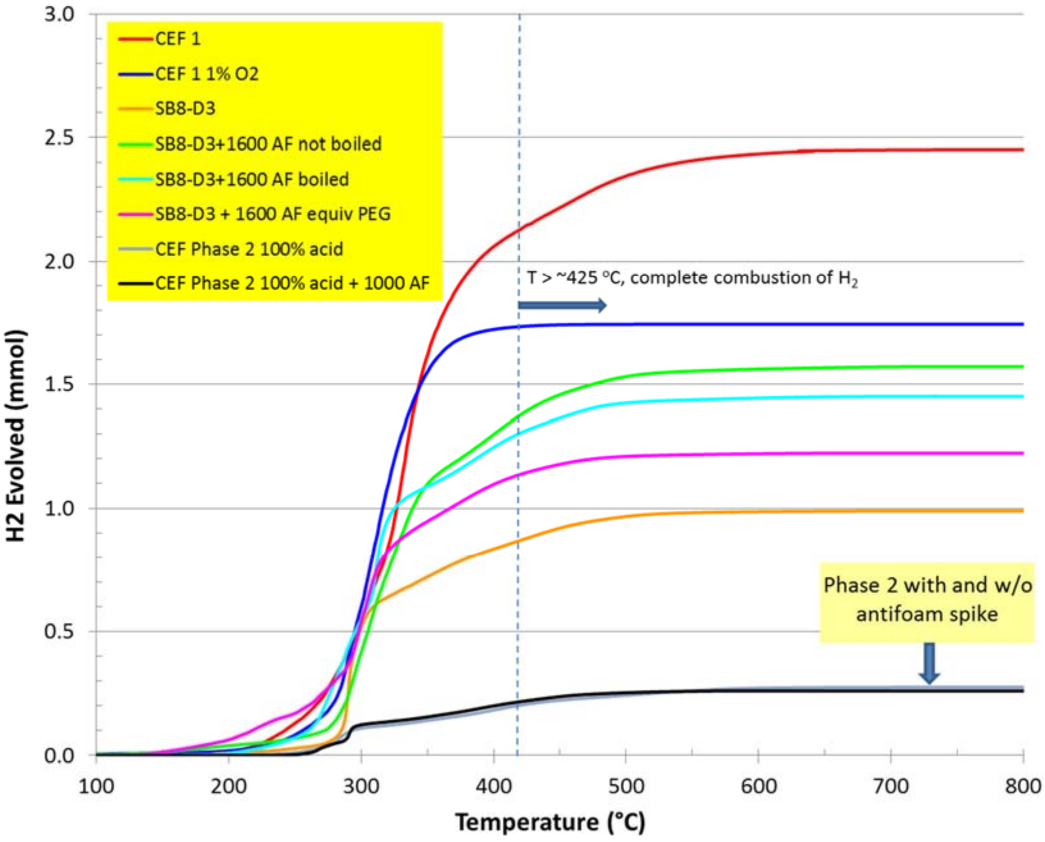

Figure 2-2. Cumulative H_2 Evolution during Batch-Melting in Ar-Purged Crucible [Ref. 17].

2.3.2 *Comparison of H_2/CO Data with Phase 1*

The measured concentrations of H_2 and CO for the 100%_NB case are compared in Figure 2-3 and Figure 2-4 to those measured during Phase 1 in terms of H_2/TOC and CO/TOC molar ratios, respectively. These ratios represent the measure of relative flammability potential of each feed normalized per mole of carbon fed, thereby removing the effect of feed rate. The 100%_NB data was chosen because the Phase 1 feed was also prepared at ~100% acid stoichiometry and run under non-bubbled conditions.

Figure 2-3 shows that at $T_{gas} < \sim500$ °C each carbon in the NGA flowsheet feed produced ≤ ¼ of the H_2 produced by each carbon in the NFA flowsheet feed under non-bubbled conditions. As T_{gas} increased above 500 °C, the difference between the H_2/TOC ratios of the two feeds narrowed quickly but the NGA flowsheet ratios remained < ½ of those of the NFA flowsheet. As the potential for melter off-gas flammability remains low until T_{gas} decreases below 400 °C, it can be concluded that on a per carbon basis the NGA flowsheet feed has only ¼ of the off-gas flammability potential of the NFA flowsheet feed, which can be attributed to the fact that the former has a 3.6X higher nitrate (oxidant) than the latter.

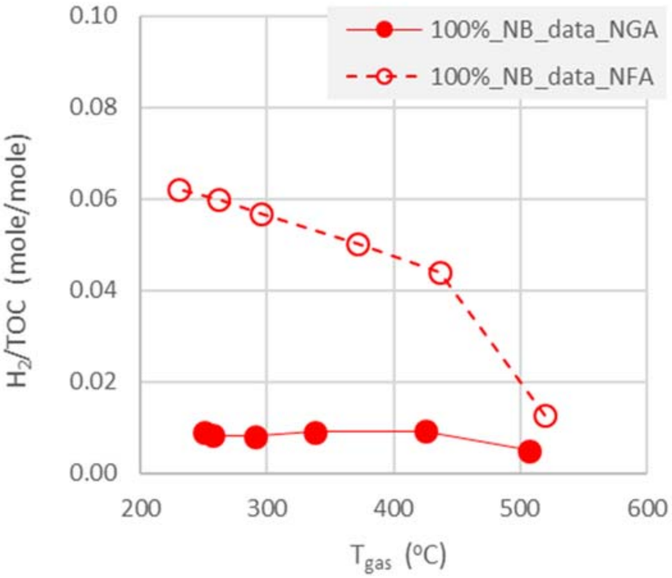

Figure 2-3. Measured H_2/TOC Ratios with NGA and NFA Flowsheet Feeds.

In Figure 2-4, the CO/TOC profile for the NGA flowsheet feed is shown to continuously decrease with decreasing temperature except at the lowest T_{gas}, while that of the NFA flowsheet feed started to level off at $T_{gas} = \sim370$ °C, thus rendering it more flammable than the NGA flowsheet feed. For example, at $T_{gas} = 300$ °C, each carbon in the NGA flowsheet feed produced less than ½ of the CO produced by each carbon in the NFA flowsheet feed. As T_{gas} increased above 370 °C, the two CO/TOC ratios remained essentially equal until T_{gas} was near 500 °C. Thus, even without taking credit for the lower CO of the NGA flowsheet feed at $T_{gas} < 370$ °C, it is concluded that the overall flammability potential of the NGA flowsheet feed would be ¼ that of the NFA flowsheet feed.

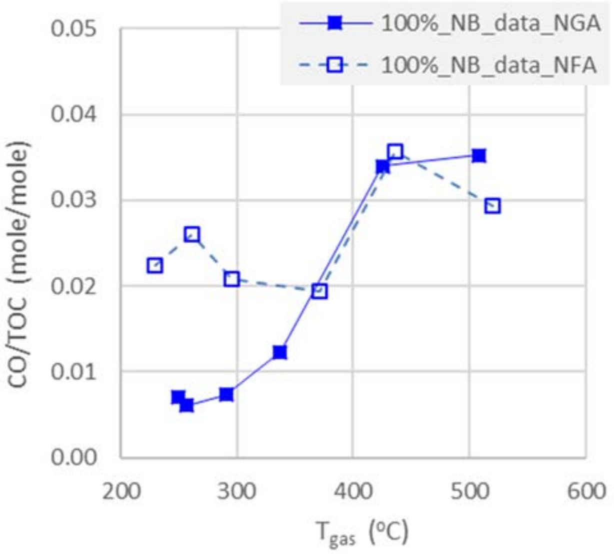

Figure 2-4. Measured CO/TOC Ratios with NGA and NFA Flowsheet Feeds.

In Table 2-11, the measured concentrations of H_2 and CO under bubbled conditions are clearly shown to be higher than their counterparts under non-bubbled conditions, which is attributed to the higher feed rates afforded under bubbled conditions. In terms of the H_2/TOC ratio, however, bubbling is shown in Figure 2-5 to have little or no impact at all T_{gas}, which indicates that each mole carbon in the 100% acid stoichiometry feed produced the same moles of H_2 regardless of bubbling or not. In terms of CO/TOC ratio, bubbling is shown in Figure 2-6 to have a modest but opposite impact at T_{gas} ~ 400°C. Although not shown, the impact of bubbling on both H_2/TOC and CO/TOC ratios appeared to be within the uncertainty of data for the 125% acid stoichiometry feed, i.e., no significant impact. No direct comparison could be made to the NFA flowsheet feed due to lack of bubbled data during Phase 1.

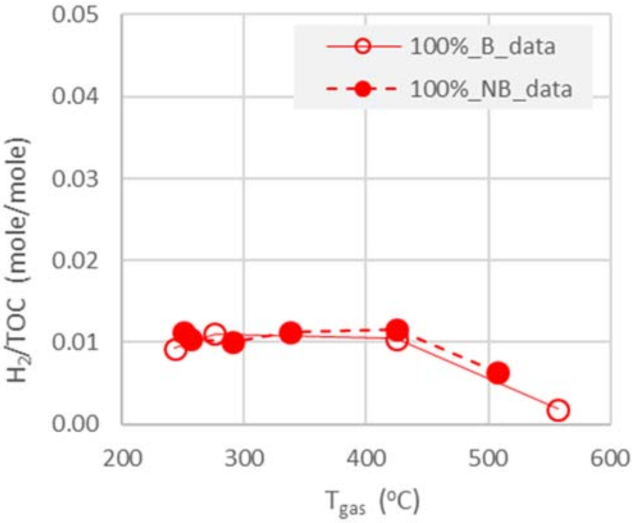

Figure 2-5. Impact of Bubbling on H_2/TOC Ratio (100%) for the NGA flowsheet.

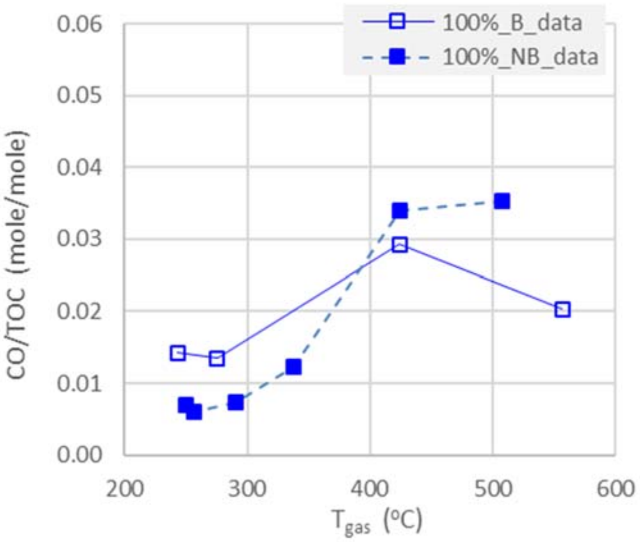

Figure 2-6. Impact of Bubbling on CO/TOC Ratio (100%) for the NGA flowsheet.

2.3.3 *Off-Gas Surge Data*

The number of pressure spikes and magnitudes of those spikes measured during Phase 2 are compared to those measured during the 2010 CEF run in Table 2-12. It is clearly shown that under bubbled conditions the NGA flowsheet feed produced pressure spikes < 2 "H_2O at an order of magnitude higher frequency than the NFA flowsheet feed. However, pressure spikes of these small magnitudes are not expected to pose any significant operational difficulties in the DWPF, considering that the DWPF melter is equipped with a fast-acting pressure control system. Note that the CEF pressure spike data in Table 2-12 was obtained in the absence of pressure control system and thus unmodulated, which enabled the surge magnitudes to be calculated directly from the measured pressure drop and off-gas data, as shown later in the report.

Table 2-12. Number of Pressure Spikes during CEF Runs.

Pressure Spike above Baseline ("H_2O)	Bubbled		Non-bubbled	
	Formic	Glycolic	Formic	Glycolic
	2010	2014	2010	2014
1 - 2	98	1,164	28	1
2 - 3	42	43	15	0
3 - 4	27	15	3	0
4 - 5	7	6	1	0
> 5	18	14	0	1
Total	192	1,242	47	2
Test Duration (day)	4.3	4	2.5	1
Frequency (#/day)	45	311	19	2

By contrast, the NGA flowsheet feeds produced almost no pressure spikes under non-bubbled conditions, whereas the difference between bubbled and non-bubbled pressure spike frequencies during the Phase 1 run with the NFA flowsheet feed is shown to be not nearly as large. However, considering that a majority of the reported pressure spikes during the Phase 1 run occurred while the system components were still being checked out and fine-tuned, the actual difference between bubbled and non-bubbled spikes of the NFA flowsheet feed was likely to be larger than the data shown in Table 2-12.[6] One of the two rare pressure spikes measured during the non-bubbled surge test was in excess of 5 "H_2O but lasted for only 13 seconds, which is too short a duration to have any significant impact on the off-gas flammability.

The NGA flowsheet feed produced pressure spikes > 2 "H_2O at about the same frequency as the NFA flowsheet feed, including those > 5 "H_2O, and the largest pressure spike measured during Phase 2 under bubbled conditions was in excess of 13 "H_2O from the baseline -5 to +8.3 "H_2O, as shown in Figure 2-7. By comparison, the largest pressure spike measured during the Phase 1 run was 10” H_2O from baseline -5 to +5 "H_2O, which was subsequently used to set the current off-gas surge basis of 9X normal condensable and 5X normal non-condensable flows (9X/5X).

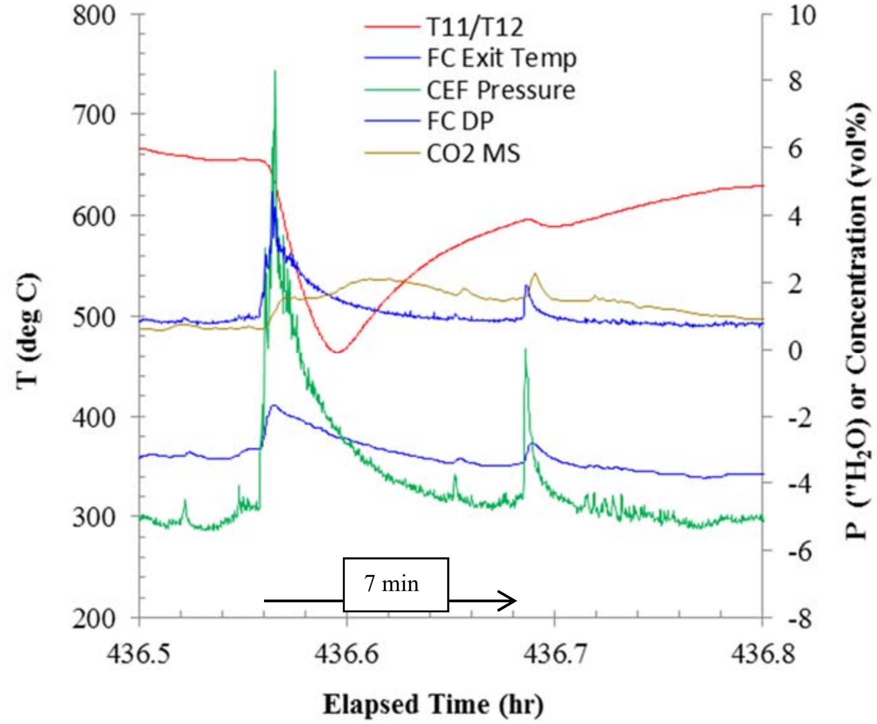

Figure 2-7. +13 "H_2O Pressure Spike during Phase 2 Bubbled Test with 100% Feed.

In fact, an even larger pressure spike in excess of +20 "H_2O also occurred during Phase 2 but it lasted only for ~5 sec, which is too short a duration to have any impact on the off-gas flammability or trigger a switchover to the backup off-gas system under the current DWPF Distributed Control System (DCS) logic. However, it still had an adverse impact on the CEF operation as it caused a significant off-gas carryover leading to the exhauster failure. For the +13 "H_2O spike shown in Figure 2-7, its key attributes such as the instantaneous ascend at the onset but a more gradual decent after the peak and the overall duration matched closely those of the DWPF design basis melter off-gas surge profile:[6]

- At time zero, the flow rates of condensable and non-condensable gases instantly increase to 9 times (9X) and 5 times (5X) the nominal, respectively, then immediately decrease linearly to 30% of their respective peak values during the first minute and further decrease linearly to 1.0 times the normal values (1X) during the next 7 minutes.

The measured T_{vs} fell by 240 °C due to a sudden surge of steam ejected from the cold cap, which is a clear indication of how large the pressure spike was, as T_{vs} rarely drops that much. As Figure 2-7 depicts the largest pressure spike observed during Phase 2 with any significant duration, the +13 "H_2O spike was designated as the baseline off-gas surge for the NGA flowsheet operation. The profiles of pressure drop across the film cooler (ΔP_{FC} or FC DP) and CO_2 in the off-gas are re-highlighted in Figure 2-8 as they serve as the basis for determining the magnitudes of the associated condensable and non-condensable flow surges, respectively.

Specifically, as the off-gas flow is directly proportional to ΔP_{FC} and the pressure spike is caused mostly by a surge in the condensable flow, which consists of free H_2O and volatiles in the feed, the increase in measured ΔP_{FC}, i.e., from 0.83 "H_2O before the surge to 4.25 "H_2O at the peak of surge, is used to estimate the magnitude of condensable flow surge. The non-condensable flow consists of calcine gases produced in the cold cap, whose main constituent is CO_2. Thus, the increase in measured CO_2 (MS) in the off-gas, i.e., from 0.62 to 2.1%, is used to estimate the magnitude of non-condensable flow surge. Both Figure 2-7 and Figure 2-8 show a second smaller peak ~7 min after the first and it is not counted as part of the large surge but as a separate surge. It is this second pressure spike that clearly shows the time delay in the response of CO_2 readings, which is estimated to be 18 seconds. The time delay in the response of T_{vs} readings is estimated to be much longer at 1 minute 49 seconds.

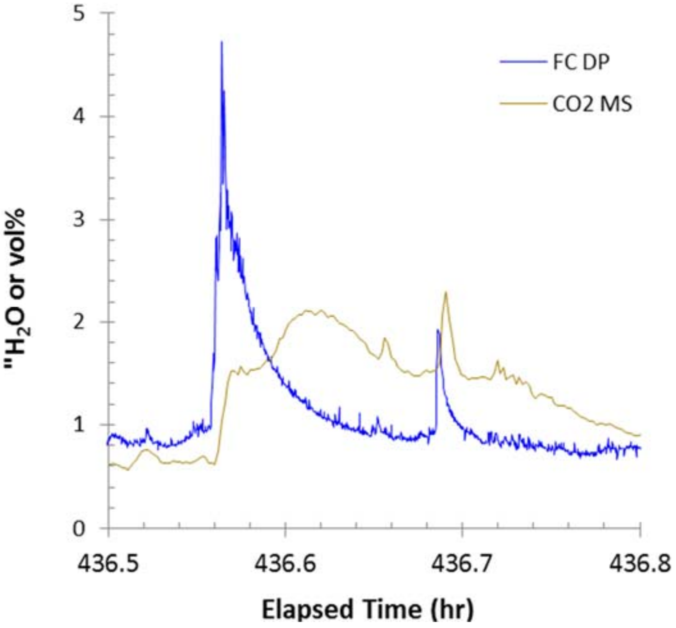

Figure 2-8. Profiles of ΔP_{FC} and CO_2 during 13 "H_2O Pressure Spike.

It is noted that the feed rates used in Phase 1 was ~50% higher than those used in Phase 2 partly because the CEF was run at a 50-100 °C higher T_{vs}. Nevertheless, the CEF was definitely pushed harder during Phase 1 in terms of feed rate because the ability to visually monitor the cold cap to prevent potential overfeeding was non-existent. It means that had the CEF been run the same way as it was during Phase 2, the pressure spikes measured in Phase 1 would have been smaller and less frequent, which in turn would have made the greater surging tendency of the NGA flowsheet feed more evident in terms of both magnitude and frequency. Increased surging tendency of the NGA flowsheet feed is likely due to excess nitrate which is the main gas generator in the cold cap.

3.0 DWPF Melter Off-Gas Chemistry Model

3.1 Original Model

The original DWPF melter off-gas flammability model had been in use since the radioactive startup in 1996 through the assessment of SB6 in 2010 to define the melter operating window for a given sludge batch in the form of Technical Safety Requirements (TSR) and feed interlocks.[14] It consists of two sub-models; the first model, called the 4-stage cold cap model, thermodynamically describes the chemistry of calcination and fusion reactions and calculates the compositions of calcine gases and glass from a given feed composition. The model was developed based on the Scale Glass Melter 9th campaign (SGM-9) data and validated against data from two smaller-scale melters.[23] The calculated composition of calcine gases is then used as the input to the second model, called the melter off-gas (MOG) dynamics model, which predicts the transient behavior of the DWPF MOG system under various upset scenarios.[24] Embedded in the MOG dynamics model is the vapor space combustion module that calculates the time-dependent concentrations of flammable gases in the melter exhaust using the global kinetics scheme to predict the off-gas flammability potential downstream. The baseline upset scenario for the flammability safety analysis is an off-gas surge, which depends on the feed chemistry as well as the melter operating mode.[6]

3.2 Revised Model

It is noted that the original model was developed and validated using the data produced with the NFA flowsheet feeds that contained much smaller quantities of antifoam than used in the DWPF along with little free formic acid. The scope of the original model was expanded in 2011 by accounting for the presence of significant levels of antifoam and free (undissociated) formic acid in the feed and their impact on the off-gas flammability. Specifically, a 2-step antifoam decomposition scheme was added to the cold cap model,[19] while formic acid was allowed to volatilize and decompose via two parallel routes in the melter vapor space.[25] The resulting model bounded both H_2 and CO data taken during Phase 1.[8] In doing so, however, it over-predicted the TOC-to-H_2 conversion by a factor of ~4 at $T_{gas} < \sim 350$ °C, which was attributed to the conservative antifoam decomposition scheme used in the cold cap model.

The revised model had been used to perform the melter off-gas flammability assessment for SB6, SB7a, SB7b, SB8 and lastly SB9 in 2016. The DWPF has since implemented a new control strategy in 2017 and no longer requires the revised model to set the Technical Safety Requirements (TSR) and melter feed interlocks. Thus, the new model documented in this report may be viewed as a tool for assessing the impact of changing process and input conditions on the underlying chemistry of the cold cap/REDOX reactions and the combustion of flammable gases produced during the calincation/fusion process. As such, the model is called the DWPF melter off-gas chemistry model from here on.

3.3 New Model

The flowsheet change to be addressed in the new model is in the chemistry of cold cap and vapor space reactions involving the glycolate, free glycolic acid, and their decomposition products. Specifically, the strategy used to develop a new off-gas flammability model for the NGA flowsheet was to preserve the original 4-stage cold cap model construct, and the impact of the new flowsheet chemistry was instead modeled by introducing a new reaction zone located at the cold cap surface where the volatile feed components and those with low decomposition temperatures participate in the pre- and post-cold cap reactions before entering the vapor space reactor, and further address the shortcomings of the current model, including the conservative antifoam decomposition scheme.

Regarding the conservatism in the antifoam decomposition scheme used in the current model, the results of Phase 2 as well as crucible tests using feeds spiked with excess antifoam showed little or no difference in terms of H_2 evolution between the baseline and spiked feeds. This is likely because the excess nitrate in the NGA flowsheet feed was more than enough to counterbalance the excess antifoam carbon added, resulting in little or no net increase in the reducing potential of the feed.

3.3.1 *Fractional Removal of Nitrate*

The scoping cold cap model runs showed that under the thermodynamic equilibrium framework practically 100% of the nitrate fed would reduce to N_2 in the cold cap and the O_2 thus formed would oxidize most of the H_2 and CO produced from the decomposition of carbon species, rendering the resulting calcine gases non-flammable, despite their presence in the off-gas at low but non-zero concentrations.[4] Low concentrations of H_2 and CO were detected in the off-gas during Phase 2 (see Table 2-11) and during the crucible test, as shown in Figure 2-2 in comparison to the NFA flowsheet feeds. In Revision 0, a new parameter was introduced in the form of fractional nitrate removal by excluding a portion of nitrate fed from the cold cap model input, effectively reducing the oxidizing potential of the feed. Specifically, it is N_2O_5 that gets removed from the input due to its volatility:

$$2\,NaNO_3 \;\rightarrow\; Na_2O + \;N_2O_5 \tag{3}$$

The gaseous product N_2O_5 is made up of NO_2 and NO_3, and the latter further decomposes to NO and O_2. The physical justification for this parameter was that since nitrate is present at such a high concentration in the feed, it is conceivable that some fraction of it decomposes and leaves the cold cap without fully imparting its oxidizing power on other feed constituents. This scheme is similar to the bypassing mechanism frequently used to model the non-ideal mixing in real processes. The fraction of nitrate to be removed was determined iteratively by matching as closely as possible the calculated concentrations of H_2 and CO at an assumed removal fraction with those measured at the lowest vapor space temperatures at near 300 °C or lower during each series of steady state runs.[4]

3.3.2 *Glycolic-Acid Denitration*

The fractional removal of nitrate thus determined in Revision 0 for the 100% acid stoichiometry feed was 22%, and this nitrate removal was equivalent to 90% denitration in the glycolic acid-to-nitrate molar ratio of 1:2 as follows:[4]

- The cold cap model input vector for the 100% acid-stoichiometry feed in Table 4-1 of Reference 4 shows the following flows; $C_2H_4O_3$ = 30.847 moles/hr and N_2O_5 = 27.505 moles/hr. The corresponding flow of nitrate is (27.505) (2) = 55.01 moles/hr, which is numerically close to (30.847) (2) (0.9) = 55.52.

A literature review found an earlier work that produced the data of relevance to this study. The data came from the bench-scale experiments conducted at the Pacific Northwest National Laboratory

(PNNL) to evaluate the effectiveness of sucrose and glycolic acid as a reductant for the denitration of high-nitrate salts.[26] The feed used was the simulated Low Activity Waste (LAW) evaporator bottoms, whose composition is shown in Table 3-1; although sodium was by far the most dominant cation species, it also contained several other metal species found in the DWPF feed, and the nitrate concentration was quite high as it accounted for ~74 wt% of the dried solids compared to 12.4 wt% for the 100% acid-stoichiometry feed. The partially-dried LAW bottoms simulant was blended with a synthetic calcium silicate inert, called Micro-Cel E, and glycolic acid was added at the glycolic acid-to-nitrate molar ratio of 1:1.4. The mixture was fed to a rotary calciner and heated to 375 °C at 5-20 °C/min under argon purge. The analysis of the calcination product showed that 90.6% of nitrate was removed at the end of heating and, as expected, the removal efficiency was shown to depend strongly on how well various feed components were mixed.

Table 3-1. LAW Evaporator Bottoms Simulant Used in the PNNL Study [Ref. 26].

Analyte	mole/L	g/L
Al	6.60E-01	1.78E+01
B	1.87E-02	2.02E-01
Ca	2.36E-01	9.46E+00
Cd	2.82E-03	3.17E-01
Cr	2.88E-03	1.50E-01
Fe	2.14E-02	1.20E+00
K	1.77E-01	6.92E+00
Mn	1.16E-02	6.37E-01
Na	1.79E+00	4.12E+01
Ni	1.13E-02	6.63E-01
Zr	1.68E-03	1.53E-01
Ag	7.19E-06	0.00E+00
NO_3	4.55E+00	2.82E+02
PO_4	1.35E-02	1.28E+00
SO_4	4.62E-02	4.44E+00
Cl	3.14E-02	1.11E+00
F	6.86E-01	1.30E+01
Total		3.81E+02

As glycolic acid is added to the SRAT batch as a 70% solution early in the DWPF process, the nitrate and glycolic acid (dissociated and undissociated) should remain well-mixed throughout the SRAT/SME processing and the evaporation/calcination steps in the melter cold cap. Furthermore, as the melter feed is calcined to a much higher temperature than 375 °C, it seems reasonable to postulate that the denitration efficiency in the melter would be higher than 90% at the same glycolic acid-to-nitrate ratio of 1:1.4, which is equivalent to saying that the same 90% denitration efficiency would be achieved at a lower glycolic acid-to-nitrate ratio than 1:1.4.

Thus, the fractional removal of nitrate is superseded by the glycolic-acid denitration in Revision 1 and the extent of reaction is set at 90% denitration at the stoichiometric glycolic acid-to-nitrate ratio of 1:2. As this substitution eliminated the need for iteratively solving for the fractional removal of nitrate, it became more important to accurately determine the fraction of free glycolic acid in the total glycolic measured by IC, as shown by Figure 2-1. Furthermore, the glycolic-acid denitration is modeled as one of the pre-cold cap reactions taking place in the new reaction zone located at the surface of the cold cap and proceeds as follows:

$$N_2O_5 \rightarrow 2NO + \frac{3}{2}O_2 \tag{4}$$

$$C_2H_4O_3 + \frac{3}{2}O_2 = 2\,CO_2 + 2H_2O \tag{5}$$

In this study, the formation of N_2O was modeled as the byproduct of the glycolic-acid denitration reactions:

$$N_2O_5 + 2\,NO \rightarrow 2\,N_2O + \frac{5}{2}O_2 \tag{6}$$

The formation of N_2O was modeled using Eq. (6), as it is regarded as the most probable route.[27] The extent (or fractional conversion) of Eq. (6), ξ_6, was set by matching the measured concentration of N_2O in the off-gas at each T_{gas}, while the extent of Eq. (4), ξ_4, was set at 1- ξ_6. In doing so, 100% of N_2O_5 is consumed by Eq. (4) and Eq. (6). In case not enough N_2O was produced via Eq. (6), additional N_2O could be produced via the disproportionation of NO:

$$3\,NO \rightarrow N_2O + NO_2 \tag{7}$$

It turned out that Eq. (7) was not necessary in any of the cases considered. The extent of Eq. (5) depends on the availability of O_2 produced from Eq. (4) and, if available, from the decomposition of the remaining nitrate (after de-nitration) in the cold cap.

3.3.3 *Thermal Decomposition of Free Glycolic Acid*

The remaining free glycolic acid after Eq. (5) was thermally decomposed as follows:

$$C_2H_4O_3 \rightarrow 2CO + H_2 + H_2O \tag{8}$$

Eq. (8) was modeled as part of the pre-cold cap reactions, as free glycolic acid would begin to decompose quickly upon entering the melter and exit the cold cap along with other volatile components in the feed. The extent of Eq. (8) was determined iteratively at each steady state $T_{gas} \leq$ 350 °C of the baseline case by varying the rate of air infiltration simultaneously until 125% of the measured concentrations of H_2 and CO are matched using the existing global kinetic parameters of H_2 and CO combustion shown in Table 3-2. Using the existing global kinetic parameters at $T_{gas} \leq$ 350 °C was conservative, as they were shown in Revision 0 to under-predict the rate constants that were derived to match 125% of measured H_2 data, as shown in Figure 4-1. The extents of Eq. (8) thus determined at $T_{gas} \leq 350$ °C were used to derive the first-order global kinetic parameters of the glycolic-acid decomposition, which were then used to predict the extents of Eq. (8) at $T_{gas} > 350$ °C. Note that the intent of targeting 125% of measured H_2 and CO data was to impart conservatism by slowing down the combustion kinetics.

Table 3-2. Existing First-Order Global Kinetic Parameters of Vapor Space Combustion.[21]

Species	k_o (1/sec)	E_a (Btu/lbmole)	R^2
CO	1,759	22,192	0.845
H_2	2.795 E7	38,940	0.999

3.3.4 *Reduction of NO to N_2*

Under the thermodynamic-equilibrium framework, the cold cap model predicts that practically 100% of the nitrate fed would decompose into N_2, as pure $NaNO_3$ would under inert conditions.[28] However, the conditions in the cold cap are far from being inert particularly under the constant air purge into the vapor space. This is reflected on the off-gas data collected during Phase 2; the most dominant nitrogen-oxygen species detected in the off-gas was NO. To overcome this difficulty, the model was run by removing N_2 and N_2O from the list of potential species that can form in the cold cap, which in turn made the resulting calcine gases very reducing, i.e., contain conservatively high concentrations of H_2 and CO. Thus, part of the NO formed was reduced to N_2 via:

$$2NO \rightarrow N_2 + O_2 \tag{9}$$

where the extent of Eq. (9) was set by matching the amount of N_2 produced from the nitrate in the feed, which was calculated as the balance of the total N fed as nitrate after subtracting the total N in the measured $NO/NO_2/N_2O$. The O_2 produced from Eq. (9) was allowed to participate in the post-cold cap reactions with H_2 and CO exiting the cold cap.

3.3.5 *Air Infiltration*

In some cases, the O_2 produced from Eq. (9) was determined to be not nearly enough to reduce the predicted H_2/CO concentrations by the cold cap model to 125% of their respective off-gas data after the vapor space combustion. The shortfall in O_2 was made up for by allowing air to infiltrate the new reaction zone at the cold cap surface and participate in the post-cold cap reactions with H_2/CO exiting the cold cap. In this study, the extent of air infiltration was calculated as a fraction of the SRNL and Canty camera air purges combined, which was maintained constant at ~8 scfm in all runs. Specifically, the extent of air infiltration was determined at each steady state $T_{gas} \leq 350$ °C of the baseline case by matching 125% of measured H_2 off-gas data using the existing global kinetic parameters of H_2 combustion. As Eq. (8) produces both H_2 and CO, the extents of Eq. (8) and air infiltration were determined iteratively by matching 125% of measured H_2 and CO simultaneously. Once the extent of air infiltration was determined for $T_{gas} \leq 350$ °C, the best-fit curve of data was derived and used to predict those of the baseline case at $T_{gas} > 350$ °C.

3.3.6 *New Global Kinetic Parameters of H_2/CO Combustion*

The extents of H_2 and CO oxidation were determined for $T_{gas} > 350$ °C by matching 125% of the measured concentrations of H_2 and CO using the extents of Eq. (8) and air infiltration predicted by their respective correlations that were derived from the data at $T_{gas} \leq 350$ °C. A new set of global kinetic parameters for H_2 and CO combustion were then derived from the existing extents of reaction at $T_{gas} \leq 350$ °C and those just derived at $T_{gas} > 350$ °C.

3.3.7 *Oxidation of NO to NO_2*

It was assumed that no NO_2 was present in the off-gas exiting the melter during Phase 2 and it only formed downstream of the film cooler via:

$$NO + \frac{1}{2}O_2 \rightarrow NO_2 \tag{10}$$

The extent of Eq. (10) was determined by matching the measured concentration of NO_2 in the off-gas assuming that the data was taken at the off-gas temperature measured at the FC exit, T_{FC_exit}. If there was a clear correlation between the extent of Eq. (10) and T_{FC_exit}, the extents of reaction determined at varying T_{FC_exit} were used to derive the global kinetic parameters of NO oxidation.

4.0 Mass and Energy Balance Calculations

Since only the steady state conditions were considered in this study, it was not necessary to run the entire MOG dynamics model. Instead, a spreadsheet was developed that calculates the steady state component mass and energy balances for the melter and off-gas system, including the global combustion kinetics of H_2 and CO in the melter vapor space (VS). Once the component flow rates of calcine gases calculated by the cold cap model were input into the spreadsheet along with the CEF operating parameters in Table 2-10, the unknowns such as the CEF air inleakage and T_{gas} as well as the nitrate decomposition model and other kinetic parameters were determined according to the calculation steps outlined next.

4.1 Calculation Steps

For all T_{gas} of each data set:

1. Calculate ΔP across the off-gas header, i.e., from the film cool exit to the quencher inlet using the hydraulic equations from the literature.
2. Estimate the quencher suction using the performance curve at a given draft, which was calculated as the ΔP between the quencher inlet and the off-gas condensate tank (OGCT).
3. Estimate the rate of air inleakage and the actual gas temperature in the CEF vapor space (T_{gas}) simultaneously by performing an overall mass/energy balance calculations from the melter to the FC exit.
4. Calculate the carbon balance as the difference between the calculated and measured flow rates of carbon due to CO and CO_2 combined at the FC exit.
5. Exclude from further considerations those cases whose carbon balance is off by > ±25%.
6. Adjust the extent of Eq. (9) until the calculated concentration of N_2 in the off-gas that originated from the nitrate fed, i.e., excluding the contributions from the air purges and inleakage, equals that calculated as the balance of total N fed as nitrate after subtracting the sum of N from the measured concentrations of NO, NO_2 and N_2O.
7. Adjust the extent of Eq. (6) until the calculated concentration of N_2O in the off-gas matches measured data.
8. Adjust the extent of Eq. (10) until the calculated concentration of NO_2 in the off-gas matches measured data.
9. Check the nitrogen balance by calculating the fraction of total N fed as nitrate that exited the melter as N_2 and that calculated as the balance of the total N fed after subtracting the sum of N from measured $NO/NO_2/N_2O$ data.
10. Exclude those cases with negative nitrogen balance (i.e., negative N_2 concentration) and/or with substantial differences between the calculated and measured concentrations of NO, from the development of the nitrate decomposition chemistry model.
11. Pick the baseline case for the model development from the four data sets; 100%_B, 100%_NB, 125%_B, and 125%_NB. The selected baseline case must have enough steady state data points remaining after the carbon/nitrogen balance screening.

For the baseline case:

12. Adjust the extent of air infiltration and that of Eq. (8) until the calculated concentrations of H_2 and CO using the existing global combustion kinetics parameters match 125% of their respective measured data simultaneously at each $T_{gas} < 350$ °C.
13. Derive a correlation:
    - between the extent of air infiltration and feed flux, defined as the feed rate per unit melt surface area
    - between the extent of Eq. (8) and feed flux.
14. Predict the extent of air infiltration and that of Eq. (8) at each $T_{gas} > 350$ °C using the correlations developed in Step 13.
15. Using the extents of air infiltration and Eq. (8) calculated in Step 14, determine the extents of H_2 and CO combustion in the vapor space at each $T_{gas} > 350$ °C by matching the calculated concentrations of H_2 and CO with 125% of their respective measured data.
16. Derive the revised 1^{st}-order global kinetic parameters of H_2 and CO combustion from the extents of H_2 and CO combustion determined in Step 15 for $T_{gas} > 350$ °C and those derived from the existing global kinetic parameters for $T_{gas} < 350$ °C.

For the remaining cases,

17. Calculate the extent of Eq. (8) using the correlation developed in Step 13 at each T_{gas}.
18. Adjust the extent of air infiltration until the calculated concentration of H_2 using the revised global combustion kinetics parameters developed in Step 16 matches 125% of the measured data at each T_{gas}.
19. Check if the calculated concentration of CO remains conservative.
20. Check if the calculated extents of air infiltration can be correlated to the feed flux.
21. Check if the total O_2 made available through Eq. (9) and air infiltration can be correlated to the feed flux for varying feed and operating conditions.

4.2 Cold Cap Model Run

4.2.1 *Model Input*

The 100% and 125% acid stoichiometry SRAT product compositions in Table 2-6 and Table 2-7, respectively, were remediated per Table 2-8 and the free acid fractions were adjusted according to Figure 2-1 at the measured pH of each remediated feed. The resulting Phase 2 feed compositions were then converted into the cold cap model input vectors in gmole/hr at the DWPF design basis glass production rate of 228 lb/hr, as shown in Table 4-1 and Table 4-2 for the 100% and 125% acid stoichiometry feeds, respectively. The decomposition scheme used to convert the insoluble solids and salts into oxides and gases is described elsewhere.[29] The flow rates of N_2O_5 shown represented 11% and 20% nitrate removal (i.e., denitration) for the 100% and 125% acid stoichiometry, respectively. Some of the trace level species such as Ba, Cr and Ti were left out of these input vectors; yet the input still accounted for over 99.6% of the dried feeds.

Table 4-1. Cold Cap Model Input at 228 lb/hr Glass Rate (100% Acid Stoichiometry).

Species	Stage 1 (gmole/hr)	Stage 2 (gmole/hr)	Stage 3 (gmole/hr)
Condensed:			
Al_2O_3	0	95.789	0
B_2O_3	75.922	0	0
CaO	0	10.678	0
CuO	0.751	0.000	0
Fe_2O_3	73.111	0	0
K_2O	1.530	0.007	0
Li_2O	0	176.889	0
MgO	0	0	13.441
MnO_2	0	5.687	0
MnO	41.930	0	0
Na_2O	112.498	92.595	0
NiO	19.271	0	0
SiO_2	859.043	0	0
$CaSO_4$	0	0	0
$Na2SO_4$	0	0	3.923
Calcine Gases:			
H_2O	533.781	6.600	2.640
CO	85.102	96.962	37.094
CO_2	24.332	35.516	12.365
H_2	73.325	92.735	37.094
O_2	26.520	61.827	24.731
NO	37.096	61.827	24.731
NO_2	37.096	61.827	24.731
Volatiles to Vapor Space:			
HCOOH	0.139		
$C_2H_4O_3$	15.330		
HNO_3	3.232		
CH_4	13.100		
N_2O_5	13.797		
H_2O (free)	8,978.516		

Table 4-2. Cold Cap Model Input at 228 lb/hr Glass Rate (125% Acid Stoichiometry).

Species	Stage 1 (gmole/hr)	Stage 2 (gmole/hr)	Stage 3 (gmole/hr)
Condensed:			
Al_2O_3	0	96.692	0
B_2O_3	75.817	0	0
CaO	0	11.505	0
CuO	0.691	0	0
Fe_2O_3	68.699	0	0
K_2O	1.408	0	0
Li_2O	0	176.646	0
MgO	0	0	12.924
MnO_2	0	8.049	0
MnO	38.372	0	0
Na_2O	110.738	91.962	0
NiO	18.525	0	0
SiO_2	858.680	0	0
$CaSO_4$	0	0	0
$Na2SO_4$	0	0	3.612
Calcine Gases:			
H_2O	519.225	15.329	6.132
CO	91.275	115.317	44.481
CO_2	18.282	30.962	10.739
H_2	70.944	95.874	38.350
O_2	27.312	62.182	24.873
NO	37.309	62.182	24.873
NO_2	37.309	62.182	24.873
Volatiles to Vapor Space:			
HCOOH	0.664		
$C_2H_4O_3$	37.047		
HNO_3	0		
CH_4	12.382		
N_2O_5	33.342		
H_2O (free)	8,832.470		

4.2.2 *Model Output*

The flow rates of glass and calcine gases calculated by the cold cap model are shown in Table 4-3 for both 100% and 125% acid stoichiometry feeds. The predicted glass compositions are split in groups or phases; the letter l after each species in the melt phase denotes "liquid." These liquid (or melt) species do not necessarily represent independent molecular or ionic species but serve to represent the local associative order.[30] Due to structural similarities, spinels readily form solid solutions with one another and thus are allowed to form a separate phase of their own. Each of the species in the Invariant Condensed Phase (ICP) is assumed to form a separate phase by itself. The calculated REDOX of the two Phase 2 feeds was similar at 0.11-0.12, which lie between the measured value of 0.26 in a CC-ramp and those of the glass samples pulled from the CEF which were fully oxidized.

Table 4-3. 4-Stage Cold Cap Model Output at 228 lb/hr Glass Rate.

Species	100% Acid (gmole/hr)	125% Acid (gmole/hr)
Melts:		
SiO_2 l	633.512	636.234
Na_2SiO_3 l	209.023	206.262
$LiBO_2$ l	151.154	150.926
$LiAlO_2$ l	191.600	193.400
Fe_3O_4 l	12.859	12.861
$MgSiO_3$ l	13.057	12.492
FeO l	2.769	2.769
$CaFe_2O_4$ l	3.041	3.328
B_2O_3 l	4.8E-04	0.001
Ca_2SiO_4 l	1.645	1.977
$Ca_3MgSi_2O_8$ l	0.221	0.278
Fe_2SiO_4 l	0.106	0.107
Li_2O l	5.523	4.437
K_2SiO_3 l	1.214	1.072
KBO_2 l	0.644	0.673
Spinels:		
$NiFe_2O_4$	19.270	18.530
Mn_3O_4	15.872	15.473
$CuFe_2O_4$	0.751	0.691
$MgFe_2O_4$	0.162	0.149
Invariant Condensed Phase:		
Fe_2O_3	29.097	25.219
$CaSO_4$	3.684	3.394
Calcine Gases:		
H_2O	671.866	651.643
CO_2	278.526	290.462
H_2	100.715	119.030
CO	25.933	32.954
SO_2	0.239	0.218
NO	247.350	248.770
NO_2	8.8E-09	7.3E-09
$H_2/(CO_2+CO)$	0.331	0.368
CO/CO_2	0.093	0.113
REDOX:		
Fe^{+2}/Fe^{total}	0.11	0.12
Measured (closed crucible-ramp)	0.26	0.26

4.3 Mass and Energy Balance Calculations

A spreadsheet was used to perform the component mass and energy balance calculations from the CEF vapor space to the OGCT for each of the 24 steady state data sets. This section describes the input and output of the spreadsheet along with further interpretation of data in light of the results. The main goal of Revision 1 was to develop the nitrate decomposition model based on measured $NO/NO_2/N_2O$ data, determine the extents of air infiltration and thermal decomposition of $C_2H_4O_3$, and refine the existing global kinetic parameters for H_2 and CO combustion at $T_{gas} > 350$ °C.

4.3.1 *Spreadsheet Input*

The input for the spreadsheet calculations included all the steady state pressure, temperature, and flow data taken during Phase 2, as shown in Table 2-10 and tabulated in more detail in Appendix A, as well as the instantaneous flow rates of calcine gases calculated by the cold cap model (Table 4-3) and the volatile feed components fed directly to the vapor space (Table 4-1 and Table 4-2). To simulate actual steady state operations reflected in Table 2-10, the flow rates of calcine gases and volatiles were adjusted down by the Phase 2-to-DWPF feed rate ratio.

4.3.2 *Bases and Assumptions*

Except for CH_4 which was detected mostly at <10 ppm, the only flammable gases detected during Phase 2 were H_2 and CO so the off-gas flammability assessment was focused on these gases only. Before performing such assessments, however, two unknowns that cannot be measured directly and yet have a large impact on the measured concentrations of H_2 and CO must be estimated from the data collected. The first unknown is the rate of air inleakage into the CEF vapor space which, depending on the CEF vacuum, can constitute a major portion of the total air available for both combustion and dilution. The second is the actual gas temperature in the CEF vapor space (T_{gas}) at each measured vapor space temperature (T_{vs}), and it is T_{gas} that is used in the combustion kinetics calculations. Since gases are mostly transparent to infrared radiation, T_{gas} tends to be lower than T_{vs}, and the size of difference between the two temperature readings depends on both design and operating variables such as configuration of melter cavity and feed rate. Furthermore, these two unknowns are interdependent so they need to be solved simultaneously by iteration. Three key assumptions were made to facilitate the evaluation of these unknowns and further develop the nitrate decomposition chemistry.

4.3.2.1 Well-Mixed Reactor

The CEF vapor space is assumed to be a well-mixed reactor. This assumption is valid since the CEF has 3 fixed air injection points plus a substantial rate of air inleakage. Likewise, the DWPF melter maintains a dedicated air purge through the backup film cooler which was shown to form an air jet extending down to the cold cap, providing good mixing by entrainment.[5] This assumption enables the use of T_{gas} as the representative gas temperature for the entire vapor space.

4.3.2.2 First-Order Global Kinetics

The combustion of H_2 and CO in the vapor space is currently modeled using the first-order global kinetics approach:[23]

$$-r = k_o \exp(-E_a/RT)C \qquad (11)$$

where $-r$ is the reaction rate in lbmole/ft^3/sec, k_o the pre-exponential factor in 1/sec, E_a the activation energy in Btu/lbmole, R the gas constant, T the gas temperature in K, and C the concentration of H_2 or CO in lbmole/ft^3. The global first-order kinetic parameters of H_2 and CO oxidation used by the existing model are shown in Table 3-2; they were derived from the data taken during the Scale Glass Melter 9th Run (SGM-9) and have been in use beginning with the original model. It is the intent of this work to revise the kinetic parameters for both H_2 and CO combustion, as they were shown to be not conservative at all T_{gas}.[4] For example, the existing first-order rate constants for H_2 combustion are shown in Figure 4-1 to be higher than those calculated from the Phase 2 data at T_{gas} > ~350 °C, which means that the predicted concentration of H_2 would be lower than those measured and thus not conservative. At T_{gas} < ~350 °C, the existing first-order rate constants are lower than those calculated and thus conservative. It is noted that the lower temperature bound for the existing kinetic parameters was originally T_{gas} = 393 ºC and later extended down to 204 ºC.[23]

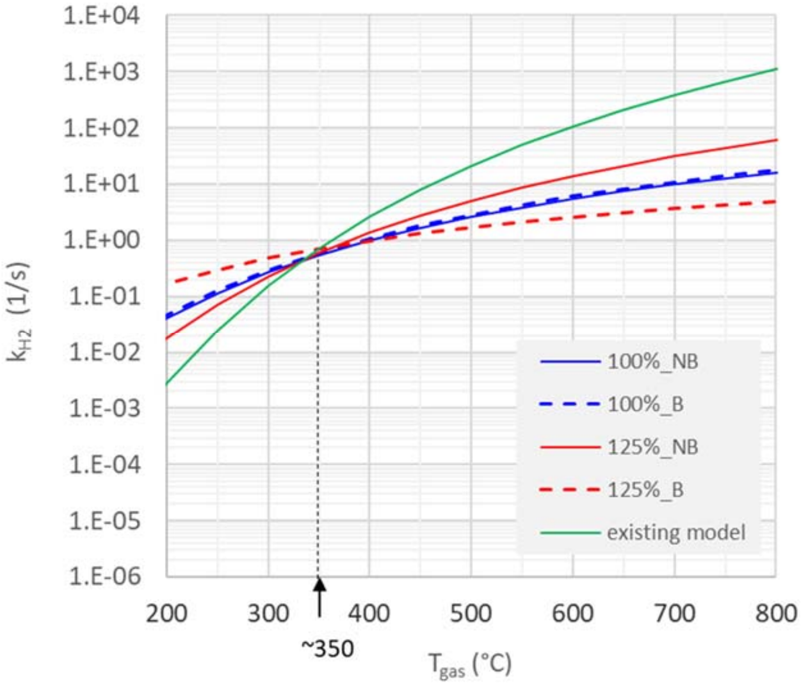

Figure 4-1. Comparison of First-Order Rate Constants of H_2 Combustion from Existing Model and Revision 0 [Ref. 4].

4.3.2.3 Air Infiltration

This is a new feature added to Revision 1. Preliminary nitrogen balance showed that the total N in the measured $NO/NO_2/N_2O$ during Phase 2 would not allow enough N_2 (and O_2) to form from Eq. (9) and, as a result, the H_2 produced in the cold cap and from Eq. (8) would not burn sufficiently to the level of ≤100 ppm in the off-gas after combustion in the vapor space per the existing global kinetics. Thus, the air from the vapor space was taken as an additional source for O_2. Although the cold cap itself is modeled as an impermeable entity, its surface is in constant contact with the air above so it seems logical to allow air to infiltrate the new reaction zone at the cold cap surface and participate in the low-temperature reactions that are excluded from the cold cap model such as the thermal decomposition of glycolic acid, glycolic-acid denitration, and oxidation of H_2/CO exiting the cold cap. Strictly speaking, the term "infiltration" here is not referring to air diffusing into the cold cap, whose boundary is defined in the model,[29] but rather the volatile feed components and calcine gases reacting with air on the cold cap surface before entering the vapor space reactor.

Air infiltration is not unique to the NGA flowsheet feed. In fact, it is also present with the NFA flowsheet feed as it is inherently related to the melter design and slurry feeding. The difference is that less N fed as nitrate is tied up in the measured concentrations of $NO/NO_2/N_2O$ with the NFA flowsheet feed, which means that Eq. (9) alone would produce enough O_2 (and N_2) so there is no need for additional O_2 from air infiltration. In this study, the sum of Canty and SRNL camera air purges in Table 2-10 was taken as the basis for air infiltration, as it was held constant at ~8 scfm throughout the Phase 2 test.

4.3.3 *Spreadsheet Calculations*

The air inleakage and true gas temperature in the CEF vapor space were calculated iteratively by matching; (1) calculated off-gas flow at the film cooler exit with the quencher suction and (2) calculated off-gas temperature at the film cooler exit (T_{FC_exit}) with the measured data. Specifically, the calculations proceeded in the following order:

1) *Off-Gas Header ΔP* - To calculate the quencher suction, the ΔP across the off-gas header between the quencher inlet and where the film cooler exit pressure is measured was first calculated using:[31]

$$\Delta P \;= 0.000000280\, K\, W\text{^}2/(D\text{^}4\,\rho)(27.7073) \qquad (12)$$

where ΔP is in "H_2O, W the off-gas flow rate in lb/hr, D the inside diameter of the off-gas header in ft, ρ the off-gas density in lb/ft^3, and K the resistance coefficient calculated as:

$$K = (12\, n_{90} + 50\, n_{RB} + L/D)f_T + 0.5804 \qquad (13)$$

where n_{90} is the number of 90° elbows, n_{RB} the number of return bends, L the total length of straight pipe in ft, and f_T the friction factor for turbulent pipe flow. The nominal 2" off-gas header has no 90° elbow, one return bend, and one 45° bend with expansion. The extent of iterative calculations involved can be seen from Eq. (12), which shows that the off-gas header ΔP depends on not only the off-gas flow rate (W), which includes one of the unknowns, air inleakage, but the density (ρ), which depends on the off-gas composition and temperature. The off-gas temperature in turn depends directly on the temperature of the off-gas exiting the melter, which is the other unknown, T_{gas}.

2) *Quencher Suction* - Once the off-gas header ΔP was calculated, it was subtracted from the measured film cooler exit pressure to calculate the quencher inlet pressure. Finally, the quencher draft was calculated by subtracting the quencher inlet pressure from the measured OGCT pressure. The quencher draft was then used to determine the suction from the vendor-provided performance curve for the 3" scrubber model FIG. 7007 by Schutte & Keorting.[32] Since the suction capacity estimated from the performance curve is for air at 20°C, the actual suction was calculated by taking into account the density difference between air and the CEF off-gas at T_{FC_exit}:

$$Q = \; Q_{air}\sqrt{\rho_{air}/\rho} \qquad (14)$$

where Q is the suction capacity in acfm, and ρ the density in lb/ft^3.

3) *Estimation of Unknowns* - The CEF air inleakage rate was varied along with the true vapor space gas temperature, until the calculated off-gas flow and temperature at the film cooler exit matched Q and T_{FC_exit} simultaneously. It is noted that after each iteration cycle the vapor space combustion kinetic parameters and all other relevant component and stream properties such as heat capacities were updated before the next iteration cycle.

4) *Estimation of Air Infiltration* – For the baseline case at $T_{gas} < 350$ °C, the fraction of camera air that infiltrated the cold cap was varied until enough O_2 was made available to reduce the concentration of H_2 produced from the cold cap and from Eq. (8) to 125% of the measured data in the off-gas after combustion in the vapor space per the existing global kinetics. At $T_{gas} > 350$ °C, the fraction of camera air was estimated by extrapolating the air infiltration vs. feed flux data taken at $T_{gas} < 350$ °C.

5) *Thermal Decomposition of Glycolic Acid* – For the baseline case, the fractional conversion of Eq. (8) was varied at each $T_{gas} < 350$ °C until the calculated concentrations of H_2 and CO in the off-gas using the existing global combustion kinetics matched 125% of their respective measured data. For $T_{gas} > 350$ °C, the fractional conversion of Eq. (8) was estimated by extrapolating the fractional conversion vs. T_{gas} data taken at $T_{gas} < 350$ °C.

6) *Revised Kinetic Parameters of H_2 and CO Combustion* – The fractional conversions of H_2 and CO combustion calculated at $T_{gas} > 350$ °C and those based on the existing kinetic parameters at $T_{gas} < 350$ °C were fitted together into new 1st order global kinetic models and the new kinetic parameters for H_2 and CO combustion, respectively, were derived.

4.3.4 *Spreadsheet Output*

The results of mass and energy balance calculations for the 26 steady state runs are given in Table 4-4 in a chronological order. Some of the key results are discussed next.

4.3.4.1 Overall Carbon Balance

The carbon balance results shown in Table 4-4 was calculated as:

$$C\ Balance\ = \frac{(Total\ C\ in\ calculated\ CO_2{+}CO - Total\ C\ in\ measured\ CO_2{+}CO)}{Total\ C\ in\ measured\ CO_2{+}CO} \times 100 \qquad (15)$$

So, a negative carbon balance would mean that the total carbon in the calculated CO_2/CO flows was smaller than that in the measured CO_2/CO flows. The fact that carbon balance was negative for all 26 cases is consistent with the results shown in Table 2-9; the calculated TOC of the remediated feeds was up to 18% lower than the TOC_{DWPF} data. Although carbon balance is also affected by the quality of steady state data, a likely culprit of negative carbon balance consistently shown in Table 4-4 is under-estimation of total glycolate in each feed by the sample preparation and analytical methods employed, as the antifoam carbon was set at the theoretical maximum according to the recipe assuming 100% retention during the SRAT/SME processing.

Carbon balance was off by more than 25% in 5 of 26 steady state runs, and they were excluded from further considerations. In addition, the 100%_B case at $T_{vs} = 607$ °C was also excluded for two reasons. First, it was so close to the adjacent steady state run at $T_{vs} = 592$ °C that the calculated T_{gas} differed by < 2 °C. Second, the measured NO_x data by FTIR or MS was considerably lower than the trend predicted by the adjacent data points, as shown in Table 2-11.

4.3.4.2 Nitrogen Balance

A total of 8 steady state cases showed poor nitrogen balance in terms of negative N_2, mostly during the 125%_NB run. However, half of the 8 cases had no further impact on the results, as they also showed poor carbon balance and were already excluded. Poor nitrogen balance impacts the nitrogen chemistry model to be developed but not the overall mass and energy balance. Thus, those cases with poor nitrogen balance were included in the calculation of operating parameters such as air inleakage and T_{gas}. The nitrogen balance is discussed in more detail later in this report.

Table 4-4. Output of CEF Phase 2 Steady State Heat/Mass Balance Calculations.

SS Run	T_{vs} (°C)	Feed Flux (lb/hr/ft$_2$)	T_{gas} (°C)	Melter P (“H_2O)	Air Inleakage (lb/hr)	Extent of Eq. (9)	Air Infiltration (% Camera Air)	Total O_2 Flux (lb/hr/ft$_2$)	Carbon Balance	N_2 from Feed (mole/mole NO_3)	NO_2/NO (FTIR)
125%_B	705	13.1	552	-5.22	40	30.3%	0.22%	0.098	-18.9%	0.224	0.220
	625	9.5	460	-5.35	46	18.7%	0.41%	0.066	-21.6%	0.131	0.192
	481	6.7	348	-4.90	49	30.5%	0.26%	0.051	-7.4%	0.226	0.148
	415	6.6	307	-4.74	46	28.5%	0.28%	0.049	3.8%	0.210	0.161
	360	5.5	275	-3.48	30	42.1%	-0.01%	0.042	9.2%	0.319	0.165
	270	4.3	220	-1.16	16	26.2%	0.18%	0.032	-3.6%	0.191	0.141
125%_NB	709	5.9	513	-5.47	49	4.8%	0.62%	0.049	-19.8%	0.019	0.155
	604	6.3	401	-5.29	86	0.0%	0.59%	0.050	-31.7%	-0.170	0.202
	486	5.2	306	-5.51	98	0.0%	0.28%	0.035	-42.5%	-0.327	0.182
	393	3.0	284	-5.46	66	0.0%	0.29%	0.022	-23.2%	-0.112	0.223
	351	2.6	262	-5.04	62	0.0%	0.27%	0.019	-21.1%	-0.130	0.376
	302	2.1	233	-4.96	53	0.0%	0.27%	0.016	-16.0%	-0.258	0.299
100%_B	750	11.5	557	-4.67	50	23.1%	0.65%	0.079	-20.2%	0.204	0.186
	705	10.1	529	-4.81	54	6.7%	0.86%	0.064	-28.5%	0.057	0.197
	607	9.9	426	-4.96	63	30.6%	0.19%	0.062	-11.1%	0.270	0.166
	592	8.6	424	-4.66	58	8.0%	0.75%	0.055	-21.4%	0.070	0.191
	521	7.5	336	-4.70	73	0.0%	0.87%	0.049	-32.2%	-0.050	0.207
	471	7.2	326	-4.42	68	0.0%	0.84%	0.046	-26.5%	-0.026	0.202
	373	6.0	276	-5.06	65	10.5%	0.56%	0.039	-13.4%	0.091	0.181
	323	5.2	243	-1.13	27	16.1%	0.40%	0.034	-5.5%	0.142	0.179
100%_NB	697	7.4	507	-5.27	51	13.6%	0.55%	0.049	-23.7%	0.120	0.181
	600	5.8	425	-5.70	55	9.9%	0.49%	0.039	-19.7%	0.086	0.170
	496	5.0	337	-6.00	61	5.4%	0.44%	0.030	-17.4%	0.046	0.166
	410	3.3	291	-5.46	63	1.6%	0.38%	0.021	-13.0%	0.012	0.168
	344	2.8	257	-4.46	57	4.2%	0.32%	0.018	-7.2%	0.036	0.288
	326	2.5	250	-4.02	50	0.0%	0.30%	0.016	-12.1%	-0.133	0.459

4.3.4.3 CEF Air Inleakage

The calculated air inleakage rates are plotted in Figure 4-2 against the square root of driving force, i.e., the differential pressure (ΔP) between the melter vapor space and ambient air. Despite some scatter, the calculated air inleakage rates increased linearly with increasing $\sqrt{\Delta P}$, as expected by Darcy's formula.[30] Air inleakage rate is also shown to increase with time from the 125% to 100% acid stoichiometry feed. For example, the calculated air inleakage rate during the 100%_B run at T_{VS} = 323 °C was ~70% higher than that during the 125%_B run four days earlier at T_{VS} = 270 °C, although the CEF pressure remained the same at -1.1 "H_2O, which suggests that the system became less tight as Phase 2 progressed. This is consistent with the observed deterioration of the insulation material with time particularly at the entry points of the lid heaters. In fact, two of the six 125%_NB runs were repeated toward the end of Phase 2 but the resulting data had to be discarded since the calculated air inleakage rates were nearly doubled at over 100 lb/hr, which made it difficult to mesh the new data into that obtained earlier. In Figure 4-2, the calculated air inleakage rates are fitted with a linear function of $\sqrt{\Delta P}$ for bubbled runs only, as the range of ΔP was wider; the fit (R^2) of non-bubbled runs was poor, as the range of ΔP variation was too narrow.

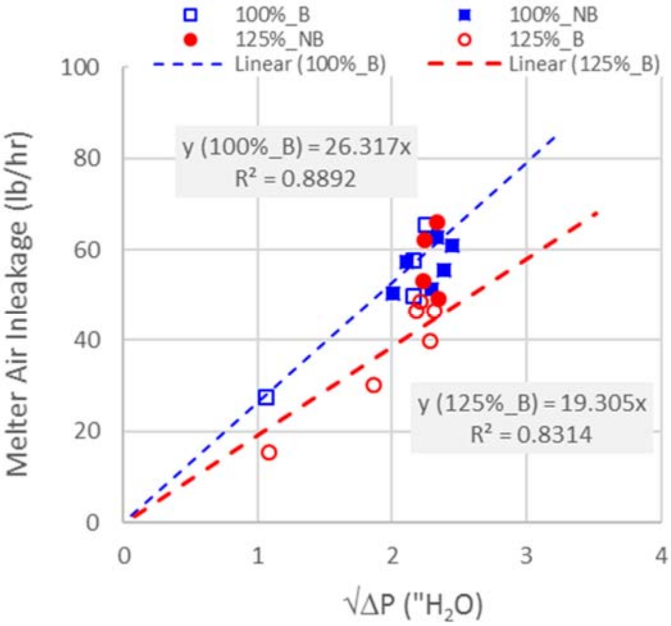

Figure 4-2. Calculated Air Inleakage during Phase 2 CEF Run.

The calculated air inleakage rates during Phase 2 are compared in Figure 4-3 to those from the earlier CEF runs. The high air inleakage rates at low T_{vs} during Phase 1 were attributed to the increased air infiltration through the pour tube due to highly intermittent glass pouring during low T_{vs} runs, which resulted in a relatively flat correlation between air inleakage rate and $\sqrt{\Delta P}$.[8] The same situation was also encountered during the Phase 2 non-bubbled runs at low T_{vs}; however, the calculated air inleakage rates were less scattered. It is clearly seen that efforts made to reduce the high air inleakage rate during the 2010 run appear to have worked;[6] however, the calculated air inleakage rates greater than 40-50 lb/hr at nominal -5" H_2O is still large considering that the calculated air inleakage rate of the DWPF melter, which has an effective melt surface area 11X larger than the CEF, has been < 100 lb/hr. This is one of the areas that need be improved upon to make the scale up of the CEF data more straightforward, if the same platform is to be used again in future melter tests.

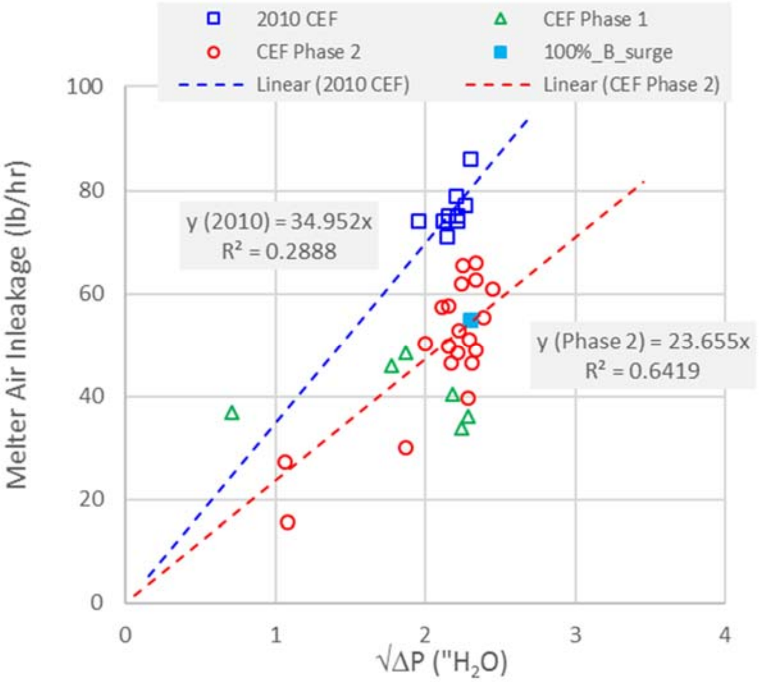

Figure 4-3. Comparison of Air Inleakage Rates During All CEF Runs.

4.3.4.4 Vapor Space Gas Temperature.

The calculated gas temperatures in the CEF vapor space (T_{gas}) are plotted in Figure 4-4 against the measured temperature (T_{vs}) during Phase 2. The existing DWPF correlation, Eq. (16), which has been used to define the DWPF melter operating window,[12] is shown to predict T_{gas} well for $T_{vs} >$ 500 °C. However, at $T_{vs} <$ 500 °C, it under-predicts T_{gas} and the extent of under-prediction is shown to increase as T_{vs} decreases below 500 °C. This was expected, as T_{vs} is higher than T_{gas} due to infrared radiation incident on the thermocouple, while gases are mostly transparent to such radiation, and the impact of infrared radiation decreases rapidly with decreasing T_{vs}. For example, at T_{vs} = 697 °C, the calculated T_{gas} was 507 °C, which agrees well with that calculated from the current DWPF correlation shown in Eq. (10). However, at T_{vs} = 326 °C, the calculated T_{gas} was 250 °C vs. 170 °C calculated from Eq. (16), which means that the combustion rate based on Eq. (16) would be lower by a factor of 5 than using the calculated T_{gas}. Considering that most safety basis calculations were performed in the past at $T_{gas} <$ 400 °C, this represents a significant source of conservatism in the current DWPF control strategy to mitigate potential off-gas flammability.[14]

$$T_{gas} = 0.91685\, T_{vs} - 128 \qquad (16)$$

Furthermore, all calculated T_{gas} during Phase 2 is shown to be fitted well by the correlation for the 100%_NB run, Eq. (17):

$$T_{gas} = 132.34\, e^{0.0019\, T_{vs}} \qquad (17)$$

At $T_{vs} >$ ~600 °C, Eq. (17) practically coincides with Eq. (16), and the validity of Eq. (16) was confirmed against the data taken from large-scale melters.[23] On the other hand, when Eq. (17) is extrapolated down to T_{vs} = 200 °C, it predicts T_{gas} = 194 °C, which shows that the impact of infrared radiation becomes negligible at near 200 °C, as postulated earlier.[23] It is noted that the validity of Eq. (17) throughout all T_{vs} range adds relevance to the calculated air inleakage rates shown in Figure 4-2, as they were determined simultaneously.

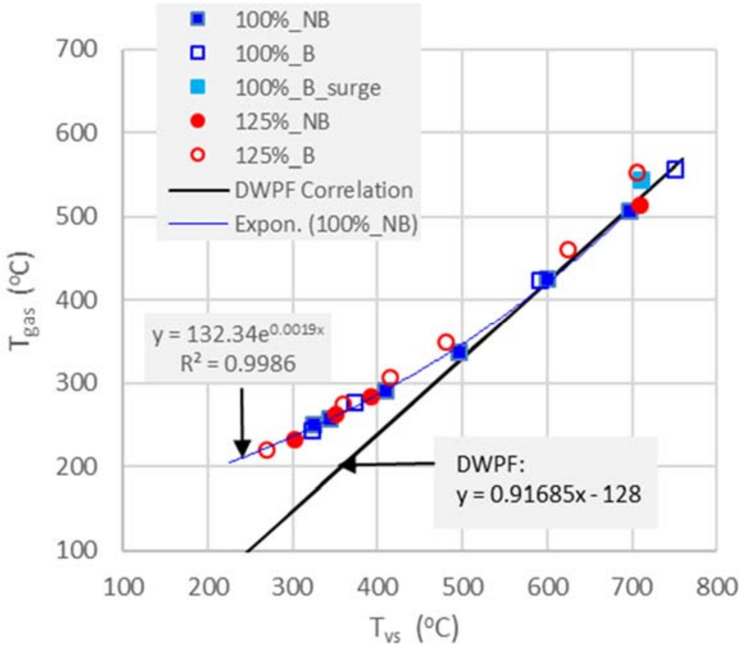

Figure 4-4. Measured T_{vs} vs. Calculated T_{gas} during Phase 2.

4.3.4.5 Nitrate Decomposition Chemistry

The calculated molar ratios of N_2 in the off-gas to the total N fed as nitrate are shown in Column "N_2 from Feed" in Table 2-11. As the measured N_2-to-total N fed ratios for the 100%_NB case showed a decreasing trend with decreasing feed rate at T_{vs} > 344 °C, the calculated fractional conversions of Eq. (9) showed the same trend. Furthermore, the calculated percent air infiltration in Table 4-4 also showed a monotonically decreasing trend with feed rate or T_{vs} and the overall carbon/nitrogen balances were quite consistent for the 100%_NB case. By contrast, the remaining cases showed no correlation in any of these parameters. Thus, the 100%_NB case was chosen as the baseline for the model development. However, it will be shown later that it is not necessary for the air infiltration or N_2-partition to show a monotonic correlation with feed rate or T_{vs} in the new model construct.

The fractional conversion of Eq. (6), shown here again, was determined by matching the measured N_2O-to-total N fed ratio at each T_{gas}:

$$N_2O_5 + 2\,NO \rightarrow 2\,N_2O + \frac{5}{2}O_2 \qquad (6)$$

The fractional conversions thus determined did not vary much with feed rate or T_{gas}. However, the average fractional conversion is shown in Table 4-5 to decrease modestly from non-bubbled to bubbled operation and from 100% to 125% acid stoichiometry, although the result of the 125%_NB case is based only on one data point. As expected, the measured concentrations of N_2O and other N-species decreased with decreasing feed rate, as shown in Table 2-11; however, it appears that the decreasing trend of N_2O was also in part due to decreasing T_{gas}, as the measured N_2O per unit feed flux (thereby removing the impact of feed rate) for the 125%_B case also showed an overall decreasing trend with decreasing T_{gas}. The average concentration of N_2O per feed flux is also shown to decrease from the non-bubbled to bubbled cases but increased from the 100% to 125% acid stoichiometry feed cases.

Table 4-5. Average Fractional Conversion of Eq. (6).

Case	Average N_2O (ppm) per Feed Flux ($lb/ft^2/hr$)	Average Fractional Conversion
100%_NB	17	0.554
100%_B	13	0.465
125%_NB*	37	0.415
125%_B	19	0.280

* Represented by only one data point at the highest T_{gas} of the run.

The fractional conversion of Eq. (10), shown here again, was determined by matching the measured molar ratio of NO_2-to-total N fed:

$$NO + \frac{1}{2}O_2 \rightarrow NO_2 \tag{10}$$

As NO_2 is not thermodynamically stable at the normal operating temperatures of a melter, Eq. (10) was assumed to only occur downstream of the film cooler. The measured concentrations of NO_2 by MS in Table 2-11 are > 2X higher than those measured by FTIR, which rendered the calculated N_2 fraction negative particularly at high T_{gas}. Furthermore, the NO_x data, which is the sum of NO and NO_2, by FTIR was higher than that by MS at $T_{gas} > \sim500$ °C, which also rendered the calculated N_2 fraction negative. Thus, the measured concentrations of NO and NO_2 were revised as follows:

$$NO_2 = NO_x(MS)\ \frac{NO_2(FTIR)}{NO_x(FTIR)} \tag{18}$$

$$NO = NO_x(MS)\ \frac{NO(FTIR)}{NO_x(FTIR)} \tag{19}$$

The revised NO_2 data per Eq. (18) was used to set the fractional conversion of Eq. (10). For the baseline case, the fractional conversion was determined at all temperatures except the lowest T_{vs} = 326 °C, where the nitrogen balance was negative. The calculated fractional conversions are shown in Figure 4-5 to decrease slightly with decreasing film cooler exit temperature (T_{FC_exit}) except at T_{FC_exit} = 201 °C. This apparent anomaly at T_{FC_exit} = 201°C (or at the corresponding T_{vs} = 344 °C) led to the high NO_2/NO ratio of 0.29. Although not shown, the measured NO_2/NO ratio at the lowest T_{vs}, which was excluded due to a negative nitrogen balance, was in fact even higher at 0.46. The measured NO_2/NO ratios for all four cases are shown in Figure 4-6. The overall data trend clearly indicates that the baseline NO_2/NO ratio of 0.29 at T_{FC_exit} = 201 °C was an outlier and the NO_2/NO ratios, particularly for the 125%_B case, appear to decrease slightly with decreasing T_{FC_exit}. It is noted that the measured T_{FC_exit} at T_{vs} = 326 °C is shown in Table 2-10 to be higher than that at T_{vs} = 344 °C. This occurred because as the VS air purge was increased by 24% to reduce T_{vs} from 344 °C to 326 °C, the FC air had to be reduced by 40% to keep the CEF vacuum ≤ -4” H_2O.

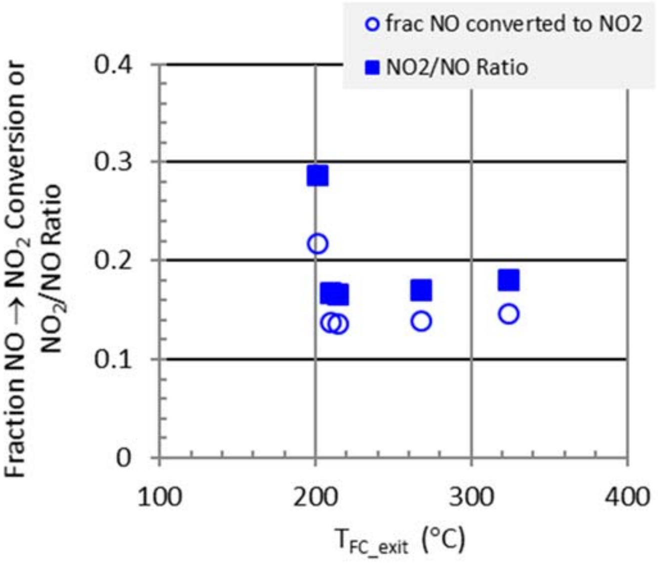

Figure 4-5. Fractional Conversion of Eq. (10) vs. T_{FC_exit} (100%_NB).

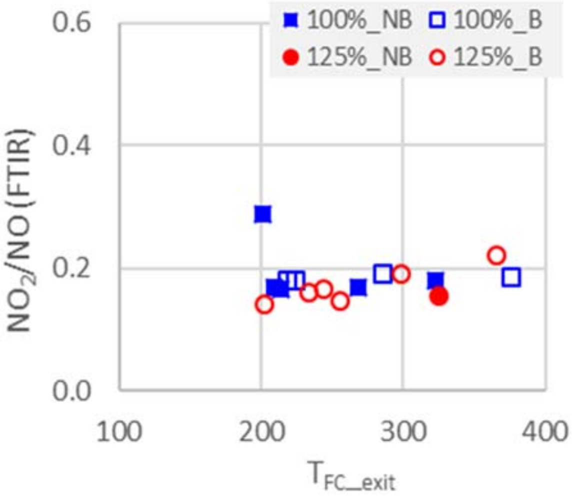

Figure 4-6. Measured NO_2/NO Ratio by FTIR During Phase 2.

Once the measured NO_2, N_2O and N_2 ratios to the total N fed as nitrate are matched, the measured NO-to-total N fed ratio would be automatically matched, unless the N_2 ratio is calculated to be negative, which is a further indication of nitrogen balance. The partitioning of N fed as nitrate in the off-gas is shown in Figure 4-7 for the baseline case; the data at T_{FC_exit} = 201 °C or T_{gas} = 257 °C was excluded. Clearly, NO was the dominant N-containing gas species at all T_{gas}, and it appears that it increased with decreasing T_{gas} at the expense of N_2. Both NO_2 and N_2O fractions remained essentially unchanged with varying T_{gas}. Although not shown, the N-partitioning profile for the 100%_B case was similar except that both NO and N_2 fractions remained relatively unchanged with varying T_{gas} like NO_2 and N_2O. Figure 4-8 shows similar profiles for the 125%_B case; they also look similar except that the N_2 fraction appears to increase slightly with decreasing T_{gas}, which is opposite to the 100%_NB case.

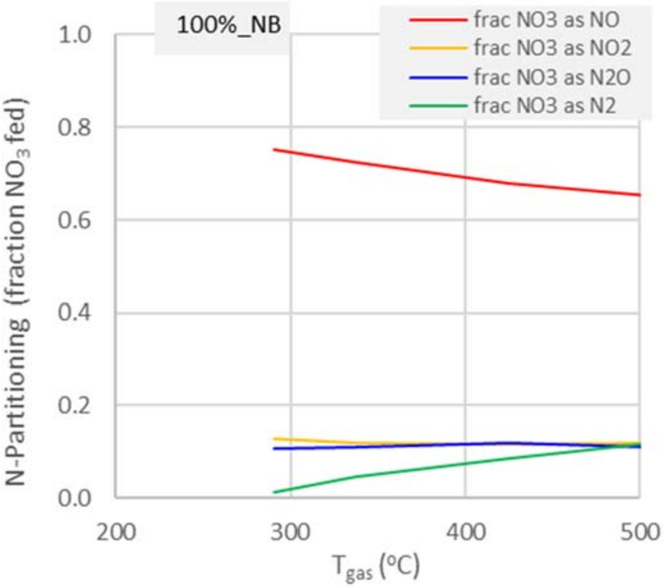

Figure 4-7. Off-Gas Partitioning of Nitrate Fed (100%_NB).

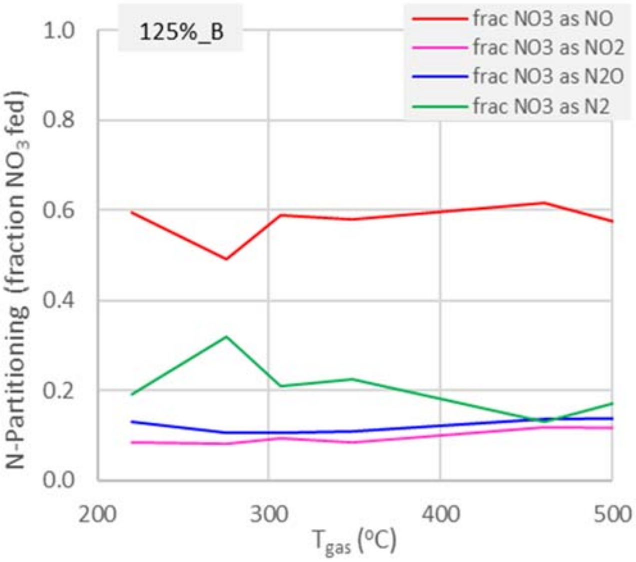

Figure 4-8. Off-Gas Partitioning of Nitrate Fed (125%_B).

4.3.4.6 Air Infiltration

The calculated air infiltration rates of the baseline 100%_NB and 100%_B cases in Table 4-4 are plotted against the feed flux in Figure 4-9. The air infiltration rates, shown as percent of the total camera air purge, provide the necessary O_2 along with that from Eq. (9) to sufficiently reduce the conservative H_2 concentration predicted by the cold cap model to 125% of the measured H_2 data in the off-gas, after combustion in the vapor space is carried out according to the existing global kinetics. Although the results for the 100%_B case are more scattered, the overall power-function fits are quite similar for both cases.

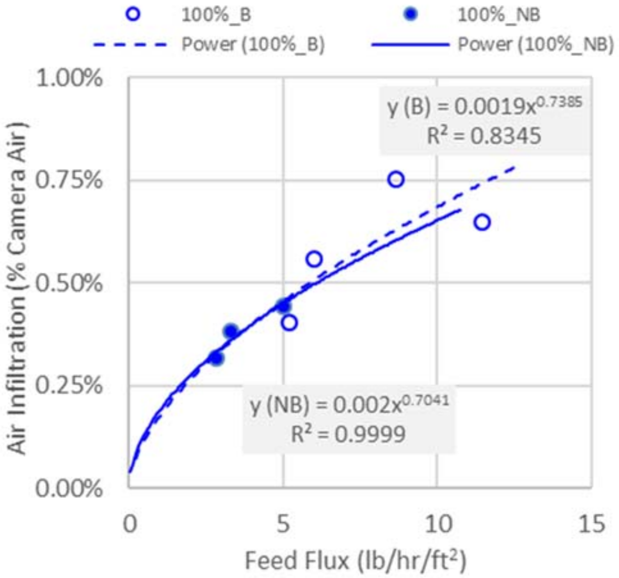

Figure 4-9. Calculated Air Infiltration of 100% Acid Stoichiometry Feeds.

However, the calculated air infiltration rates of the 125%_B and 125%_NB cases did not show any kind of trend. Nevertheless, when the O_2 inputs from air infiltration and Eq. (9) are combined, the total O_2 available for H_2/CO combustion is shown in Figure 4-10 to correlate well with the feed flux for each feed regardless of the operating mode (B or NB) and the two linear correlations are found to be quite similar.

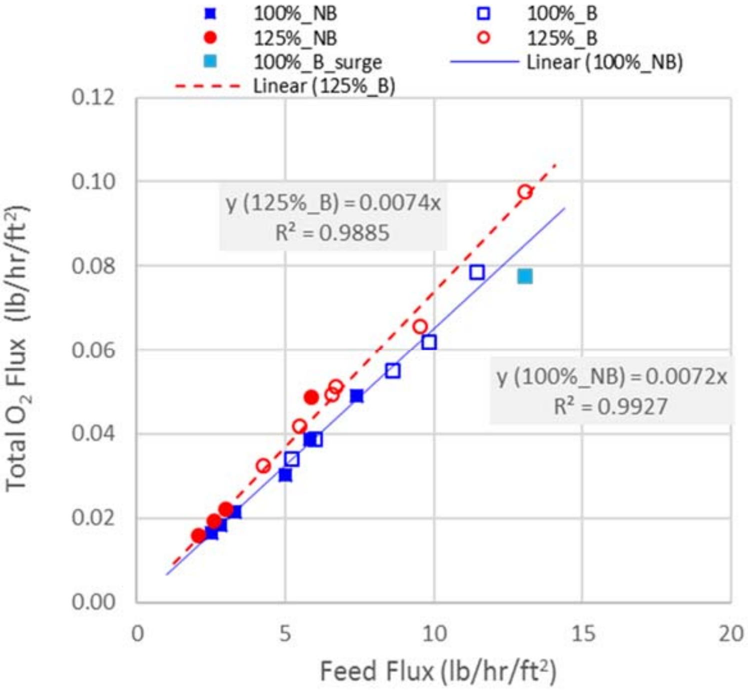

Figure 4-10. Total O_2 Flux from Eq. (9) and Air Infiltration During Phase 2.

4.3.4.7 Thermal Decomposition of Glycolic Acid

The calculated fractional conversions of Eq. (8) for the baseline case at T_{gas} < 350 °C are shown in Figure 4-11. Also plotted is the reference decomposition temperature of 100 °C, and all four data points are fitted with an exponential function, which shows that the thermal decomposition of glycolic acid would be 100% complete at T_{gas} > ~350 °C. The reason for using the exponential fit was that free glycolic acid would decompose so easily at low T_{gas} that it would not make sense to limit, for example, only 60% of it to decompose even at T_{gas} = 500 °C, if a quadratic fit with R^2 > 0.99 is used.

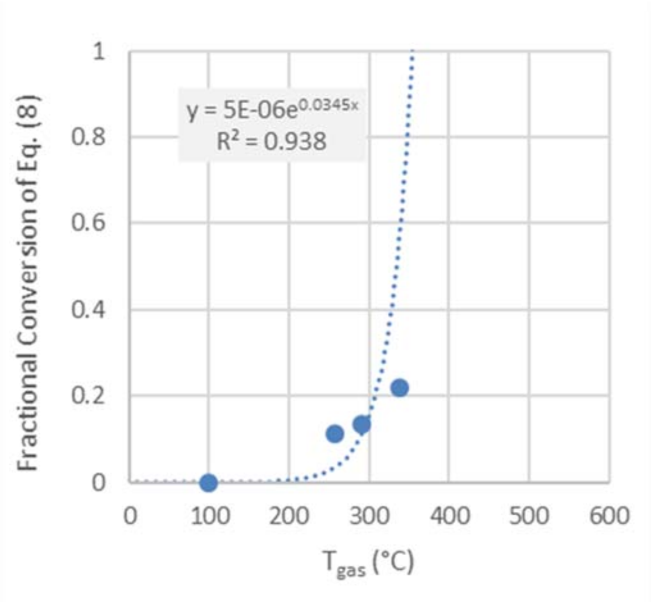

Figure 4-11. Calculated Fractional Conversion of Eq. (8) at T_{gas} < 350 °C (Baseline).

The baseline data at T_{vs} = 326 °C was excluded from the nitrate decomposition chemistry because it had a negative nitrogen balance. However, it was used for trending purposes in the derivation of a correlation between the fractional conversion of Eq. (8) and T_{gas}. Specifically, the fractional conversion of Eq. (9) was set at 0, which is in line with the overall trend seen at higher T_{gas}. The air infiltration rate was then adjusted simultaneously with the fractional conversion of Eq. (8), as in those cases with positive nitrogen balance, until 125% of measured H_2 and CO data in the off-gas were matched. The fractional conversion of Eq. (8) thus determined at T_{vs} = 326 °C (or equivalent T_{gas} = 250 °C) was 0.12, which turns out to be slightly higher than 0.11 at T_{gas} = 257 °C. It means that the fractional conversion of Eq. (8) asymptotically approaches the minimum 0.11 at T_{gas} > 257 °C. The temperature for asymptotic approach was determined to be 290 °C by solving for T_{gas} at the fractional conversion of 0.11 using the correlation shown in Figure 4-11 as Eq. (20):

$$FRAC_{C_2H_4O_3} = 5 \text{ x } 10^{-6}\, e^{0.0345\, T_{gas}},\ T_{gas} \geq 290\ °C \tag{20}$$

where $FRAC_{C_2H_4O_3}$ is the fractional conversion of glycolic acid decomposition by Eq. (8). It is noted that the data plotted in Figure 4-11 at T_{gas} = 291 °C is 0.136, which is higher than 0.11 set for T_{gas} = 290 °C. This is because the former represents the specific data determined by iteration, whereas the latter is the target value to be predicted from Eq. (20). Furthermore, the asymptotic approach to 0.11 in lieu of zero fractional conversion at 100 °C implies that T_{gas} may drop below

290 °C, the cold cap surface temperature for Eq. (20) cannot be < 290 °C. Due to this asymptotic nature, the glycolic acid decomposition model is to be based on Eq. (20) rather than the global kinetic parameters.

4.3.4.8 Results of Baseline Case

The calculated vs. measured molar flows of H_2 per mole of TOC fed are compared in Figure 4-12; the calculated values are shown to track the data perfectly as they were set to match 125% of the measured data at each T_{gas}. Unlike the NFA flowsheet, the measured H_2 data did not show any significant dependence on temperature at T_{gas} < ~430 °C.

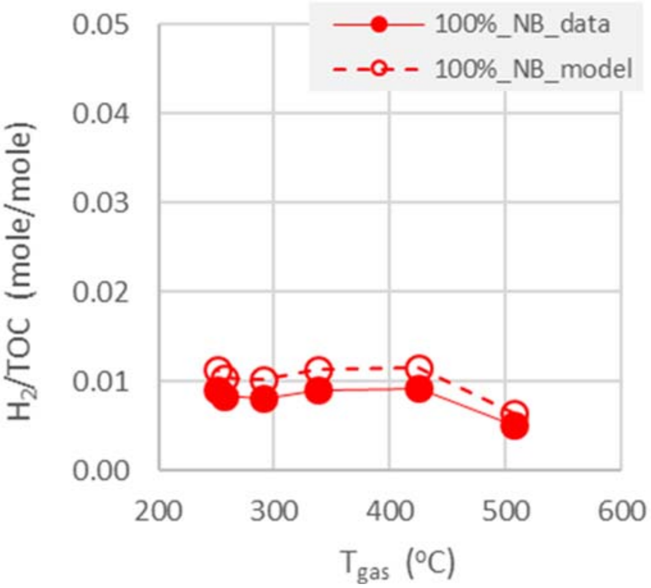

Figure 4-12. Measured vs. Calculated H_2-to-TOC Ratios for the Baseline (100%_NB).

On the other hand, the measured CO data increased continuously with increasing temperature, which appears to be counterintuitive from the combustion kinetics standpoint; as T_{gas} increases, the rate of CO combustion also increases, which should result in a net loss of CO. This seemingly counterintuitive data could be explained by comparing the rate constants of H_2/CO combustion vs. glycolic-acid decomposition, as shown in Figure 4-14. Clearly, the kinetics of glycolic acid decomposition represented by Figure 4-11 is much faster than that of either H_2 or CO combustion at T_{gas} > ~300 °C, which indicates that more H_2 and CO would be produced than consumed, as long as free glycolic acid is not depleted. Furthermore, Eq. (8) shows that each mole of glycolic acid produces two moles of CO vs. one mole of H_2. As a result, there should be a net increase in CO in the off-gas exiting the melter with increasing T_{gas}, as shown in Figure 4-13. In fact, the relative flat profile of H_2/TOC ratio in Figure 2-3 compared to that of the NFA flowsheet feed may also be explained in terms of the impact of Eq. (8), which is unique to the NGA flowsheet.

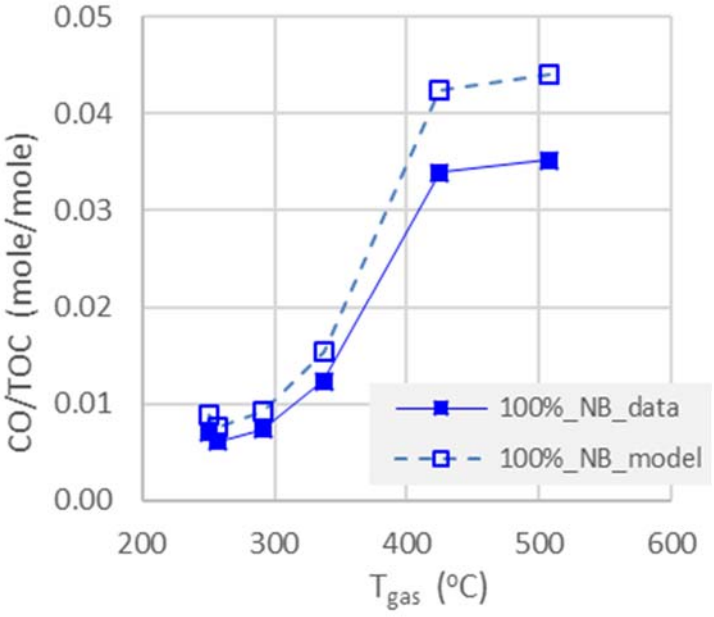

Figure 4-13. Measured vs. Calculated CO-to-TOC Ratios for the Baseline (100%_NB).

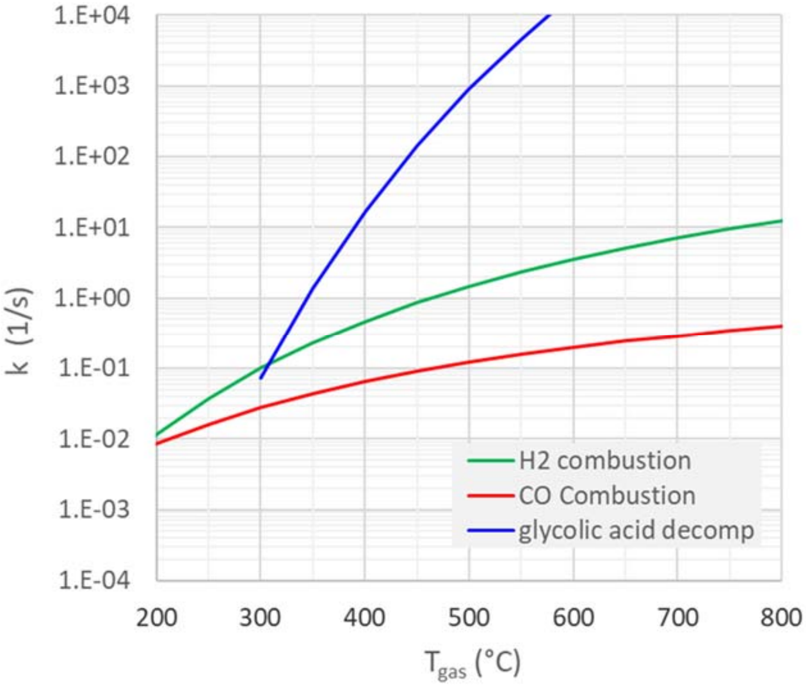

Figure 4-14. Comparison of Rate Constants for the Baseline Case.

4.3.4.9 Revised Global Kinetic Parameters of H_2/CO Combustion

The air purges not only induce good mixing in the vapor space but provide O_2 well in excess of the stoichiometric amount required to combust H_2 and CO produced in the cold cap and from the volatile carbon sources. Thus, the existing global kinetic parameters were derived using the first-order rate constant expression of the Arrhenius type:[23]

$$-r = k_0 \exp(-E_a/RT)C \tag{21}$$

where $-r$ is the reaction rate in lbmole/ft^3/sec, k_o the pre-exponential factor in 1/sec, E_a the activation energy in Btu/lbmole, R the gas constant in Btu/lbmole/K, T the representative gas temperature in K, which is equal to T_{gas}, and C the concentration of H_2 or CO in lbmole/ft^3. The term $k_0 \exp(-E_a/RT)$ in Eq. (21) represents the global first-order rate constant, *k*:

$$k = k_0 \exp(-E_a/RT) \tag{22}$$

Taking logarithm on both sides of Eq. (22) gives:

$$\ln k = ln\, k_0 - (E_a/R)\,(1/T) \tag{23}$$

The first-order rate constant *k* is calculated by integrating Eq. (21) at each T_{gas}:[33]

$$k = \frac{F_i\, X}{F_0\, \tau} \tag{24}$$

where F_i and F_o are inlet and out flow rates of H_2 or CO in lbmole/hr, *X* the fractional conversion, and τ the gas residence time in the vapor space in sec. Once the first-order rate constant k is evaluated at each T_{gas} by substituting in the values of F_i, F_o and τ from the spreadsheet along with the calculated *X*, the results are plotted in terms of *ln k* vs. *1/T* for H_2 and CO in Figure 4-15 and Figure 4-16, respectively.

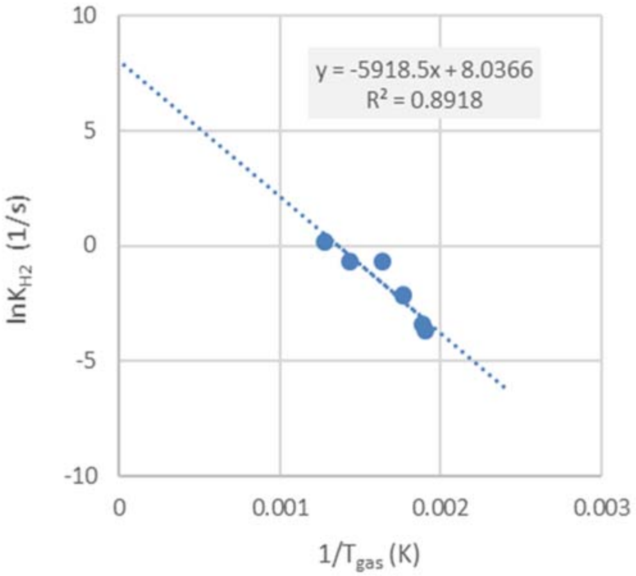

Figure 4-15. ln k vs. 1/T for H_2 Combustion for the Baseline Case.

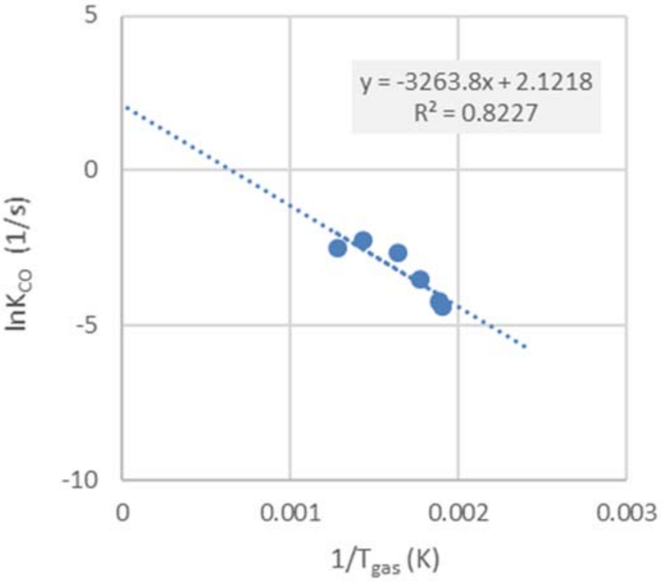

Figure 4-16. ln k vs. 1/T for CO Combustion for the Baseline Case.

The values of k_o and E_a were estimated from the slope and y-intercept of each *ln k* vs. *1/T* plot. For example, the kinetic parameters of H_2 combustion were calculated as follows:

$$k_o = \exp(y - intercept) = \exp(8.0366) = 3{,}092.08\ sec^{-1} \tag{25}$$

$$E_a = (-slope)(R) = (5{,}918.4\ K/sec)(3.57452\ Btu/lbmole/K) = 21{,}155.8\ Btu/lbmole \tag{26}$$

The resulting revised first-order global kinetic parameters of H_2 and CO combustion in the vapor space are tabulated in Table 4-6. In Revision 0,[4] these kinetic parameters were derived for each of the four cases of Phase 2. In Revision 1, the baseline kinetic parameters in Table 4-6 were applied to the remaining cases using the air infiltration as the only adjustable parameter to match 125% of the measured H_2 data.

Table 4-6. Revised First-Order Global Kinetic Parameters of Vapor Space Combustion.

Species	k_o (1/sec)	E_a (Btu/lbmole)	R^2
CO	8.35	11,666.5	0.823
H_2	3,092.08	21,155.8	0.892

In Figure 4-17, the profile of the revised first-order rate constants of H_2 combustion is compared to those based on the existing parameters and those derived in Revision 0 for the same 100%_NB case. The revised rate constants are shown to be lower than those derived in Revision 0 at all T_{gas}. However, they are still higher than the current model at T_{gas} < ~300 °C, which suggests that the current model predicts too slow a combustion rate compared to the measured H_2 data during Phase 2.

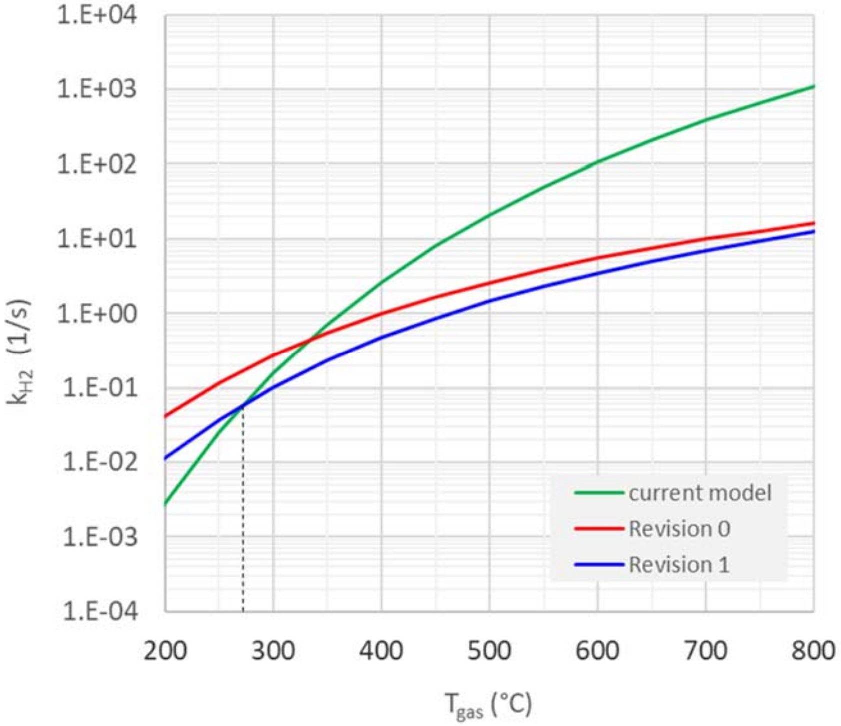

Figure 4-17. Comparison of First-Order Rate Constants of H_2 Combustion.

4.3.4.10 Kinetics of NO to NO_2 Oxidation

It was assumed that any NO_2 detected in the off-gas was due to the oxidation of NO downstream of the film cooler. The fractional conversion of Eq. (10) thus calculated by matching the revised NO_2 data per Eq. (18) was fitted into the first-order global kinetics model by following the same steps used for the combustion of H_2 and CO, i.e., Eq. (21) – Eq. (26). The first-order kinetics (in terms of NO) at the measured T_{FC_exit} was justified as air was present in even greater excess with the addition of cooling air at the film cooler. The *ln k* vs. *1/T* plot is shown in Figure 4-18 for the 125%_B case, as an example. As evidenced by an order-of-magnitude smaller slope, the rate of NO oxidation was found to be much slower than that of H_2 or CO combustion.

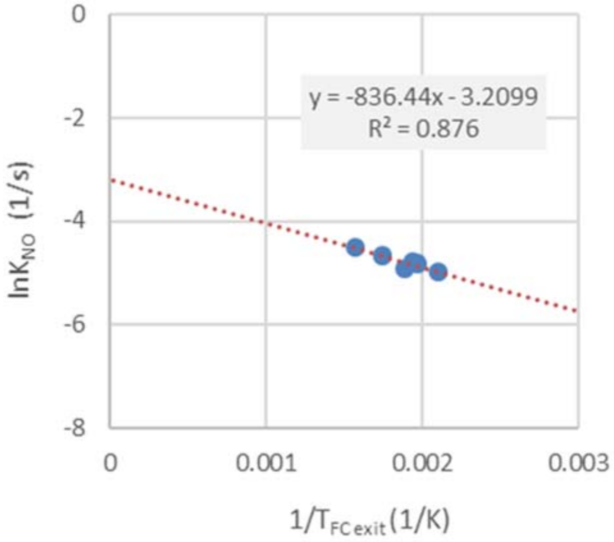

Figure 4-18. ln k vs. 1/T for Oxidation of NO during the 125%_B Run.

The resulting first-order kinetic parameters are compared in Table 4-7 for the baseline 100%_NB, 100%_B and 125%_B cases; the kinetic parameters for the 125%_NB case are not listed as it had only one data point with good nitrogen balance. The kinetic parameters for the two 100% acid stoichiometry cases are similar and their kinetic rates are ~20% slower than that of the 125%_B case. It is noted that unlike the kinetic parameters for the H_2 and CO combustion, those kinetic parameters shown for the baseline case were not used to predict the NO oxidation rates for the 100%_B and 125%_B cases. Instead, the measured NO_2 concentrations were precisely matched by adjusting the fractional conversion of Eq. (10) for each case.

Table 4-7. First-Order Kinetic Parameters of NO + ½ O_2 = NO_2.

Cases	k_o (1/sec)	E_a (Btu/lbmole)	R^2
100%_NB	0.012	700.2	0.853
100%_B	0.010	316.9	0.369
125%_B	0.040	2,989.9	0.876

4.3.5 *Application of 100%_NB Model*

The new model parameters derived for the baseline case were applied to the remaining cases, as described in Section 4.1:

1. Adjust the fractional conversions of Eq. (9), Eq. (6) and Eq. (10) until the measured N_2, N_2O and NO_2 concentrations in the off-gas, respectively, are matched.
2. Set the fractional conversion of Eq. (8) using Eq. (20).
3. Set the rate constants of H_2 and CO combustion using the global kinetic parameters given in Table 4-6.
4. Adjust the air infiltration rate until 125% of measured H_2 data in the off-gas is matched.

The fractional conversions of Eq. (9) and the air infiltration rates thus determined are shown in Table 4-4. It was noted earlier that although the amount of additional O_2 produced from Eq. (9) and that from air infiltration individually did not vary in any consistent manner from one steady state to the next, except for the baseline case, the total O_2 flux showed a good correlation with the feed flux for each acid-stoichiometry and the two correlations turned out to be quite similar, as shown in Figure 4-10.

The predicted CO concentrations in the off-gas for the 100%_B, 125%_NB and 125%_B cases are compared against measured data in Figure 4-19, Figure 4-20 and Figure 4-21, respectively. It appears that the baseline model over-predicted the data at $T_{gas} > 300$ °C but under-predicted at $T_{gas} < 300$ °C for the bubbled runs. However, the model still captured the slightly upward data trend at $T_{gas} < 300$ °C reasonably well and the degree of under-prediction was relatively small. Considering that the predicted H_2 was set at 25% higher than the data and the lower flammability limit (LFL) of H_2 is ~1/3 of CO, the overall flammability potential predicted by the model should still be higher than that based on measured H_2 and CO. In Figure 4-20, the predicted CO for the non-bubbled run (125%_NB) is shown to be higher than the data at all T_{gas}.

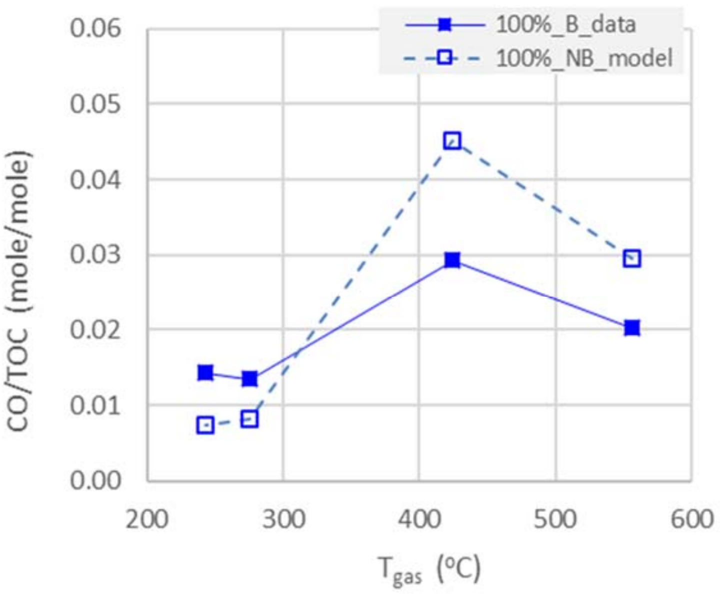

Figure 4-19. Measured vs. Predicted CO/TOC Ratio (100%_B).

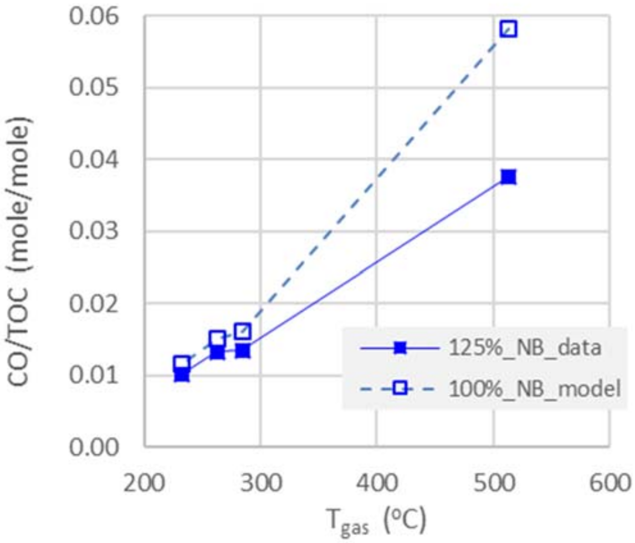

Figure 4-20. Measured vs. Predicted CO/TOC Ratio (125%_NB).

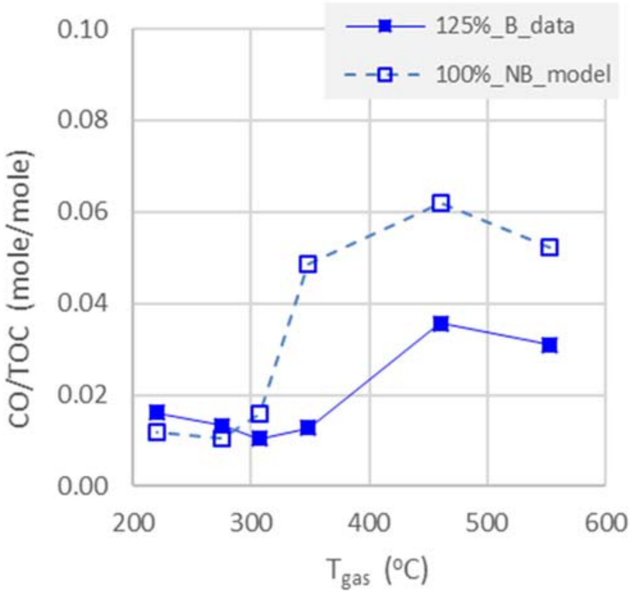

Figure 4-21. Measured vs. Predicted CO/TOC Ratio (125%_B).

4.3.6 *Validation of Model against Pressure Spike Data*

The new model parameters were tested further against the data taken during the +13 "H_2O spike, which occurred at 17:34 hour on 3/14/2014 just past 436.5-hour mark, as shown in Figure 4-22. The CEF vapor space pressure rose from -5.3 to +8.3 "H_2O for a total rise of +13.6 "H_2O and the spike lasted for ~7 minutes before a second pressure spike to 0.0 "H_2O began. The measured H_2 data by MS began to rise immediately and reached its peak 8 seconds after the peak pressure, which was expected due to the lags associated with the off-gas sampling/analysis and, to a lesser extent, the vapor space gas mixing. The H_2 data by GC was not used as its sampling time of 4 minutes was too long compared to the time scale of pressure transients being discussed here. The measured CO_2 data by MS formed a very broad peak and, as a result, did not reach its peak until ~3 minutes after the peak pressure.

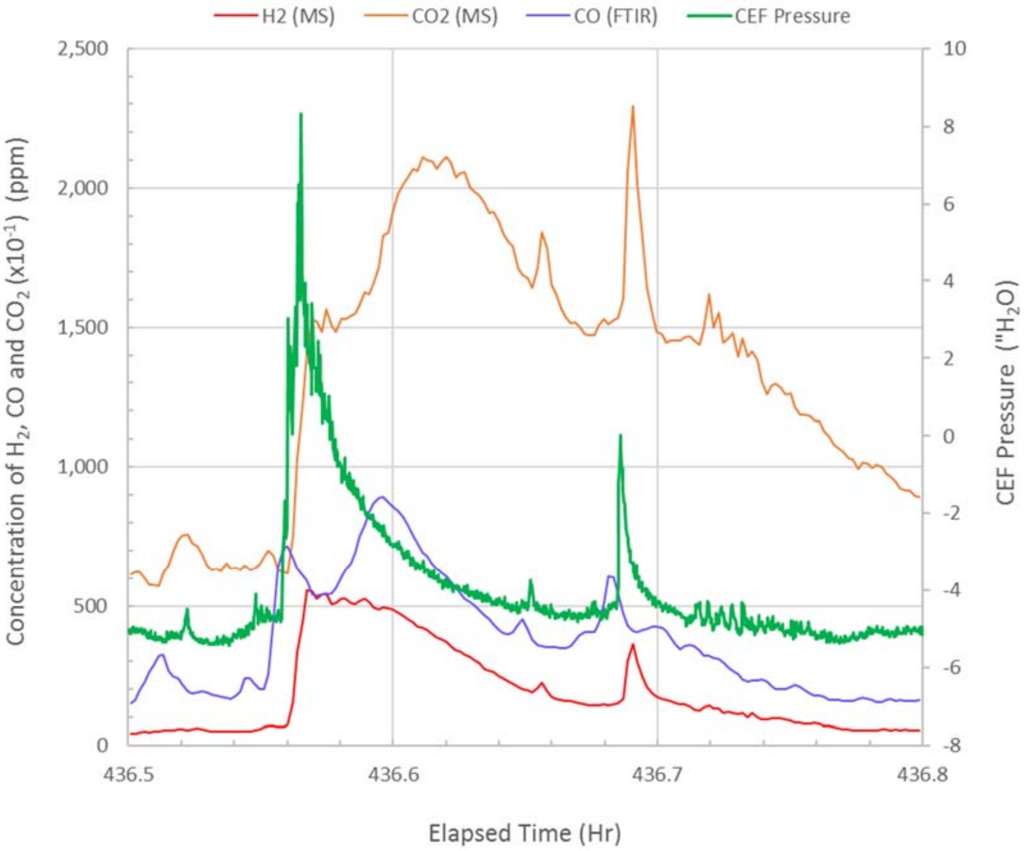

Figure 4-22. +13 "H_2O Pressure Spike During 100%_B_Surge Run.

The pressure/concentration spikes shown in Figure 4-22 are highly dynamic in nature and can be best simulated using the MOG dynamics model;[22] however, it was beyond the scope of this study. Instead, the baseline model was validated in two stages. First, the mass and energy balance calculations were performed using the steady state data taken over the 1-hour period prior to the pressure spike and the model parameters, including the unknowns (air inleakage and T_{gas}) were calculated and confirmed against those predicted using the correlations derived for the baseline case. Second, the magnitudes of off-gas surges that led to the +13" H_2O spike were estimated by matching the peak off-gas flow through the film cooler and CO_2 (MS) data. Doing so would help determine if the predicted peak concentrations of H_2 and CO at the height of surge would bound their respective maximum measured data.

4.3.6.1 Validation against Steady State Data

The pressure spike occurred while the CEF was being fed with the 100% acid stoichiometry feed with the bubblers turned on so the data is labeled as 100%_B_surge. The average feed rate during the 1-hour period was 227 g/min at the average T_{vs} = 704 °C. The average glass pour rate of 74 g/min was within 5% of the theoretical value based on the average feed rate, which indicates steady state operation. The carbon balance was also good, i.e., off by -8.3%. The calculated air inleakage rate and T_{gas} were also in good agreement with their respective correlations, as shown in Figure 4-3 and Figure 4-4. The rate of air infiltration was adjusted until the predicted H_2 equaled 125% of the measured H_2 data by MS, as shown in Table 4-8. The target N_2-to-total N fed ratio of 0.21 for Eq. (9) was close to 0.23 of the 100%_B case at T_{vs} = 750 °C shown in Table 4-4. The calculated total O_2 flux from Eq. (9) and air infiltration is shown in Figure 4-10 to be a little below that predicted by the correlation for the baseline case but well within the uncertainty of data. The predicted concentration of CO is shown to be 5% higher than the average FTIR data.

Table 4-8. Steady State and Bounding H_2 and CO during +13" H_2O Pressure Spike.

Operating Mode	Variable	Data	Model	Model/Data
Steady State	CO (ppm)	180	189	1.05
	H_2 MS (ppm)	35	44	1.25
Bounding	CO (ppm)	893	1,252	1.40
	H_2 MS (ppm)	558	751	1.35

4.3.6.2 Validation against Bounding Data

A pressure spike is induced by a sudden surge in the condensable and non-condensable off-gas flows from the cold cap. When the magnitude of surge is large, T_{vs} can drop significantly, as it did from 704 to 465 °C during the +13 "H_2O spike, as shown in Figure 2-7. However, it took nearly 2 minutes for T_{vs} to reach its minimum after the pressure peaked, compared to the 8-sec delay in the H_2 response. Thus, the input for the surge simulation consisted of the maximum ΔP/concentration data coupled with the interpolated temperature data at the time of peak pressure, as shown in Table 4-9, rather than the minimum temperatures.

The magnitude of non-condensable flow surge was determined by adjusting up the steady state calcine gas flow rate until the calculated CO_2 concentration downstream of the film cooler (FC) matched the measured data by MS. On the other hand, the magnitude of condensable flow surge was determined by adjusting up the flows of free H_2O and volatiles in the feed until the calculated off-gas flow at the FC exit matched that predicted by the correlation between the off-gas flow vs. $\sqrt{\Delta P_{FC}}$ at the maximum ΔP_{FC} of 4.25 "H_2O. Since the vapor space pressure was positive, the direction of air inleakage was reversed, i.e., it was the off-gas that leaked out, whose rate was estimated by extrapolating the air inleakage vs. $\sqrt{\Delta P}$ correlation to the maximum ΔP between the vapor space and the surrounding air, i.e., -(8.3-0) = -8.3 "H_2O. Finally, T_{gas} was calculated by matching the measured off-gas temperature at the FC exit (T_{FC_exit}) of 407 °C.

The results of surge calculations are shown in Table 4-9. The magnitude of the condensable surge was calculated to be 12.5X the pre-surge steady state condensable flow, while that of the non-condensable surge was calculated to be 2.8X the pre-surge steady state non-condensable flow based on the measured CO_2 data by MS. It is noted that the calculated surge magnitude for condensable flow is higher than the NFA flowsheet condensable surge basis of 9X the normal, whereas that of non-condensable flow is lower than the NFA flowsheet non-condensable surge basis of 5X the normal.[29] Although the condensable flow surge lowers the combustion kinetics by lowering both T_{gas} and gas residence time, it is the non-condensable flow surge that sets the fuel flows and thus directly impacts the flammability potential. Although these calculated surge magnitudes may not be as accurate as those that would have been estimated from the dynamic simulation, the reduction in the non-condensable surge magnitude appears to be large enough to conclude that the overall impact of surge on the off-gas flammability potential of the NGA flowsheet feed would be lower than that of the NFA flowsheet feed.

Table 4-9. Input/Output of +13 "H_2O Spike Simulation.

Input Data	Value	Model Output	Value
Maximum CEF Pressure ("H_2O)	+8.30	Air Inleakage (lb/hr)	-70
T_{vs} at peak pressure (°C)	630	T_{gas} (°C)	469
Maximum P_{FC_exit} ("H_2O)	+4.06	Off-Gas Flow at FC Exit (scfm)	98.84
$T_{FC\ exit}$ at peak pressure (°C)	407	Surge Magnitude (X Baseline):	
Maximum ΔP_{FC} ("H_2O)	4.25	- Condensable	12.5
Maximum CO_2 by MS (vol%)	2.113	- Non-Condensable	2.8
Maximum NO (ppm)	9,228	NO (ppm)	9,229
Maximum NO_2 (ppm)	3,972	NO_2 (ppm)	3,972
Maximum N_2O (ppm)	911	N_2O (ppm)	911
N_2/total N fed (mole/mole)	0.1744	N_2/total N fed (mole/mole)	0.1743

The calculated off-gas out-leakage rate of 70 lb/hr amounted to 28% of the total gas input into the vapor space, which means that the off-gas flow exiting the melter amounted to 72% of the calcine gases produced from the feed and the added air purges. The calculated T_{gas} was 160 °C lower than T_{vs}, which equals the ΔT during steady state. The calculated peak concentrations of H_2 and CO in the off-gas bounded the maximum measured values by a factor of 1.35 and 1.40, respectively, as shown in Table 4-8.

4.3.7 *Additional Discussion on Carbon Balance*

One of the major difficulties encountered in this study was achieving reasonable carbon balances, which were calculated per Eq. (15). As shown in Table 4-4, carbon balances were off by more than ±15% in 16 out of 26 steady state runs. Of those 16 runs, 5 runs had carbon balances off by more than ±25% and thus were excluded from the model development. Furthermore, carbon balances were negative in all but 2 steady state runs, which indicates that the calculated total carbon flow in the off-gas was consistently lower than that based on the measured CO and CO_2 data. Much of the negative carbon balance issue could have been mitigated had the glycolate concentration in each feed been adjusted up to match the measured TOC data in Table 2-9.

For the two 125%_B runs with non-negative carbon balance, it is suspected that steady state was not likely achieved as well as in the other runs because large fluctuations in the data forced the original 2-hr duration to be reduced to ~1 hour in an effort to find periods with less fluctuations. However, less fluctuations in the data do not necessarily indicate that the system is at steady state unless they can be maintained for a sufficiently long period of time. Thus, it is conceivable that the carbon balances of the two 100%_B runs could have been rendered positive when the unsteady feeding/calcination rates in the cold cap were coupled with the under-estimated TOC in the feed. Ideally, the calculated total carbon flows need to be somewhat higher than those measured (i.e., a positive carbon balance), thus leaving some fraction of the carbon fed to get entrained in the off-gas. Significant entrainment of the feed and glassy materials in the off-gas was confirmed even under non-bubbled conditions by the analytical results of the actual DWPF and CEF condensate samples.[34,3]

The large negative carbon imbalance in Phase 2 data is consistent with the results shown in Table 2-9 that the remediated feeds had up to 18% lower TOC than the measured TOC_{DWPF} even after assuming 100% retention of the antifoam added during the SRAT processing. The accuracy and consistency of the TOC_{DWPF} data was confirmed against the total carbon emission data during batch melting of the same feeds in argon-purged crucibles and the DWPF SME551-565 analytical data, including the TOC analysis.[17,19] By contrast, all three total carbon estimates based on the IC, TOC analysis and crucible runs agreed well for the NFA flowsheet feed used in Phase 1 as well as the SB8-D3 simulant, as shown in Table 2-4. All this points to the possibility that the current analytical technique under-estimated glycolate in the Phase 2 feeds.

4.4 Discussion on REDOX

The calculated REDOX of the NFA and NGA flowsheet feeds used during Phase 1, Phase 2, and batch-melting tests in argon-purged crucibles are compared against the measured data in Table 4-10, where the given TOC values are identical to the TOC_{cruc} data in Table 2-4. It is striking to see how widely the REDOX of the CEF Phase 1 (CEF1) baseline feed varied depending on the melting apparatus used. The highest REDOX of 0.64 was measured for the remaining glass after a 10g batch was boiled, calcined and melted in an argon-purged crucible. Argon-purging not only eliminated the potential for air inleakage and but helped purge out any calcine gases emitted from the batch. Due to the small batch size, however, there is also a possibility that argon purging may not have allowed enough time for gases to undergo the equilibrium reactions with the remaining batch before being swept away.

On the other hand, the probability of such equilibrium reactions occurring in the batch is higher in closed crucibles, which may provide a partial explanation to its lower REDOX of 0.26. However, a certain degree of uncertainty exists regarding the effectiveness of the sealant in terms of eliminating air inleakage but still allowing the calcine gases to exit. If the calcine gases can be suppressed from leaving the batch early, it should make the crucible data more representative of the REDOX under actual melter conditions. This is because the glass residence time in a melter is at least an order-of-magnitude longer than the typical 1-hr heating at 1,150 °C in the crucible. Interestingly, the cold cap model predicted the REDOX that lies exactly at the midpoint of the two aforementioned values.

Table 4-10. Comparison of Measured vs. Calculated REDOX of Phase 1 and Phase 2 Feeds.

Feed	Reductant	TOC (mg/kg)	Redox			
			Ar-purged crucible	closed crucible - ramp	cold cap model	CEF glass
CEF1_Baseline	Formic	12,789	0.64	0.26	0.45	0.08-0.2
CEF1_Baseline_1% O_2 in Ar purge	“	13,392	0	-	-	-
SB8-D3_Baseline	“	17,209	0.30	0.21	0.11	-
SB8-D3_1600ppm-AC Spike_Fresh	“	17,311	0.49	-	-	-
SB8-D3_1600ppm-AC Spike_Boiled	“	18,315	0.48	-	-	-
SB8-D3_1600ppm-PEG C Spike_Boiled	“	20,610	0.46	-	-	-
CEF2_100% Acid_Baseline	Glycolic	16,178	0.27	0.25	0.11	0
CEF2_100% Acid_1000ppm AC Spike	“	15,623	0.22	-	-	-
CEF2_100% Acid_1476ppm AC Spike	“	-	0.57	0.44	-	0

The REDOX of glass samples pulled from the CEF during Phase 1 ranged from 0.08 and 0.2. As noted elsewhere,[8] the upper end of this REDOX range occurred during the initial stage of feeding with active argon bubbling of the melt pool to facilitate the melter turnover, while the lower end occurred near the end of steady state testing at low feed rates under non-bubbled conditions. In fact, had the initial feeding been continued, the upper bound could have been pushed higher to a value near or even above the closed crucible data. However, the two redox values would not be directly comparable as the argon-bubbling is known to increase the REDOX of the DWPF glass by 0.1,[22] while the closed crucible data was obtained without bubbling. When the argon purge was mixed with air at a target of 1% O_2, the resulting glass was completely oxidizing, indicating a REDOX drop of at least 0.64. This result shows how strong an effect the gas phase above the cold cap has on the cold cap chemistry and REDOX.

When a 10-g batch of SB8-D3 slurry, also based on the NFA flowsheet, was melted in an argon-purged crucible, the resulting glass proved more oxidizing than the Phase 1 glass despite the fact the former feed had a 35% higher TOC than the latter. This can be explained by the difference in nitrate, as shown in Table 2-4; the SB8-D3 had a 74% higher nitrate than the Phase 1 feed. The REDOX measured in a closed crucible was also lower but by only 0.05 compared to a decrease of 0.34 in argon-purged crucible. The cold cap model also predicted a lower REDOX and the magnitude of decrease was exactly the same at 0.34. As expected, the glasses made from the next three SB8-D3 feeds spiked with additional carbons in argon-purged crucibles were all similarly reducing at a REDOX of just under 0.5.

When the 100% acid stoichiometry NGA flowsheet feed used in Phase 2 was melted in the argon-purged and closed crucibles, both glasses had nearly the same REDOX 0.27 vs. 0.25. The cold cap model predicted more oxidizing glass at a REDOX of 0.11. However, the glass samples pulled during Phase 2 were all completely oxidized except for the few samples taken early on during the melter turnover. In fact, the Phase 2 glass remained completely oxidized even with feeds spiked with 2X antifoam and after the CEF was continuously fed round-the-clock for 4+ days with argon bubbling at 2X the DWPF bubbling flux. Glass did not become completely oxidized in Phase 1 under similar operating conditions and the main difference between Phase 1 and Phase 2 runs was in the feed chemistry, i.e., the formic vs. glycolic acid in the reductant space. More importantly, each carbon in the NGA flowsheet feed required ~4X more nitrate than the NFA flowsheet feed, i.e., the TOC-to-nitrate ratio of the NGA flowsheet was ~¼ that of the NFA flowsheet.[36] All this seems to suggest that given adequate time for the calcine gases to equilibrate with the remaining batch as in a melter, the excess O_2 produced from the nitrate decomposition is likely to drive the REDOX of the NGA flowsheet glass to zero.

For example, when the Phase 2 feed was spiked with 1,476 ppm of additional antifoam carbon, which is equivalent to a 2X spike, the resulting glass made in the argon-purged crucible is shown in Table 4-10 to be quite reducing at a REDOX of 0.57, while the glass made in a closed crucible was less reducing, as expected, at a REDOX of 0.44. Clearly, either REDOX data is nowhere near the measured value of zero for the glass samples pulled from the CEF during the Phase 2 run. It is noted that although a potential for air-glass contact existed, the glass residence time in the CEF was on the order of 20 hours, which is considerably longer than any of the bench-scale melting apparatuses discussed so far. Two additional melting apparatuses, closed crucible-hot (CC-hot) and Melt Rate Furnace (MRF), have since been used and further discussions are given elsewhere on the impact of melting apparatus on the REDOX.[35]

5.0 Conclusions and Recommendations

Based on the results of the CEF Phase 2 data analysis and subsequent model revision discussed so far, the following conclusions are drawn:

1. At $T_{gas} < 400$ °C, where the potential for off-gas flammability could increase appreciably, the NGA flowsheet feed produces ¼ of the H_2 produced from the NFA flowsheet feed on a per carbon basis.

2. A new off-gas surge basis has been defined for the NGA flowsheet; it consists of 13X normal condensable and 3X normal non-condensable flows for bubbled operation. Although a higher condensable surge would lower the combustion kinetics more, the fuel flows are set directly by the non-condensable surge. Thus, compared to the 9X/5X NFA flowsheet surge basis, off-gas surges are expected to be somewhat less impactful on the flammability potential of the NGA flowsheet melter off-gas.

   For non-bubbled operation, the existing surge basis of 3X normal condensable and 3X normal non-condensable (3X/3X) for the NFA flowsheet is still bounding.

3. The DWPF melter off-gas chemistry model has been revised for the NGA flowsheet - its new parameters were set to match, as a conservative measure, 125% of the measured H_2 and CO data during Phase 2 for the baseline case with 100% acid-stoichiometry feed under non-bubbled conditions. The baseline model was shown to predict both the steady state and bounding H_2/CO data taken during the +13 "H_2O pressure spike well.

4. All glass samples taken during Phase 2 were fully oxidized (i.e., $Fe^{2+}/\Sigma Fe = 0$) even under the test conditions designed to induce reducing conditions in the feed (spiked with 2-3X normal antifoam) and in the melt pool (bubbled with argon at 2X DWPF bubbling flux) along with the efforts to minimize the air-glass contact by continuously feeding/pouring at very high rates round-the-clock for 4 straight days.

5. The existing correlation used to estimate the true gas temperature in the DWPF melter vapor space from the measured data (TI4085D) for the combustion kinetics calculations is conservative, which confirms the earlier findings of the Phase 1 test.

6. The results of carbon balance on the analytical data for the Phase 2 feed samples and the off-gas data suggest that the current analytical method used to detect the glycolate is under reporting it. Specifically, based on the analysis of feed sample data, the reported glycolate may be low by up to 18-20%.

It is recommended that:

1. The current analytical method for glycolate be optimized to reduce the detected bias in glycolate data. The new analytical results should be compared against the difference between the measured TOC_{DWPF} and the sum of carbons from the IC analysis and antifoam carbon from the recipe (Section 4.3.6.2.

2. As the nitrogen balance suggests that excess nitrate may be influencing measured REDOX data, the current REDOX method should be re-evaluated and further optimized to better reflect the role of varying TOC-to-nitrate ratio (Section 4.4).

3. The new parameters added to the revised DWPF melter off-gas chemistry model be validated prior to using the model for process optimization purposes.

6.0 References

1. Wagnon, T. J., “Defense Waste Processing Facility Alternate Reductant Systems Engineering Evaluation,” ***G-AES-S-00003***, ***Rev. 0***, Savannah River Remediation, Aiken, SC, 2011.

2. Johnson, F. C, and Miller, D. H., “Nitric-Glycolic Acid Flowsheet Melter Flammability Testing: 2014 Phase 2 CEF Run R&D Directions,” ***SRNL–L3100–2014–00007, Rev. 1***, Savannah River National Laboratory, Aiken, SC, 2014.

3. Johnson, F. C., Stone, M. E., and Miller, D. H., “Alternate Reductant Cold Cap Evaluation Furnace Phase II Testing,” ***SRNL-STI-2014-00157, Rev. 0***, Savannah River National Laboratory, Aiken, SC, 2014.

4. Choi, A. S., “DWPF Melter Off-Gas Flammability Model for the Nitric-Glycolic Acid Flowsheet,” ***SRNL-STI-2014-00355***, ***Rev. 0***, Savannah River National Laboratory, Aiken, SC, 2014.

5. Choi, A. S., and Lee, S. Y., “Impact of Melter Internal Design on Off-Gas Flammability,” ***SRNL-STI-2012-00121***, ***Rev. 0***, Savannah River National Laboratory, Aiken, SC, 2012.

6. Choi, A. S., "DWPF Melter Off-Gas Flammability Assessment," ***X-CLC-S-00164***, ***Rev. 4***, Savannah River National Laboratory, Aiken, SC, 2010.

7. Abramowitz1, H., Calloway, B., Mecholsky N., D’Angelo1, N., Windham, J., and Coleman, J., “Analysis of Bubbled vs. Non-Bubbled DWPF Operating Data,” ***SRR-LWP-2018-0002***4, Savannah River Remediation, Aiken, SC, 2013.

8. Choi, A. S., “2013 CEF Run – Phase 1 Data Analysis and Model Validation,” ***SRNL-STI-2013-00705***, ***Rev. 0***, Savannah River National Laboratory, Aiken, SC, 2014.

9. Holtzscheiter, E. W., “Nitric-Glycolic Acid Flowsheet Melter Flammability Testing,” ***HLW-DWPF-TTR-2013-0002***, ***Rev. 1***, Savannah River Remediation, Aiken, SC, 2016.

10. Yeung, M. R., and Boyd, C. M., “DWPF Melter Off-Gas Flammability,” ***U-CLC-S-00003***, ***Rev. 2***, Savannah River Remediation, Aiken, SC, 2017.

11. Stone, M. E., “Feed Preparation for Alternate Reductant Melter Testing,” ***SRNL-L3100-2013-00109***, Savannah River National Laboratory, Aiken, SC, 2013.

12. Lambert, D. P., “Batching Recipe: 100% Koopman Acid Stoichiometry Nitric/Glycolic Acid Flowsheet Melter Feed,” ***SRNL-L3100-2013-00036***, Savannah River National Laboratory, Aiken, SC, June 19, 2013.

13. Lambert, D. P., “Batching Recipe: 125% Koopman Acid Stoichiometry Nitric/Glycolic Acid Flowsheet Melter Feed,” ***SRNL-L3100-2013-00064***, Savannah River National Laboratory, Aiken, SC, June 19, 2013.

14. Choi, A. S., "DWPF Melter Off-Gas Flammability Assessment (Sludge Batch 8)," ***X-CLC-S-00164***, ***Rev. 8***, Savannah River National Laboratory, Aiken, SC, 2013.

15. Lambert, D. P., “Acceptance of Harrell Batch 6B61 100% Glycolic Nitric Acid Flowsheet SRAT Product,” ***SRNL-L3100-2013-00118, Rev. 0***, Savannah River National Laboratory, Aiken, SC, 2013.

16. Lambert, D. P., “Acceptance of Harrell Batch 6B61 125% Glycolic Nitric Acid Flowsheet SRAT Product,” ***SRNL-L3100-2013-00146***, Savannah River National Laboratory, Aiken, SC, 2013.

17. Amoroso, J. W., and Zamecnik, J. R., “Measurement of Offgas Species from Thermal Decomposition of Simulated DWPF Melter Feed,” ***SRNL-STI-2014-00286, Rev. 0***, Savannah River National Laboratory, Aiken, SC, 2014.

18. Koopman, D. C., and Zamecnik, J. R., "DWPF Simulant CPC Studies for SB8," ***SRNL-STI-2013-00106, Rev. 0***, Savannah River National Laboratory, Aiken, SC, 2013.

19. Choi, A. S., "DWPF Melter Off-Gas Flammability Assessment (Sludge Batch 6 and 7A)," ***X-CLC-S-00164***, ***Rev. 5***, Savannah River National Laboratory, Aiken, SC, 2011.

20. Haynes, W. M. (ed.), CRC Handbook of Chemistry and Physics, 94th Ed., p. 3-284, CRC Press LLC, Boca Raton, FL (2013-2014).

21. Hydroxyacetic Acid, International Chemical Safety Cards (ICSC), ICSC 1537, *http://www.ilo.org/dyn/icsc/showcard.display?p_card_id=1537*, 2004.

22. Jantzen, C. M., and Johnson, F. C., "Impacts of Antifoam Additions and Argon Bubbling on Defense Waste Processing Facility (DWPF) REDuction/OXidation (REDOX)," ***SRNL-STI-2011-00652, Rev. 0***, Savannah River National Laboratory, Aiken, SC, 2012.

23. Choi, A. S., “Validation of DWPF Melter Off-Gas Combustion Model (U),” ***WSRC-TR-2000-00100***, Westinghouse Savannah River Company, Aiken, SC, 2000.

24. Choi, A. S., “Validation of DWPF MOG Dynamics Model - Phase I (U),” ***WSRC-TR-96-0307***, Westinghouse Savannah River Company, Aiken, SC, 1997.

25. Choi, A. S., “Melter Off-Gas Flammability Assessment for DWPF Alternate Reductant Flowsheet Options,” ***SRNL-STI-2011-00321***, ***Rev. 0***, Savannah River National Laboratory, Aiken, SC, 2011.

26. Smith, H. D., Jones, E. O., Schmidt, A. J., Zacher, A. H., Brown, M. D., Elmore, M. R., and Gano, S. R., “Denitration of High Nitrate Salts Using Reductants,” ***PNNL-12144***, Pacific Northwest National Laboratory, Richland, WA, 1999.

27. Malecki, A., and Maelcka, B., “Formation of N_2O during Thermal Decomposition of d-Metal Hydrates Nitrates,” ***Thermochimica Acta***, **446 (1-2)**, pp. 113-116 (2006).

28. Freeman, E. S., “The Kinetics of the Thermal Decomposition of Sodium Nitrate and of the Reaction between Sodium Nitrite and Oxygen,” ***Journal of Physical Chemistry***, **60 (11)**, pp. 1487-1493 (1956).

29. Choi, A. S., “Inputs and Assumptions of the DWPF Melter Off-Gas Flammability Model,” ***SRNL-L3100-2015-00217***, ***Rev. 1***, Savannah River National Laboratory, Aiken, SC, 2016.

30. Plante, E. R., Bonnell, D. W., and Hastie, J. W., "Experimental and Theoretical Determination of Oxide Glass Vapor Pressures and Activities," Advances in the Fusion of Glass, Am. Cer. Soc., pp 26.1-26.18 (1988).

31. "Flow of Fluids through Valves, Fittings, and Pipe," ***Technical Paper No. 410***, Crane Co., King of Prussia, PA (1988).

32. Schutte & Koerting, Bulletin 7-S, Performance Curve for Fig. 7009 3-Inch Scrubber (2008).

33. Octave Levenspiel, *Chemical Reaction Engineering,* 3rd Ed., Wiley (1998).

34. Zeigler, K. E., and Bibler, N. E., "Characterization of DWPF Melter Off-Gas Quencher and Steam Atomized Scrubber Deposit Samples," ***WSRC-STI-2007-00262***, ***Rev. 0***, Savannah River National Laboratory, Aiken, SC, 2007.

35. Choi, A. S. and Edwards, T. B., "Measured H_2/TOC and CO/TOC Ratios During 2016 Slurry-Fed Melt Rate Furnace Run with Alternate Reductant Feeds," ***SRNL-L3100-2016-00215***, ***Rev. 1***, Savannah River National Laboratory, Aiken, SC, 2017.

36. Woodham, W. H. and Zamecnik, J. R., "Evaluation of Simple Chemical Interactions in the Defense Waste Processing Facility (DWPF) Chemical Process Cell (CPC) Under the Glycolic Acid Flowsheet," ***SRNL-STI-2017-00318, Rev. 0***, Savannah River National Laboratory, Aiken, SC, 2018.

Appendix A.

Steady State Operating Data during CEF Phase 2 Run

Table A-1. Steady State Data for the Bubbled Run with 125% Acid Stoichiometry Feed with 1X Antifoam (125%_B_1X).

	VS Temp	Feed Rate	FC Air	Cam Air	VS Air	FC Exit T	CEF P	FC Exit P	Glass Temp	H2 (MS)	CO (FTIR)	CO2 (MS)	NO (MS)	NO2 (MS)	N2O (FTIR)
	(°C)	(g/min)	(scfm)	(scfm)	(scfm)	(°C)	("wc)	("wc)	(°C)	(ppm)	(ppm)	(vol%)	(ppm)	(ppm)	(ppm)
average	705	221.38	15.64	8.50	0.65	366	-5.22	-5.97	1,033	43	224	0.9187	2,183	1,430	391
std dev	8		0.08		0.00	6	0.21	0.17	7	13	66	0.1582	225	391	84
max	722		15.83		0.66	385	-4.44	-5.36	1,045	88	494	1.4827	2,425	2,804	670
min	683		15.44		0.62	357	-5.58	-6.26	1,021	25	151	0.6992	1,327	638	271
average	625	161.29	15.92	8.41	0.68	299	-5.35	-5.99	1,032	70	180	0.6758	1,898	981	266
std dev	12		0.07		0.01	8	0.18	0.15	7	16	54	0.0695	155	137	48
max	644		16.11		0.69	319	-4.75	-5.51	1,045	110	418	0.9901	2,346	1,627	429
min	605		15.76		0.66	286	-5.67	-6.26	1,018	43	105	0.5618	1,628	798	181
average	481	113.53	15.88	8.27	15.12	256	-4.90	-6.20	1,025	42	32	0.3115	917	388	106
std dev	7		0.08		0.05	4	0.29	0.29	4	11	10	0.0288	84	32	17
max	496		16.14		15.22	266	-4.01	-5.39	1,036	88	91	0.4413	1,296	523	183
min	471		15.65		15.00	251	-5.42	-6.70	1,016	23	18	0.2531	749	318	80
average	415	110.95	16.08	8.20	22.28	234	-4.74	-6.42	1,029	28	23	0.2451	793	364	90
std dev	5		0.06		0.04	2	0.15	0.14	5	10	7	0.0306	120	48	17
max	425		16.22		22.38	238	-4.27	-5.94	1,039	75	53	0.3784	1,336	577	169
min	403		15.92		22.19	226	-5.09	-6.73	1,021	12	13	0.1974	600	289	61
average	360	92.88	8.54	8.21	40.14	244	-3.48	-5.91	1,011	18	22	0.1832	498	228	68
std dev	9		0.04		0.06	5	0.29	0.26	4	6	8	0.0295	107	35	19
max	377		8.63		40.32	250	-2.63	-5.18	1,021	32	42	0.2605	806	327	108
min	344		8.43		39.98	235	-4.15	-6.55	1,005	4	6	0.1148	302	162	36
average	270	72.15	6.20	8.08	50.68	203	-1.16	-3.85	1,035	19	19	0.1617	441	184	59
std dev	8		0.03		0.08	4	0.22	0.20	3	5	8	0.0237	87	26	16
max	282		6.27		50.92	211	-0.49	-3.27	1,042	38	43	0.2162	676	246	100
min	251		6.10		50.50	194	-1.67	-4.29	1,027	8	3	0.1053	246	124	27

Table A-2. Steady State Data for the Non-Bubbled Run with 125% Acid Stoichiometry Feed with 1X Antifoam (125%_NB_1X).

	VS Temp	**Feed Rate**	**FC Air**	**Cam Air**	**VS Air**	**FC Exit T**	**CEF P**	**FC Exit P**	**Glass Temp**	**H2 (MS)**	**CO (FTIR)**	**CO2 (MS)**	**NO (MS)**	**NO2 (MS)**	**N2O (FTIR)**
	(°C)	(g/min)	(scfm)	(scfm)	(scfm)	(°C)	("wc)	("wc)	(°C)	(ppm)	(ppm)	(vol%)	(ppm)	(ppm)	(ppm)
average	302	35.08	15.91	8.14	29.62	183	-4.96	-6.81	1,084	12	6	0.1186	332	213	32
std dev	1	0.00	0.07		0.93	0	0.39	0.33	2	1	2	0.0078	46	18	5
max	303	0.00	16.08		30.33	184	-3.59	-5.56	1,088	17	13	0.1322	434	252	44
min	301	0.00	15.77		28.05	183	-5.52	-7.25	1,081	9	3	0.0986	252	181	22
average	351	44.27	15.93	8.19	20.89	200	-5.04	-6.43	1,083	16	11	0.1566	374	279	56
std dev	5	0.00	0.08		0.35	2	0.19	0.17	2	8	5	0.0335	105	55	17
max	363	0.00	16.21		20.99	205	-4.70	-6.12	1,087	51	31	0.2217	640	419	99
min	343	0.00	15.69		14.96	197	-7.71	-8.84	1,078	3	1	0.0911	174	174	24
average	393	51.07	15.73	8.13	14.98	212	-5.46	-6.56	1,085	23	14	0.1885	517	275	75
std dev	8	0.00	0.08		0.04	4	0.10	0.09	3	10	7	0.0434	135	54	25
max	409	0.00	15.97		15.06	219	-4.97	-6.15	1,090	82	56	0.3893	1,149	502	195
min	377	0.00	15.50		14.87	205	-5.70	-6.79	1,079	6	3	0.0856	120	117	21
average	486	87.60	15.89	8.44	0.28	217	-5.51	-6.16	1,059	83	55	0.4312	1,275	704	189
std dev	5	0.00	0.05		0.01	4	0.11	0.10	7	30	17	0.0918	330	195	59
max	500	0.00	16.04		0.31	228	-5.09	-5.81	1,073	138	122	0.6996	2,210	1,288	389
min	478	0.00	15.77		0.25	209	-5.76	-6.37	1,044	29	19	0.2477	652	382	83
average	604	105.85	16.04	8.56	0.25	279	-5.29	-6.00	1,060	46	119	0.4400	1,377	824	222
std dev	3	0.00	0.05		0.01	3	0.09	0.08	4	10	32	0.0727	242	168	50
max	610	0.00	16.18		0.28	286	-5.01	-5.78	1,070	86	221	0.7327	2,250	1,462	390
min	598	0.00	15.88		0.23	273	-5.47	-6.15	1,053	23	67	0.2552	927	430	138
average	709	99.60	15.73	8.30	0.45	325	-5.47	-6.02	1,083	13	119	0.4308	1,360	607	219
std dev	3	0.00	0.07		0.01	2	0.09	0.08	6	5	28	0.0629	201	106	42
max	716	0.00	15.89		0.47	333	-5.21	-5.74	1,096	29	217	0.6064	2,003	956	356
min	703	0.00	15.58		0.41	322	-5.66	-6.18	1,075	7	72	0.3191	1,004	443	149

Table A-3. Steady State Data for the Non-Bubbled Run with 100% Acid Stoichiometry Feed with 1X Antifoam (100%_NB_1X).

	VS Temp	Feed Rate	FC Air	Cam Air	VS Air	FC Exit T	CEF P	FC Exit P	Glass Temp	H2 (MS)	CO (FTIR)	CO2 (MS)	NO (MS)	NO2 (MS)	N2O (FTIR)
	(°C)	(g/min)	(scfm)	(scfm)	(scfm)	(°C)	("wc)	("wc)	(°C)	(ppm)	(ppm)	(vol%)	(ppm)	(ppm)	(ppm)
average	697	125.22	16.14	8.07	0.32	323	-5.27	-5.77	1,086	17	117	0.4755	1,445	671	152
std dev	5	0.00	0.11		0.01	3	0.10	0.08	4	4	26	0.0551	163	93	28
max	708	0.00	16.44		0.32	328	-5.00	-5.53	1,096	28	242	0.6445	2,001	989	241
min	688	0.00	15.87		0.30	316	-5.52	-5.99	1,080	8	65	0.3293	1,027	382	93
average	600	98.54	16.55	8.09	0.32	268	-5.70	-6.15	1,085	23	85	0.3550	1,137	518	125
std dev	5	0.00	0.09		0.01	2	0.09	0.08	4	6	30	0.0708	186	95	33
max	614	0.00	16.79		0.35	273	-5.27	-5.79	1,092	44	196	0.6306	2,033	1,044	289
min	593	0.00	16.23		0.30	263	-5.93	-6.35	1,074	14	40	0.2395	802	360	78
average	496	84.48	16.80	8.09	0.33	214	-6.00	-6.42	1,068	19	26	0.2967	993	455	96
std dev	5	0.00	0.07		0.01	4	0.11	0.10	5	9	15	0.0749	215	105	37
max	507	0.00	17.00		0.36	226	-5.52	-6.00	1,078	55	95	0.6123	2,067	1,027	261
min	488	0.00	16.58		0.32	208	-6.21	-6.61	1,059	6	9	0.1976	668	319	56
average	410	55.75	16.83	8.05	13.22	209	-5.46	-6.49	1,074	7	8	0.1210	502	244	634
std dev	5	0.00	0.10		0.03	3	0.11	0.10	5	4	4	0.0240	93	32	119
max	422	0.00	17.03		13.30	216	-5.08	-6.17	1,086	21	22	0.2221	953	391	1,241
min	400	0.00	16.54		13.14	203	-5.76	-6.76	1,065	4	2	0.0533	256	176	330
average	344	47.59	16.10	7.98	27.93	201	-4.46	-6.28	1,078	6	4	0.0944	307	196	364
std dev	2	0.00	0.07		0.04	1	0.21	0.18	4	2	2	0.0113	52	20	60
max	349	0.00	16.29		28.05	203	-3.34	-5.37	1,084	13	11	0.1347	502	262	584
min	341	0.00	15.90		27.84	200	-5.13	-6.87	1,070	3	0	0.0791	222	157	266
average	326	42.33	9.67	8.01	34.77	217	-4.02	-5.99	1,079	6	4	0.0946	284	252	348
std dev	3	0.00	0.03		0.07	2	0.34	0.29	1	3	2	0.0146	59	30	72
max	330	0.00	9.76		34.93	219	-3.25	-5.34	1,081	17	19	0.1389	490	346	596
min	320	0.00	9.58		34.58	212	-4.83	-6.76	1,078	2	0	0.0687	180	191	224

Table A-4. Steady State Data for the Bubbled Run with 100% Acid Stoichiometry Feed with 1X Antifoam (100%_B_1X).

	VS Temp	Feed Rate	FC Air	Cam Air	VS Air	FC Exit T	CEF P	FC Exit P	Glass Temp	H2 (MS)	CO (FTIR)	CO2 (MS)	NO (MS)	NO2 (MS)	N2O (FTIR)
	(°C)	(g/min)	(scfm)	(scfm)	(scfm)	(°C)	("wc)	("wc)	(°C)	(ppm)	(ppm)	(vol%)	(ppm)	(ppm)	(ppm)
average	705	170.49	15.25	8.39	0.52	358	-4.81	-5.50	1,050	19	161	0.6592	1,947	1,091	220
std dev	5	0.00	0.05		0.02	5	0.17	0.14	4	8	53	0.1316	242	290	52
max	714	0.00	15.37		0.55	370	-4.08	-4.88	1,057	55	344	1.0679	2,298	1,956	369
min	691	0.00	15.12		0.49	347	-5.17	-5.79	1,043	5	67	0.4343	578	205	135
average	592	146.21	15.32	8.35	0.51	285	-4.66	-5.25	1,042	37	109	0.5123	1,682	866	165
std dev	5	0.00	0.05		0.01	6	0.20	0.16	6	16	60	0.1272	259	228	53
max	602	0.00	15.51		0.52	300	-3.83	-4.65	1,049	113	480	1.0635	2,283	2,031	406
min	576	0.00	15.19		0.49	278	-5.01	-5.57	1,029	20	49	0.3765	1,098	612	103
average	471	122.69	15.32	8.29	6.09	235	-4.42	-5.22	1,041	31	55	0.3991	1,303	673	115
std dev	8	0.00	0.05		0.02	4	0.20	0.18	5	18	32	0.1101	323	178	40
max	485	0.00	15.48		6.14	244	-3.67	-4.55	1,053	108	150	0.7743	2,232	1,311	246
min	456	0.00	15.13		6.03	225	-4.88	-5.62	1,031	8	12	0.2624	857	443	72
average	373	101.80	15.50	7.97	25.94	219	-5.06	-6.96	1,025	18	20	0.2178	689	340	56
std dev	5	0.00	0.08		0.04	2	0.26	0.23	5	6	9	0.0259	104	38	10
max	384	0.00	15.77		26.06	226	-4.03	-6.05	1,035	65	69	0.3338	1,155	511	99
min	363	0.00	15.32		25.82	215	-5.84	-7.73	1,016	8	6	0.1729	471	263	39
average	323	88.29	6.12	7.86	45.90	224	-1.13	-3.61	1,031	13	18	0.1297	545	268	674
std dev	10	0.00	0.04		0.06	7	0.30	0.27	2	8	10	0.0258	152	55	188
max	341	0.00	6.20		46.04	238	1.16	-1.68	1,035	69	86	0.2697	1,319	546	1,625
min	302	0.00	6.02		45.74	207	-1.96	-4.39	1,025	3	4	0.0719	318	185	399

Table A-5. Steady State Data for the Non-Bubbled Run with 100% Acid Stoichiometry Feed with 2X Antifoam (100%_NB_2X).

	VS Temp	Feed Rate	FC Air	Cam Air	VS Air	FC Exit T	CEF P	FC Exit P	Glass Temp	H2 (MS)	CO (FTIR)	CO2 (MS)	NO (MS)	NO2 (MS)	N2O (FTIR)
	(°C)	(g/min)	(scfm)	(scfm)	(scfm)	(°C)	("wc)	("wc)	(°C)	(ppm)	(ppm)	(vol%)	(ppm)	(ppm)	(ppm)
average	722	102.72	16.14	8.60	0.19	334	-2.92	-3.67	1,097	6	154	0.5765	1,522	794	107
std dev	2	0.00	0.05		0.01	3	0.07	0.06	2	9	53	0.1126	246	155	26
max	726	0.00	16.26		0.20	340	-2.78	-3.56	1,102	27	348	0.8947	2,395	1,354	210
min	719	0.00	16.02		0.17	329	-3.09	-3.84	1,093	0	69	0.4235	1,090	547	67
average	604	46.65	15.97	8.61	0.41	292	-5.38	-6.14	1,071	60	213	0.4841	1,300	728	103
std dev	7	0.00	0.05		0.01	4	0.13	0.12	3	12	39	0.0346	115	81	13
max	616	0.00	16.09		0.45	302	-4.86	-5.64	1,074	101	373	0.6223	1,717	1,017	149
min	593	0.00	15.83		0.39	285	-5.63	-6.42	1,062	38	138	0.4104	1,028	566	75
average	519	57.41	15.99	8.56	0.42	222	-5.12	-5.77	1,066	10	89	0.2563	787	451	59
std dev	4	0.00	0.05		0.01	2	0.08	0.07	6	4	29	0.0498	163	90	16
max	524	0.00	16.12		0.45	226	-4.89	-5.56	1,080	29	241	0.5195	1,614	935	166
min	514	0.00	15.85		0.39	217	-5.34	-5.97	1,056	5	51	0.1809	527	320	35
average	397	49.35	15.85	8.48	19.00	211	-4.63	-6.29	1,052	9	51	0.1545	392	223	28
std dev	10	0.00	0.05		0.04	3	0.08	0.07	5	3	14	0.0294	96	42	10
max	412	0.00	16.00		19.11	217	-4.42	-6.10	1,058	22	109	0.2492	723	356	66
min	383	0.00	15.70		18.91	207	-4.90	-6.51	1,039	3	24	0.1032	209	142	14
average	323	39.14	10.01	8.47	27.97	211	-4.04	-5.97	1,067	9	22	0.1178	287	163	20
std dev	6	0.00	0.04		0.05	2	0.10	0.09	3	2	7	0.0148	60	24	5
max	330	0.00	10.09		28.16	214	-3.70	-5.66	1,072	17	49	0.1895	575	272	41
min	313	0.00	9.88		27.85	208	-4.31	-6.17	1,061	5	8	0.0901	185	121	12
average	293	36.81	5.69	8.46	34.39	227	-2.80	-4.88	1,066	10	27	0.1104	243	146	21
std dev	5	0.00	0.04		0.09	1	0.29	0.25	2	2	7	0.0120	45	19	4
max	300	0.00	5.77		34.60	229	-2.22	-4.40	1,069	17	61	0.1656	461	229	41
min	283	0.00	5.61		34.25	223	-3.36	-5.40	1,064	6	16	0.0886	177	118	14

Appendix B.

Design Check Lists

Distribution:

D. E. Dooley, 773-A
C. C. Herman, 773-A
F. M. Pennebaker, 773-A
G. A. Morgan, 999-W
J. R. Zamecnik, 999-W
Records Administration (EDWS)

R. E. Edwards, 766-H
E. W. Holtzscheiter, 766-H
T. L. Fellinger, 766-H
D. W. McImoyle, 766-H

E. J. Freed, 704-S
J. F. Iaukea, 704-S
M. A. Rios-Armstrong, 704-S
J. Stevens, 704-S
M. C. Clark, 704-26S
K. M. Brotherton, 704-27S
V. M. Kmiec, 704-27S
J. D. Ledbetter, 704-27S
M. M. Potvin, 704-27S
A. V. Staub, 704-30S
Q. L. Nguyen, 704-30S
Z. L. Wesley, 704-30S

T. E. Colleran, 707-4E
G. Chen, 707-4E
R. A. Smith, 707-7E
C. B. Sudduth, 707-7E